Ollscoil na hÉireann, Corcaigh

National University of Ireland, Cork

University College Cork, Ireland
Coláiste na hOllscoile Corcaigh

An experimental investigation into the most prominent sources of uncertainty in wave tank testing of floating offshore wind turbines

Thesis presented by

Eoin Lyden, BECSE (Honours)

for the degree of

Master of Civil Engineering

University College Cork
Department of Civil, Structural and Environmental Engineering

Head of School/Department: Dr Jorge Oliveira
Supervisor(s):
Dr Jimmy Murphy
Dr Frances Judge

30/08/2022

Table of Contents

Declaration 5

List of Figures 6

List of Tables 8

Abstract 9

Acknowledgements 11

List of Abbreviations 12

List of Key Symbols 13

1 Introduction *15*

1.1 General Introduction 15

1.2 Problem definition 17

1.3 Research Objectives 18

1.4 Outline of Thesis 19

2 Literature Review *20*

2.1 Offshore wind 20

2.1.1 Background and History 20

2.1.2 Reasons for Offshore Wind Renewable Energy. 23

2.2 Floating Platform Behaviour 27

2.2.1 Platform motions 27

2.2.2 Wave forces acting on FOWTs 29

2.2.3 Magnitude and frequency of platform motions 34

2.3 Main Types of Offshore wind Platforms 36

2.3.1 Platform design issues 40

2.4 Wave Tank Testing 42

2.4.1 Why wave tank testing 42

2.4.2 Scaling for wave tank testing 44

2.4.3 Mooring requirements for wave tank testing. 50

2.5 Uncertainty Analysis 52

2.5.1 Introduction 52

2.5.2 Uncertainty Classification 53

2.5.3 Sources of experimental uncertainty in wave tank testing 57

2.5.4 Combined Uncertainty (u_c) 60

2.5.5 Uncertainty Analysis of Irregular waves 62

2.6 Summary 65

3 Experimental Test Campaign *66*

3.1 Introduction 66

3.2 Model Descriptions 66

3.2.1 Model A 66

3.2.2 Model B 71

3.3 Model Design and Fabrication 72

3.4 In-air tests 73

3.4.1 Balance tests and hang tests to determine the location of the CoG 73
3.4.2 Moment of Inertia Bifilar and Trifilar tests 75

3.5 Test Facility 78

3.6 Instrumentation used 79

3.7 Wave Tank Testing Setup 81
3.7.1 Model A 81
3.7.2 Model B 82

3.8 Test Plan 83

3.9 Wave Calibration 85

3.10 Test Setups 88
3.10.1 Model A Inertia Variation A – *V2* and *V4* 88
3.10.2 Model A Inertia Variation B – *V3* and *V6* 89
3.10.3 Model A Wind emulation system variation – *V4*, *V5*, and *V6* 90
3.10.4 Model A Mooring Variation A – *V7* 93
3.10.5 Model A Mooring Variation B –*V8* 94
3.10.6 Model B Inertia Variation A –*V10* 94
3.10.7 Model B Inertia Variation – *V11* 94
3.10.8 Model B wind emulation system variation –*V12* 95
3.10.9 Summary 96

3.11 In-water decay tests 97

4 Analysis and Discussion 99

4.1 Repeatability 99
4.1.1 Model A 99
4.1.2 Model B 114

4.2 Effect of changes in inertia on platform responses 121
4.2.1 Model A 121
4.2.2 Model B 128

4.3 Effect of wind emulation system on platform motions 135
4.3.1 Model A 135
4.3.2 Model B 143

4.4 Influence of mooring system stiffness on platform responses 149

5 Conclusions 156

5.1 Introduction 156

5.2 Detailed conclusions 156
5.2.1 Conclusions from variations in model physical properties 156
5.2.2 Conclusions from variations in wind emulation system. 158
5.2.3 Conclusions from variations in mooring stiffness 160

5.3 Overall Conclusions 161

5.1 Recommendations for further research 163

6 References 166

7 Appendices 175

7.1 Test List Model A 175

7.2 Test List Model B 177

7.3 Summary of Results. ____ 178

Declaration

"This is to certify that the work I am submitting is my own and has not been submitted for another degree, either at University College Cork or elsewhere. All external references and sources are clearly acknowledged and identified within the contents. I have read and understood the regulations of University College Cork concerning plagiarism and intellectual property."

Signed: 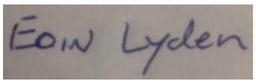

Date: 30/08/2022

Eoin Lyden

List of Figures

Figure 1 – Different types of floating offshore wind platform (DNV GL, 2018) 16
Figure 2 - The widely used American Pumping Jack 21
Figure 3(a) and (b) - The Darrieus Turbine and McDowell's H-rotor.....................................21
Figure 4 - 200kW Gedser Wind Turbine 22
Figure 5 - Evolution of wind turbine power output and size over time(Pisano, 2019). 22
Figure 6 - Gross installation of Wind Energy Converters, Onshore vs Offshore (WindEurope, 2019) 24
Figure 7 - Average windspeed(m/s) at a height of 100m Ireland(Vortexfdc, 2021)................25
Figure 8- Variation in water depth along Irish coasts (Gosch et al., 2019) 26
Figure 9 – The Six-Degrees-of-Freedom(6DoF)(Dvorak, 2021)..28
Figure 10 – Ship as a mass-spring system...33
Figure 11 - Types of offshore wind turbine (Bailey et al., 2014) 37
Figure 12 – Hywind wind farm in Scotland with a spar-buoy floating platform (Equinor, 2020) 38
Figure 13 – Blue H Technologies TLP concept tested in 2008 (Blue H Technologies, 2017) ...39
Figure 14 – Windfloat Atlantic development off the coast of Portugal (PrinciplePower, 2019) 40
Figure 15 – Impeller Blade used for the first iteration of SiL (Azcona et al., 2019).................47
Figure 16– Diagram of the Software-in-the-loop method (Azcona et al., 2019)....................48
Figure 17 – SMART mooring line arrangement (Chakrabarti, 2005) 50
Figure 18- Accuracy vs Precision (Edvotek, 2021) 54
Figure 19 - Student-t distribution table (Tdistributiontable, 2020)..57
Figure 20 - A sample of different probability distributions (Menon, 2020) 62
Figure 21 – Plan and elevation view of Model A with full-scale dimensions (MaRINET2, 2019) 68
Figure 22 – Model in the tank during testing. 68
Figure 23- Ifremer Thruster used on Model A 69
Figure 24 – Mooring system setup. 70
Figure 25 – Mooring line fairleads and attachments to tank wall for model A.......................71
Figure 26 Measuring the CoG using a long angle section, the 90° silver bar shown in both images 74
Figure 27- Labelling for bifilar method explained...76
Figure 28 – Bifilar test for x, y, and z axes from left to right for model A. 76
Figure 29-Lir DOB, view from behind the paddles..79
Figure 30 - Qualisys motion tracking markers on Model A and view of the type of markers used 80
Figure 31 – Futek 10lb load cell (left) and EFE 200N load cell (right) 81
Figure 32 – PSD of the PN time series for each repeat in the low-frequency range (left) and the wave-frequency range(right). 88
Figure 33 – Pulley system employed for V4, V5, and V6. The attachment point to the thruster (left) and the pulley used(right). 91
Figure 34- Weight attached to simulate thrust 91
Figure 35 - Close-up view of the pulley used during testing 92
Figure 36 – Thruster used for Variation 12 95
Figure 37 - UCC Thruster during the calibration procedure. 96

Figure 38 – Variation in PSD for surge, heave, and pitch for repeats of Model A................100
Figure 39 – Variation in PSD for sway (top), roll (middle), and yaw (bottom) for repeats of Model A...102
Figure 40 – Variation in PSD of mooring line responses for repeats of Model A. 104
Figure 41 – Regions with bounds of f_1 and f_2 for the calculation of T_r and $T_{r,\ mag}$. 107
Figure 42 – Variation in M_{WF} in surge, heave, and pitch for repeats of Model A.................109
Figure 43 – Variation in M_{WF} in sway, roll, yaw, and mooring line responses for repeats of Model A...111
Figure 44 – Variation in T_r in surge, heave, and pitch for repeats of Model A. 112
Figure 45 – Variations in $T_{r,\ mag}$ in surge heave, and pitch for repeats of Model A. 113
Figure 46 – Variations in M_{WF} in surge, heave, and pitch for repeats of Model B. 115
Figure 47 – Variation in M_{WF} in sway, roll, yaw, and mooring line responses for repeats of Model B. 117
Figure 48 - Variation in T_r in surge, heave, and pitch for repeats of Model B. 119
Figure 49 – Variation in $T_{r,\ mag}$ 120
Figure 50 – Change in surge T_r with changes in inertia for model A 122
Figure 51 - Change in heave T_r with changes in inertia for model A. 123
Figure 52 - Change in pitch T_r with changes in inertia for model A. 124
Figure 53 – Variations in $T_{r,\ mag}$ for variation in inertia surge, heave, and pitch for model A. 126
Figure 54 – Change in surge M_{WF} of model A with changes in inertia. 127
Figure 55 - Change in surge T_r with changes in inertia for model B 129
Figure 56 - Change in heave T_r with changes in inertia for model B. 130
Figure 57 – Change in pitch T_r with changes in inertia for model B. 131
Figure 58 – Model A pitch decay test (left) vs model B pitch decay test (right). 131
Figure 59 – Change in $T_{r,\ mag}$ in surge, heave, and pitch with changes in inertia for model B. 133
Figure 60 -Thruster system vs Pulley system effect on T_r in surge, heave, and pitch. 136
Figure 61 -Thruster system vs Pulley system effect on $T_{r,\ mag}$ in surge, heave, and pitch. 137
Figure 62 – Thruster system vs Pulley system effect on M_{WF} in surge, heave, and pitch. 139
Figure 63 – Thruster vs Pulley system effect on M_{WF} for sway, roll, yaw, and mooring responses. 141
Figure 64 – Surge decay tests for thruster (above) and pulley (below) model A. 142
Figure 65 – Pitch decay tests with the thruster (left) and the pulley (right) for model A. 143
Figure 66 – Variation in thrust for test 001 with SIL vs constant thrust force for all tests in V12. 144
Figure 67 - Effect of change of wind emulation system on $T_{r,}$ for model B. 145
Figure 68 – PSD of model B for V9 and V12. 146
Figure 69 – SiL thrust response to platform motions 147
Figure 70 – Effect of change of wind emulation system on $T_{r,\ mag}$ for model B. 148
Figure 71 – Variation in T_r with changes in mooring stiffness for surge, heave, and pitch for model A. 151
Figure 72 – Variation in $T_{r,\ mag}$ for surge, heave, and pitch with variations in mooring stiffness. 153
Figure 73 – Effect of variations in mooring stiffness on surge M_{WF} for model A. 154

List of Tables

Table 1 – Mode numbers for each motion 30
Table 2– Froude scaling factors (Samuel, 2019) 45
Table 3 – Table for Mass and Draft of Model A at Model scale and full-scale. 67
Table 4- Initial Location of CoG of Model A 67
Table 5 - Initial Inertia Properties of Model...67
Table 6 – Stiffness of Mooring lines for initial mooring setup. 71
Table 7 – Difference between desired and actual properties for model A. 73
Table 8 – Probe locations calibration model A. 82
Table 9 – Mooring line fastening points for model A. 82
Table 10 – Probe locations calibration model A. 83
Table 11 – PN wave parameters 84
Table 12 – Summary of tests carried out with variations indicated 84
Table 13 – Comparison between calibration waves at model A full-scale. 86
Table 14 – Deviations from the average value at model A full-scale. 87
Table 15- Model A Inertia Variation A; location of CoG at full-scale. 89
Table 16 – Model A Inertia Variation A; Inertia Values at full-scale. 89
Table 17 – Model A Inertia Variation B; location of CoG at full-scale. 90
Table 18 - Model A Inertia Variation B; Inertia Values at full-scale. 90
Table 19 – Masses added to the pulley to emulate thrust. 93
Table 20 - Mooring Variation A; Spring Stiffness' 93
Table 21 – Mooring Variation B; Spring stiffness' 94
Table 22 – Summary of variations made. 97
Table 23 – Frequency bounds used for calculation of T_r. 106
Table 24 – Model Property changes for V1, V2, and V3 relative to the base case, V1 121
Table 25 – Values for metrics for V1, V2, and V3. 128
Table 26 - % change in V1, V2, and V3 relative to the base case, V1. 128
Table 27 - Model Property changes for V9, V10, and V11 relative to the base case, variation 9. 129
Table 28 - Values for metrics for V9, V10, and V11. 134
Table 29 - % change in metrics for V9, V10 and V11 relative to the base case, V9. 135
Table 30 – Summary of values for metrics for V1 and V4 143
Table 31 - % change in metrics for V1 and V4 relative to the base case, V1. 143
Table 32 - Summary of values for metrics for V9 and V12 149
Table 33 - % change in metrics for V1 and V4 relative to the base case, V1. 149
Table 34 – Change in mooring stiffness for V1, V7, and V11 relative to the base case, V1. .150
Table 35 – Summary of values for metrics for V1, V7, and V8. 155
Table 36 - % change in the metrics for V1, V7, and V8 relative to the base case, V1. 155

Abstract

There is an urgent need to replace carbon-based energy sources with renewable energy sources, and floating offshore wind is seen as a critical component in the drive towards energy diversification. Floating offshore wind facilitates accessing a far vaster wind resource that exists in deeper waters, further offshore.

Floating offshore wind platforms must undergo wave tank testing in the early stages of development to assess model responses to different wave and wind conditions. Wave tank testing, while highly beneficial, is liable to errors arising throughout the testing campaign. Errors can arise during wave tank setup, testing, and analysis of results. Some of the primary sources of error include errors in the model location within the tank, errors in model parameters like mass, inertia and CoG, and errors due to incorrect replication of mooring forces and aerodynamic forces from the turbine.

Scaling wind turbine blade properties can be challenging; this is because aerodynamic forces are scaled using Reynolds scaling, but all hydrodynamic forces are scaled using Froude scaling. For this reason, wind emulation systems are used to replicate the aerodynamic forces from the turbine only.

Testing was completed using two very different floating offshore wind concepts. A sensitivity analysis was completed by conducting variations to the wind emulation system used, the model inertia and centre of gravity, and the mooring stiffness of the model. The magnitudes of the variations to the inertia, centre of gravity and mooring stiffness were based on the uncertainty in the values of each of the parameters. Three wind emulation systems of varying complexity were used for this comparison, a simple weighted pulley system, a constant thruster and the software in the loop system developed by CENER. The comparison was conducted to assess the influence of wind emulation systems on the uncertainty of platform response

It was found that the effects of each variation conducted were magnified at resonance, and the magnitude of platform response was affected to a greater extent than the period of

resonance response. Of all the variations to the model properties conducted, the inertia about the y-axis and location of the centre of gravity along the x-axis affected pitch response to the greatest extent. A 7% change in the inertia about the y-axis coupled with an 8.57% resulted in a 10% change in the period of resonance response for pitch, T_r, and 52% decrease in the magnitude of resonance respsonse for pitch, $T_{r,\ mag}$. Changes in the wind emulation system affected the pitch response most significantly, while the period of resonance response T_r, was mostly unaffected , the magnitude of resonance response $T_{r,\ mag}$, was reduced by nearly 90% when a pulley system was used in lieu of a conventional thruster for a semi-submersible model. Changes in mooring stiffness did not influence the period of resonance response but did affect the magnitude of resonance response, particularly in surge. For a linear horizontal mooring system applied to a semi-submersible model, a 1% decrease in the spring stiffness resulted in a 9% decrease in the magnitude of resonance response for surge, $T_{r,\ mag}$.

Acknowledgements

I am deeply grateful to many people who helped me with my research throughout the year. Firstly, I would like to express my sincere thanks to my supervisors, Dr Jimmy Murphy and Dr Frances Judge. Without their guidance and constructive feedback throughout the year, it would not have been possible to complete this study. I would also like to thank Sebastien Gueydon for his help throughout the year on all aspects of this research project. His experience and immense knowledge helped develop such a comprehensive testing campaign and guided me through the analysis procedure.

I would like to thank Dr Michael O'Shea, the MaRINET2 project coordinator, for allowing me to be part of such an incredible initiative and allowing me to use their floating offshore wind model for my research purposes. To all the staff at MaREI, I would like to thank all of you for allowing me to use the facilities and helping me proceed with my research and studies throughout such a challenging year. In particular, I would like to thank Thomas Walsh, Ian Power, Christian van den Bosch and Derek O' Gorman for helping me complete the two testing campaigns. Between all of you, you helped me with everything from model construction to setting up the tank for each round of testing, while imparting your wisdom to me along the way.

Finally, I would like to thank my family and friends for their support and encouragement throughout the year.

List of Abbreviations

- ASME – American Society of Mechanical Engineers
- BMOWT – Bottom Mounted Offshore Wind Turbines
- CoG – Centre of Gravity
- DOB – Deep Ocean Basin
- EFE – Essor Francaise Electronique
- FAST – Fatigue, Aerodynamics, Structures, and Turbulence
- FORE – Floating Offshore Renewable Energy
- FOW – Floating Offshore Wind
- FOWT – Floating Offshore Wind Turbine
- HAWT – Horizontal Axis Wind Turbine
- IPCC – Intergovernmental Panel on Climate Change
- ISO – International Organisation for Standardisation
- ITTC – Internation Towing Tank Conference
- JONSWAP – Joint North Sea Wave Project
- LCOE – Levelised Cost of Energy
- LiR – LiR National Ocean Testing Facility
- MaREI – Marine and Renewable Energy Ireland
- MCM – Monte Carlo Method
- OWC – Oscillating Water Column
- PDF – Probability density function
- PN – Pink Noise
- PSD – Power Spectral Density
- RAO – Response Amplitude Operator
- SiL – Software in the Loop
- TLP – Tension Leg Platform
- TSM – Taylor Series Method
- VAWT – Vertical Axis Wind Turbine
- WEC – Wave Energy Converter
- 6DoF – Six Degrees of Freedom

List of Key Symbols

Symbol	Meaning	Unit
P_{avail}	Power from a turbine	W
ρ	density	kg/m^3
v	velocity	m/s
C_p	Power coefficient for a turbine	-
$\boldsymbol{F}_{wave}$	Force from a wave	kN
$\boldsymbol{F_e}$	Excitation Force	kN
$\boldsymbol{F_r}$	Radiation Force	kN
$\boldsymbol{F_h}$	Hydrostatic Force	kN
ω	Wave frequency	rad/s
g	Acceleration due to gravity	m/s^2
A_{wl}	Area of the waterline of platform	m^2
C_{11}	Hydrostatic Stiffness in Surge	N/m
C_{33}	Hydrostatic Stiffness in Heave	N/m
C_{44}	Hydrostatic Stiffness restoring moment Roll	Nm
C_{55}	Hydrostatic Stiffness restoring moment Pitch	Nm
GM_L	Longitudinal Metacentric Height	m
GM_T	Transverse Metacentric Height	m
M	Mass of a Body	kg
∇	Displaced Volume	m^3
RG_{kk}	Radius of gyration for the k^{th} degree of freedom (Equation 32 and Equation 33)	m
A_{kk}	Added mass for the k^{th} degree of freedom (See Table 1)	kg/m^2
I_{kk}	Inertia for the k^{th} degree of freedom (See Table 1)	kg/m^2
Fr	Froude Number	-
Re	Reynolds Number	-
U_m	Mean velocity	m/s
D	Hydraulic Mean Depth	m
μ	Viscosity of water	Pa.s

u_A	Type A uncertainty	
n	Number of repeat tests	-
s	Standard deviation	-
q_k	The value of the k^{th} observation	-
u_B	Type B uncertainty	-
u_c	Combined uncertainty	-
U	Expanded uncertainty	-
k	Coverage Factor (Equation 41)	-
M_{WF}	Integral under PSD of response spectrum in wave-frequency range	SI/m
f	Frequency	Hz
f_1	Lower frequency bound for wave-frequency range	Hz
f_2	Upper frequency bound for wave-frequency range	Hz
S_{signal}	PSD of the response spectrum	-
m_0	0^{th} spectral moments	m^2
S_η	Wave PSD	m^2/Hz
T_r	Period of resonance response	s
f_e	Eigenfrequency	Hz
δf	Frequency bound around f_e for calculation of T_r	Hz
T	Period of oscillation	s
l	Length of filars	m
d	Distance between filars	m
T_z	Zero-up crossing period	s
H_s	Significant wave height	m
m_2	2^{nd} spectral moment	$m^2.Hz^2$
T_{-10}	Energy period	s
m_{-1}	1^{st} negative moment	m^2/Hz
S_s	Significant wave steepness	-
KG_Z	Distance between keel of platform and CoG_Z	m
$T_{r,\ mag}$	Magnitude of resonance response	SI^2/Hz
k	Mooring line stiffness	N/m

1 Introduction

1.1 General Introduction

Since the pre-industrial era, excessive fossil fuel consumption has had consequences on global temperatures (IPCC, 2018). As a result, there has been an increased focus on developing renewable energy sources to stunt the rate of global temperature increases. In 2021 wind energy provided 38% of Ireland electricity demand, the highest of any country in Europe (WindEurope, 2021). Most of this wind resource is from onshore wind. Of the 4309MW of installed wind capacity in Ireland, only 25MW are from offshore wind (Wind Energy Ireland, 2021). This 25MW capacity comes from the Arklow Bank wind farm, where the turbines are placed on fixed foundations. Water depths on Irish coastlines, particularly southern and western Atlantic coasts, increase rapidly with distance from the coastline, meaning floating offshore wind is more suitable than fixed (Chester et al., 2019). It is expected that Ireland's offshore wind capacity will increase significantly when floating offshore wind technologies become more widespread. Much of Irelands planned increases in offshore wind capacity are reliant on advances in the floating offshore wind sector. It is believed that in Ireland, an offshore wind capacity of over 30GW could be achieved by 2050, mostly from floating offshore wind(McAuliffe et al., 2020).

The basic principles of the floating platform are to reduce wave-induced motions to provide a stable foundation for the turbines that are placed upon them. There are three main concepts, the spar-buoy, the semi-submersible, and the tension leg platform. Spar-buoy platforms are deep, drawing up to 70m, and narrow platforms that are heavily ballasted at the bottom of the platform to provide stability. Semi-submersible platforms draw approximately 20 – 30m and use a large water plane area and ample buoyancy to provide stability (Hannon et al., 2019). Tension leg platforms consist of a structure with ample buoyancy restrained through a tension leg mooring system. When inclined, the tension in the legs provides stability (ETI, 2015).

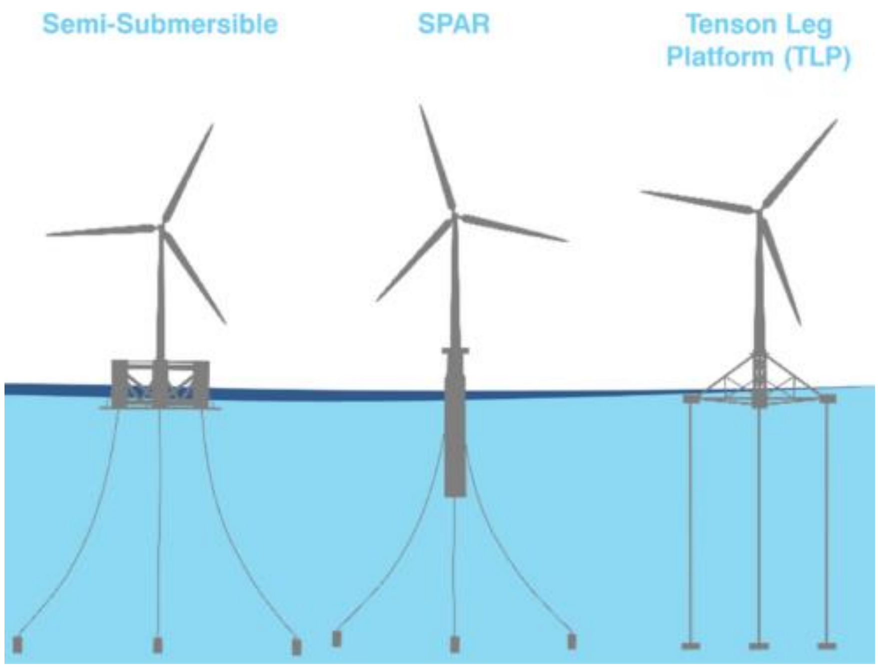

Figure 1 – Different types of floating offshore wind platform (DNV GL, 2018)

Several obstacles must be overcome before floating offshore wind can even be deployed at a large scale. Very few ports have the necessary infrastructure to move and launch the massive floating platforms, access to the platforms for maintenance is challenging, and the maintenance costs are all challenges that will have to be overcome. Despite these challenges, there have been some installations of floating offshore wind. Two Scottish projects, the Hywind project (Equinor, 2021b) and the Kincardine Wind Farm (PrinciplePower, 2021), have been installed with great success. The former has been the UK's best-performing wind farm since its installation, and the latter is the worlds largest floating wind installation, with a nominal capacity of 50MW. The hywind project uses a spar design, and Kincardine wind farm uses a semi-submersible design, and stability is provided from buoyancy.

The spar-buoy used for hywind, while highly stable, draws over 70m and had to be towed from Norway for installation due to a lack of suitable ports in Scotland. This is the main downfall of the spar design. Semi-submersible do not draw as much but are less stable (Hannon et al., 2019). This instability results in decreased power production. These problems drive up the overriding issue faced by offshore wind, the levelised cost of energy. This refers to the average net cost of electricity generation over the platform's lifetime. Current estimates indicate that the value for floating offshore wind is upwards of €150/MWh (Rinaldi et al., 2021). This compares to €80/MWh for onshore wind.

If floating offshore wind is to be deployed worldwide at a large scale, costs must be driven down. Wave tank testing forms a key part of the solution to high costs. Wave tank testing allows novel floating offshore wind platform designs to be assessed at a reduced scale and refined at a relatively low cost in a controlled environment. This gives more companies an entry point into the market to test their technologies. With increased competition and innovation in the sector, solutions to the most significant design challenges can be found, and costs can be driven down.

1.2 Problem definition

Wave tank testing allows model responses to be assessed in a controlled environment at a low cost (Müller et al., 2014). While it is highly beneficial, wave tank testing models at a reduced scale is not perfect, and errors are likely to occur during model fabrication and testing. Achieving the correct model properties at model scale can be quite difficult and can require complex distribution of lead ballasting inside the platform itself to arrive at the correct scaled physical properties.

When the model arrives in the lab, tests are performed to measure model properties such as the inertia, centre of gravity, mass, draft, and mooring line properties such a spring stiffness. The methods used to calculate the inertia, centre of gravity and mooring stiffness are as good as what can be achieved within the lab. However, there is a high likelihood of error within the methods, leading to uncertainties. The influence of these uncertainties on the platform responses must be quantified to understand the results obtained during wave tank testing fully.

When the model arrives in the lab, the model properties are often not as desired. Providing access points to the inside of the platform to move, add, or remove internal ballasting means that the errors in model properties can often be corrected. However, despite design features aimed at negating these errors, sometimes the model properties cannot be corrected fully.

This results in differences between the desired and actual model properties. Likewise, where springs are used in the mooring system, there is a high probability that the properties of the spring will not be correct. These differences are likely to influence the motion of the platform, and thus, they will affect the results obtained from testing.

Finally, while Froude scaling can scale down physical model properties, similarity is not achieved for turbine properties using this method. Froude scaling produces low Reynolds numbers. The lift and drag coefficients of the turbine blades are extremely sensitive to the Reynolds number. Consequently, the aerodynamic forces on the turbine rotor are out of scale when Froude scaling is directly applied (Azcona et al., 2014). One solution applied to this problem has been the use of wind emulation systems. Wind emulation systems emulate some of the key aerodynamic forces at model scale, ignoring the physical properties of the turbine while maintaining the overall physical properties of the platform and turbine as a whole. Wind emulation systems of varying levels of complexity have been developed over time. The ability of these wind emulation systems to correctly replicate aerodynamic forces will have a considerable effect on the platform response during testing. The effect that each wind emulation system has on platform motions is not yet known.

This research aims to quantify and determine whether uncertainties in model setup and model construction have a significant influence on the results obtained during an experimental wave tank testing campaign.

1.3 Research Objectives

This research aims to:

- Examine the uncertainties and errors associated with wave tank testing of floating offshore wind platforms.
- Quantify the effect that uncertainties and errors associated with the inertia and centre of gravity have on platform responses.
- Quantify the effect that uncertainties and errors associated with mooring line stiffness have on platform response.
- Quantify the effect that different wind emulation systems have on platform responses.

1.4 Outline of Thesis

Chapter 2 investigates some of the relevant literature and theory on floating offshore wind, wave tank testing and uncertainty analysis. Chapter 3 outlines the methodology used to conduct this investigation and explains the variations conducted. The method used for model design is also detailed in this section. Chapter 4 presents an analysis and discussion on the results obtained from testing and mentions some of the initial conclusions. Chapter 5 summarises the conclusions gathered from testing and suggests some future research that could be conducted to expand on what has been done in this study. Chapter 6 contains the references, and Chapter 7 gives all of the appendices.

2 Literature Review

This chapter summarises the motivation for the development of floating offshore wind platforms, highlights the challenges faced by developers and researchers, and emphasises how wave tank testing plays a vital role in overcoming these challenges. The theory and principles of floating platforms are presented. This chapter also discusses how uncertainty analysis can lead to more accurate and commercially beneficial testing campaigns. The challenges faced in conducting coupled wind and wave tank tests with floating offshore wind platforms are also explored.

2.1 Offshore wind

2.1.1 Background and History

Wind energy has been harnessed by humans for centuries (Kaldellis & Zafirakis, 2011). The first know evidence of the use of windmills dates back over 2000 years. Originally used by the Persians and then more recently found in the Netherlands and Mediterranean between the 14th and 19th centuries, primarily being used to grind corn and pump water (Kaldellis & Zafirakis, 2011; Pasqualetti et al., 2004; Shahrukh Adnan et al., 2016). Until the 17th-century, turbines faced a fixed direction, which would be dictated by local wind patterns. Large-scale implementation of wind energy first began at the beginning of the 18th Century. The “Pumping Jack” design, shown below in Figure 2, was mainly used to pump water; unlike previous designs, the direction the turbine faced changed with varying wind direction. Over 6 million windmills were constructed in the U.S before the beginning of the 19th Century (Shahrukh Adnan et al., 2016).

Figure 2 - The widely used American Pumping Jack

Since the "Pumping Jack", many different designs have been tested, such as turbines that have their rotation shaft transverse to the direction of the wind, also known as vertical access wind turbines (Darrieus, 1931), shown below in Figure 3 McDonnell Aircraft company also came up with the concept of the H-rotor wind turbine (Shown below in Figure 3, like Darrieus' turbines, the H-rotor was also a vertical axis wind turbine (VAWT) (Rogowski et al., 2020). While most large-scale modern turbines are no longer VAWTs, there has been a renewed interest in VAWTs for small scale power generation(Bahaj et al., 2007). This renewed interest can be attributed to lower maintenance demands with VAWT(Mohamed et al., 2015).

Figure 3(a) and (b) - The Darrieus Turbine and McDowell's H-rotor

Unlike the Darrieus and McDowell turbines, the modern wind turbine is a horizontal axis wind turbine (HAWT), based on one manufactured in Denmark at the end of the 1950s. This turbine became known as the Gedser turbine, named after the area it was installed. The turbine had a capacity of 200kW and ran for 11 years without maintenance. The modern turbine consists of 3 blades that power an asynchronous motor(Gustavo & Enrique, 2011).

Figure 4 - 200kW Gedser Wind Turbine

Since 1960, global efforts have been focused on increasing the electrical output from a particular wind turbine. In simple terms, this has been achieved by increasing the efficiency of the blades, increasing the radius of the blades and increasing the height of the turbine towers. There is a direct correlation between the radius of the turbine blades and the power output from the blades (Ackermann, 2005). Figure 5 below shows the development of wind turbine size and output over time.

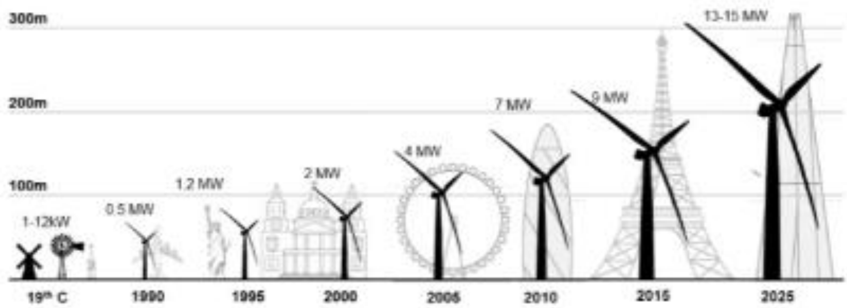

Figure 5 - Evolution of wind turbine power output and size over time(Pisano, 2019).

In the past 30 years, since 1990, there has been a 2800% increase in wind turbine power output. The world's biggest wind turbine blades are offshore wind turbines (Parnell, 2020). For example, the worlds biggest turbine, the SG 14-222 DD turbine, has a rotor diameter of 222m and can be boosted to a capacity of 15MW, and it is an offshore wind turbine (Siemens Gamesa, 2020).

Offshore wind turbines are not subject to the same restrictions that limit the size of onshore wind turbines. Many people favour wind turbines provided they are not located near where they live. Some of the main objections to onshore wind turbines are concerns arising due to noise and light pollution, and these issues restrict the size of onshore turbines, and these issues are not relevant offshore. Offshore wind platforms are built more than 15 kilometres from the coast, and consequently, the issues alluded to earlier in this section are no longer a factor(Esteban et al., 2011). At sea, there are no limitations with regard to transporting the turbine tower and blades to the installation location. On-land, most turbines are placed in remote locations, and so road access to the sites is generally poor, and aside from this, there is a limit to the size of the vehicles that can be used to transport the turbine. At sea, the turbines can be transported by specialist vessels capable of transporting far larger turbines than on land.

2.1.2 Reasons for Offshore Wind Renewable Energy.

Fossil fuels are a finite resource and will eventually run out. More importantly, however, the burning of fossil fuels releases carbon dioxide into the atmosphere. Carbon dioxide is a large contributor to the greenhouse effect and consequently to rising air and sea temperatures(IPCC, 2012). To combat this alternative, cleaner energy sources must be sought. Climate initiatives such as the EU Climate and Energy framework (European Commission, 2013) have forced governments to reduce reliance on carbon-based energy sources. By 2030, participating countries must reduce greenhouse gas emissions by 40%. Consequently, there is an urgent need to diversify energy sources. By 2030, Ireland aims to have renewable energy sources account for 70% of the overall energy production (IWEA, 2018). With Ireland's energy demands set to increase by 2030, this will not be achieved without significant investment (SEAI, 2017). At the moment, wind is Ireland's primary source of renewable energy. With a limited number of viable onshore wind sights remaining, Ireland's onshore wind capacity will have to increase. Offshore wind is a resource that has slowly become more and more popular across EU member states. Of the 192GW of electricity produced by wind in the EU, 22GW are from offshore wind. Figure 6 below shows that year on year, the installation of offshore wind is starting to catch up with onshore wind. While Ireland has the highest percentage of electricity produced by wind, it falls behind other European countries when it comes to offshore wind (WindEurope, 2021)

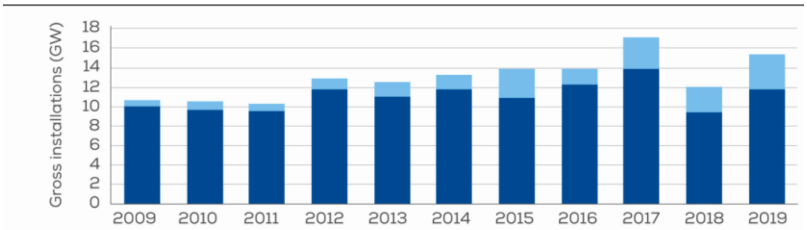

	2009	2010	2011	2012	2013	2014	2015	2016	2017	2018	2019
Offshore	0.6	0.9	0.8	1.2	1.5	1.5	3.0	1.6	3.2	2.7	3.6
Onshore	10.0	9.6	9.5	11.7	11.0	11.7	10.9	12.3	13.9	9.4	11.7
Total	**10.7**	**10.5**	**10.3**	**12.9**	**12.5**	**13.3**	**13.9**	**13.8**	**17.1**	**12.1**	**15.4**

Figure 6 - Gross installation of Wind Energy Converters, Onshore vs Offshore (WindEurope, 2019)

Offshore wind has enormous potential for Ireland due to a huge wind resource and large offshore territory. 10 km off the coast, sea surface winds are generally 25% higher than onshore winds. These high offshore wind resources can be utilized 2–3 times longer to generate electricity than onshore wind farms in the same period of time (Tambke et al., 2005). Surface roughness tends to be lower out at sea when compared with values onshore (L. Wang, J. Wei & Zhang, 2011). Wind speeds at sea are, on average, far higher and steadier than windspeeds on land, as illustrated in Figure 7. As per, Equation 1 wind speed has a significant bearing on turbine power output.

$$P_{avail} = \frac{1}{2}\rho A v^3 C_p$$

Equation 1

Where P_{avail} is the power available from a turbine(W), ρ is the density of air(g/m^3), A is the swept area of the turbine m^2, the swept area of the turbine is the area covered by the rotating turbine blades, v is the wind speed(m/s), and C_p is the power coefficient, C_p varies depending on the turbine design. Offshore wind turbines will have larger blades and increased wind speed, resulting in greater power output.

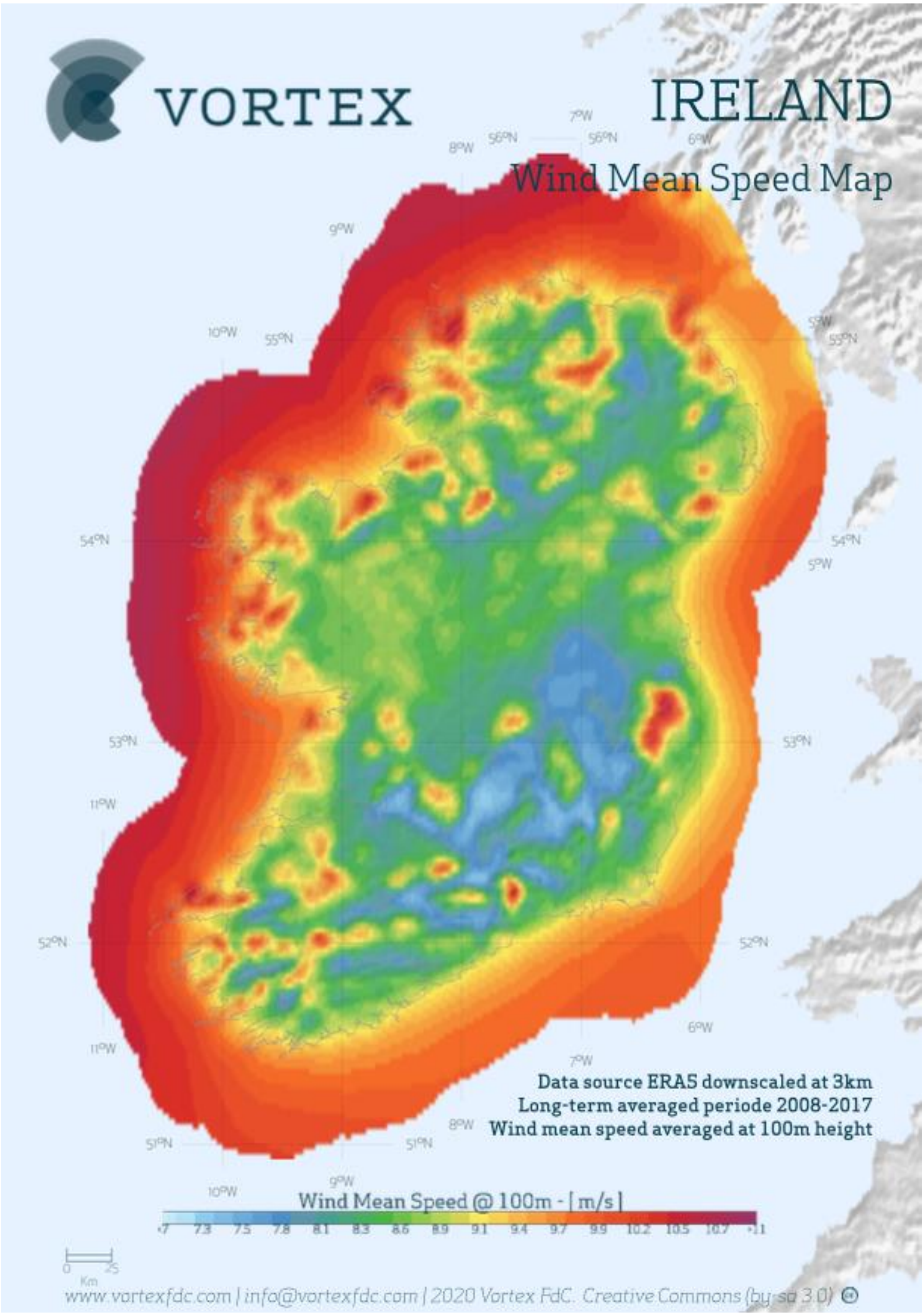

Figure 7 - Average windspeed(m/s) at a height of 100m Ireland(Vortexfdc, 2021)

The platform is the foundation upon which the wind energy converting turbine is placed. Offshore wind turbines can be split into two categories, bottom-mounted offshore wind turbines (BMOWTs) refer to a turbine that is placed on a fixed foundation and is suitable at depths below ~60m and floating offshore wind turbines (FOWTs) refers to a turbine that is placed on a floating foundation and is suitable for depths between 60m and ~2000m. This study focuses on FOWTs, and BMOWTs will not be discussed in detail. Floating turbines facilitate accessing a higher wind resource. Water depths in the Irish Atlantic coastal waters increase rapidly with distance from the shoreline.

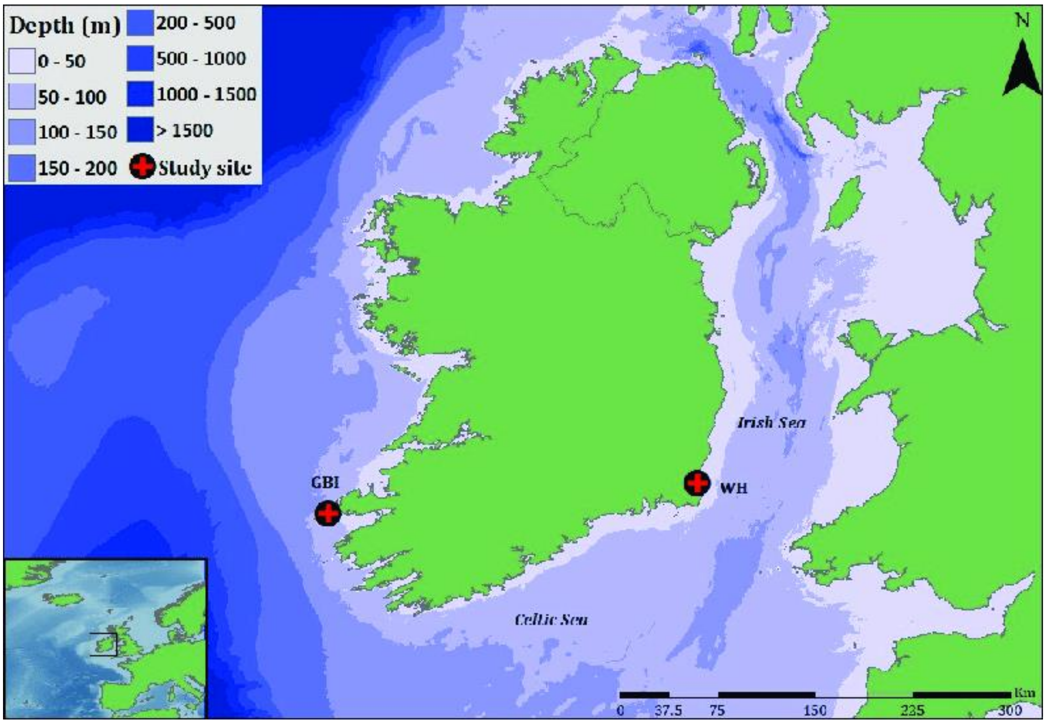

Figure 8- Variation in water depth along Irish coasts (Gosch et al., 2019)

Therefore, the opportunity for BMOWTs is limited to the Irish Sea (Musial et al., 2016). The technical potential of deep-water wind energy globally is 330,000TWh, four times greater than the shallow water resource (IEA, 2019). Exploiting this resource will go a long way to meeting, and potentially surpassing, renewable energy demands. The use of FOWTs is not without its challenges; if FOWTs are to become widespread, many challenges must be addressed and resolved. The challenges faced by FOWTs are addressed in more detail in 2.3.1.

2.2 Floating Platform Behaviour

2.2.1 Platform motions

Offshore wind platforms are subjected to a combination of aerodynamic, current and wave loads. The forces resulting from these loads and their interaction determine the platform motions. The aerodynamic loads of the FOWTs are extremely sensitive to any variations in the frequency and amplitude of the platform motion (Tran & Kim, 2015). The addition of aerodynamic loads significantly affects the structure's response to wave and wind loads.

Very simply, wind turbine blades work like an aeroplane wing or a helicopter blade, the shape of the blades is such that when wind flows across the blade. This creates a pressure difference between either side of the blade. This pressure difference produces a drag force in the direction of flow while also creating a lift force perpendicular to the direction of the flow. The lift force is a multiple of drag force and therefore is the relevant driving force for the turbine rotor (Ackermann, 2005). The platform's motion can cause an asymmetric inflow condition on the rotor blades. FOWT platforms experience the additional six degrees of freedom (6DoF) motions caused by wind and wave loads. The 6DoF are shown below in Figure 9, and these 6DoF describe the motion of the platform as the translation about the axes x, y, and z axes and the rotation about those axes. The translation motions can be described as surge (x), heave (z), sway (y), and the rotations can be described as roll (x), yaw (z) and pitch (y)

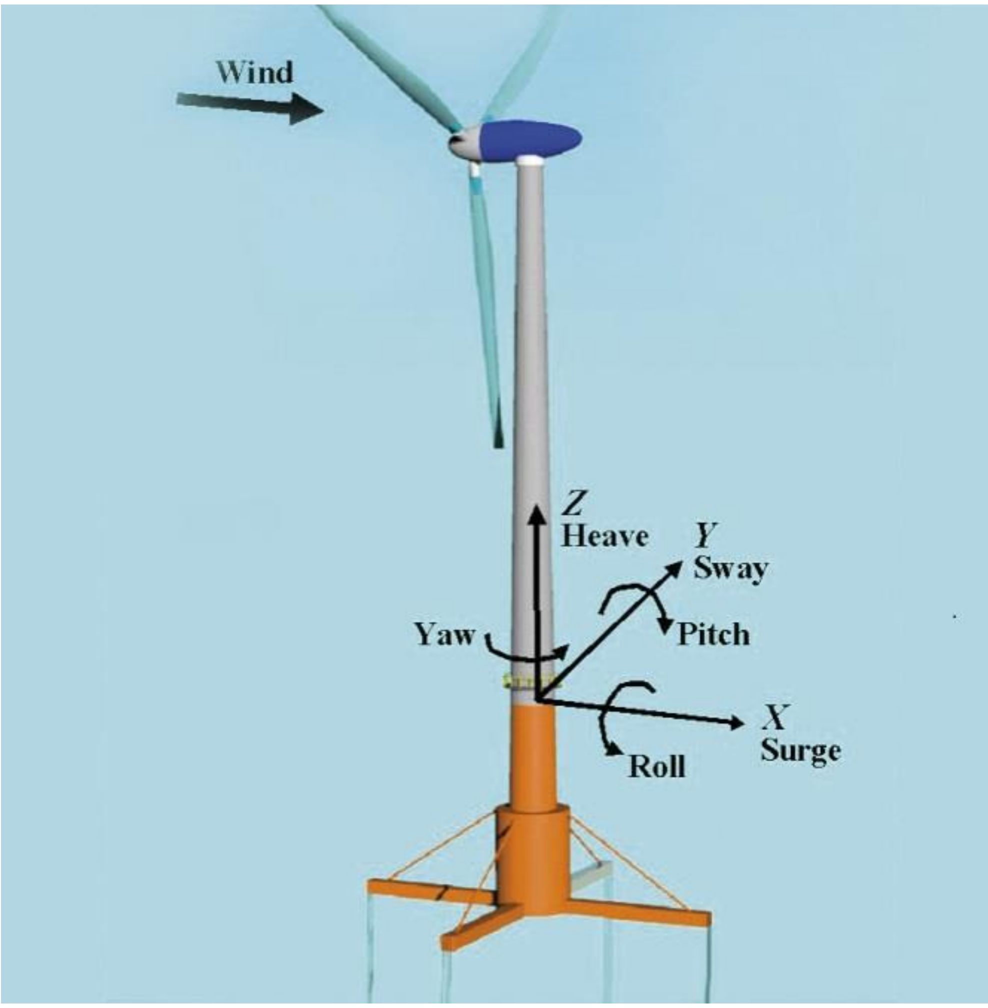

Figure 9 – The Six-Degrees-of-Freedom(6DoF)(Dvorak, 2021)

Gathering information on how these motions affect the turbine output is crucial in implementing a cost-effective design that is efficient at eliminating the most detrimental motions to turbine power output. (Lee & Lee, 2019) observed that pitch and surge motions negatively impacted turbine thrust force and power output to the greatest extent. All motions caused wake instability downstream, resulting in unsteady inflow conditions for turbines positioned downstream of the turbine. Reducing the pitch of a platform due to wave loading will reduce losses in power output (Tumewu et al., 2017). It is also essential to collect information on how the platform performs in different wave and wind conditions. Floating offshore wind turbines do not produce energy in extreme conditions. However, tests must be carried out to determine whether the floating structure and turbine will survive in the extreme environment in which it will be deployed.

2.2.2 Wave forces acting on FOWTs

Before the influence of aerodynamic loads on platform motions can be understood, it is important to understand the wave forces acting on the platform and the factors influencing the magnitude of its response. Ocean waves can be classified into three different types depending on the ratio of the wavelength, λ, and the water depth, h. For deep water waves, linear wave theory is valid until a wave steepness of 1:25. Wave steepness is the ratio of wave height to wavelength.

The two equations that describe the motion of a fluid are the Navier-Stokes Equation, derived from the conservation of momentum and the continuity Equation, derived from the conservation of mass. When considering wave body interaction, the velocity potential ϕ must satisfy the Laplace Equation, an output of the continuity Equation, the boundary condition at the seabed, at the free surface and on the submerged portion of the body (S_b). The velocity potential is given by

$$\phi_I = \frac{gH}{2\omega}\frac{cosh[k(z+h)]}{\cosh(kh)}\sin(kx-\omega t)$$

Equation 2

The velocity potential has been derived in (Dean & Dalrymple, 1991) along with the conditions it must satisfy.

The Laplace Equation is given by

$$\nabla^2\phi = \frac{\partial^2\phi}{\partial x^2}+\frac{\partial^2\phi}{\partial y^2}+\frac{\partial^2\phi}{\partial z^2}$$

Equation 3 – Laplace Equation (Martin et al., 2017)

The Bernoulli Equation, derived from the Navier-Stokes Equations, is given by:

$$p = -\rho\frac{\partial\phi}{\partial t} - \rho g z + p_{atm}$$

Equation 4 (Martin et al., 2017)

Where p is the pressure, ρ is the, g is gravity, and z is the displacement from the free surface. The derivation for Equation 3 and Equation 4, along with the boundary conditions needed to satisfy ϕ, are given in (Martin et al., 2017).

The velocity potential can be separated into three potentials, the incident potential, given in Equation 2, the diffraction potential, and the radiation potential.

$$\phi = \phi_I + \phi_D + \phi_R$$

Equation 5

The incident potential, ϕ_I, defines the flow of an incident wave when no model is present. The diffraction potential, ϕ_D, defines the flow of the diffracted waves from the presence of a fixed body and the radiation potential, ϕ_R, defines the flow of radiated waves due to an oscillating body in still water.

u is the generalised vector for a floating body:

$$\underset{u}{\rightarrow} = \underset{U}{\rightarrow} + \underset{\Omega}{\rightarrow} + \underset{r}{\rightarrow}$$

Equation 6

$$\underset{r}{\rightarrow} = [x, y, z]$$

Equation 7

$$\underset{U}{\rightarrow} = [U_x, U_y, U_z] = [u_1, u_2, u_3]$$

Equation 8

$$\underset{\Omega}{\rightarrow} = [\Omega_x, \Omega_y, \Omega_z] = [u_4, u_4, u_6]$$

Equation 9

where $\underset{r}{\rightarrow}$ is the position vector, $\underset{U}{\rightarrow}$ defines the translation velocities in x, y and z, and $\underset{\Omega}{\rightarrow}$ defines the rotational velocities about x, y and z.

Mode #	Mode
1	Surge
2	Sway
3	Heave
4	Roll
5	Pitch
6	Yaw

Table 1 – Mode numbers for each motion

If **n** is the generalised normal vector, then

$$n = [\underset{n}{\rightarrow}, \underset{r}{\rightarrow} x \underset{n}{\rightarrow}]$$

Equation 10

$$\underset{n}{\rightarrow} = [n_x, n_y, n_z] = [n_1, n_2, n_3]$$

Equation 11

$$\underset{r}{\rightarrow} x \underset{n}{\rightarrow} = [n_4, n_5, n_6]$$

Equation 12

By solving the velocity potentials for each problem, the total velocity potential can be expressed as:

$$\phi(t, \underset{r}{\rightarrow}) = Re[\hat{\phi}\left(\underset{r}{\rightarrow}\right). e^{j\omega t}]$$

Equation 13

Where ω is the angular frequency of the wave, t is the time and $\hat{\phi}$ represents the complex amplitude of the velocity potential. By filling Equation 13 into Equation 14 and assuming the platform is initially in its equilibrium position, the pressure of the fluid around the body can be calculated.

$$p = -\rho Re\left[\mathrm{j}\omega\hat{\phi}\left(\underset{r}{\rightarrow}\right). e^{j\omega t}\right] - \rho g z$$

Equation 14

The hydrodynamic and hydrostatic forces and moments can be obtained by integrating Equation 14 over S_b. Hydrodynamic forces result from water flowing against or around the surface of a model.

$$\underset{F}{\rightarrow} = \iint_{S_b} p \underset{n}{\rightarrow} dS$$

Equation 15

$$\underset{M}{\rightarrow} = \iint_{S_b} p(\underset{r}{\rightarrow} x \underset{n}{\rightarrow}) dS$$

Equation 16

$$\boldsymbol{F} = \iint_{S_b} p\boldsymbol{n} dS$$

Equation 17

Hydrodynamic forces acting on the model can be categorised into two types, the excitation force and the radiation force. The excitation force is calculated in Equation 14, where only the incident and diffraction potentials from Equation 13 are considered. The radiation is the force that generates waves from the oscillation of a platform in still water.

$$F_e = -p \iint_{S_b} Re\left[\mathrm{j}\omega\hat{\phi}\left(\underset{r}{\rightarrow}\right). e^{j\omega t}\right]\boldsymbol{n}dS$$

Equation 18

$$F_r = p\omega^2 \iint_{S_b} Re\left[\sum_{i=1}^{6} \hat{q}_i\hat{\phi}_i\left(\underset{r}{\rightarrow}\right). e^{j\omega t}\right]\boldsymbol{n}dS$$

Equation 19

The radiation force for each model, j, can be further simplified to:

$$F_{r,j} = \sum_{i=1}^{6} -a_{ji}(\omega)\frac{\partial^2 q_i}{\partial t^t} - b_{ji}(\omega)\frac{\partial q_i}{\partial t}$$

Equation 20

The terms a_{ji} and b_{ji} are the frequency-dependent 'added mass' and 'radiation damping' coefficients. The index *ji* denotes the coefficient in the jth mode, which is caused by the oscillation in the ith mode.

The restoring force, referred to previously as the gravitational storing force or buoyancy force, comes from the integration of hydrostatic pressure. Integration of hydrostatic pressure yields a 6 x 6 matrix, $\boldsymbol{K}_h$, called the hydrostatic stiffness matrix.

$$\boldsymbol{F}_h = -\rho g \iint_{S_b} z\boldsymbol{n}dS = -\boldsymbol{K}_h \underset{\boldsymbol{q}}{\rightarrow}$$

Equation 21

Finally, the total wave force on a floating system is the sum of the excitation, radiation, and hydrostatic forces.

$$\boldsymbol{F}_{wave} = \boldsymbol{F_e} + \boldsymbol{F_r} + \boldsymbol{F_h}$$

Equation 22

The motion of the platform is a consequence of both the force enacted on it by the waves and the design of the platform itself. The motion of the platform due to wave-induced forces can be explained like the motion of a mass-spring system.

$$(m + a)\ddot{x} + b\dot{x} + cx = F_{wave}$$

Equation 23

Where x is the displacement of the platform, a is the motion-induced added mass, b is the radiation damping coefficient, and c is the linear damping coefficient. Under regular wave excitation, the excitation force can be represented by the harmonic excitation function $F_e = f_e e^{j\omega t}$, where f_e is the amplitude, j is the imaginary unit, and ω is the wave frequency. Using the method of undetermined coefficients, this can be converted to x = |x|.$e^{j\omega t}$. Filling into Equation 23, we get.

$$-\omega^2(m + a_w).x - j\omega b_w.x + c.x = F_{wave}$$

Equation 24

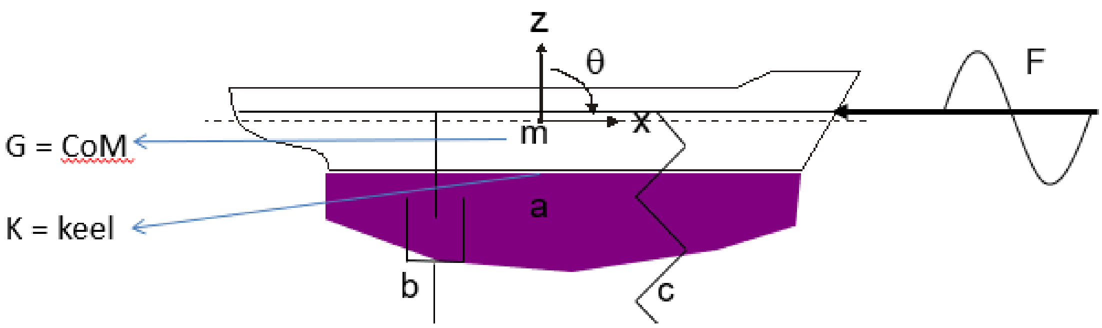

Figure 10 – Ship as a mass-spring system

The effect of aerodynamic forces, coupled with hydrodynamic forces, on the motion of FOW platforms is highly complex. Platform motions affect the load experienced by the turbine, and the load experienced by the turbine affects the platform motions (Huang & Wan, 2020). The effect of turbine loads on platform motions is of particular interest to this report. The average pressure over the entire swept area of the turbine blades, P_H, is:

$$P_H = \frac{1}{2}\rho C_{FB} {V_R}^2$$

Equation 25

where ρ is the air density (kg/m^3), C_{FB} is a coefficient, it can be taken as 0.888 (Chen et al., 2019), and V_r represents the wind speed. The horizontal load at the top of the tower F_H is found by multiplying P_H by the area of the blades. The load on the tower F_{to} is found using:

$$F_{to} = k_1 k_2 a {v_t}^2 A_w$$

Equation 26 (Chen et al., 2019),

where k_1 is the wind load shape factor (approx. 0.5 for a cylinder), k_2 is the wind pressure height variation coefficient, a is the wind pressure coefficient (usually 0.613), v_t is the design wind speed (m/s), and A_w represents the projected windward area of the tower.

2.2.3 Magnitude and frequency of platform motions

Section 2.1.1 highlighted the forces influencing platform motions. The platform design dictates the extent to which a platform is displaced by any wind and wave load combination. Where most wave energy converters (WECs) seek to maximise the response of the platform to wave loads, floating wind platforms seek to limit platform motions. Heave motions are primarily limited by the hydrostatic stiffness of the platform in heave C_{33} (N/m).

$$C_{33} = \rho . g . A_{wl}$$

Equation 27

where ρ is the density of saltwater (kg/m^3), g is the acceleration due to gravity (m/s^2), and A_{wl} is the waterline area of the platform (m^2). Heave motions are also dictated by the vertical stiffness of the mooring system employed.

Roll and pitch motions are also linked to the hydrostatic stiffness of the platform in roll C_{44} and pitch C_{55} (N.m/rad). The hydrostatic stiffness in roll and pitch is largely dictated by the metacentric height of the model. The metacentric height is a measure of the initial static stability of a floating body. It is the distance between the centre of gravity of a floating body and its metacentre. The metacentre is the point about which the floating body will rotate when given a small angular displacement.

$$GM = KB + BM - KG$$

Equation 28

where K is the keel, the bottom-most part of the platform, B is the centre of buoyancy, the centroid of the immersed part of the floating body. G is the centre of gravity, the theoretical point through which the force of gravity appears to act, and M is the location of the metacentre.

Hydrostatic stiffness in pitch, C_{55}, is calculated using the formula:

$$C_{55} = \rho . g . \nabla . GM$$

Equation 29

where ∇ is the displaced volume (m[3]), and *GM* is the metacentric height (m).

Thus, the natural periods/eigenfrequencies are found using the following formulas

$$\omega_0 = \sqrt{\frac{C}{M}}$$

Equation 30

where ω_0 is angular rotation (rad/s), *M* is the mass, and *C* is the stiffness.

$$T_0 = \frac{2\pi}{\omega_0}$$

Equation 31

Equation 31 gives a general equation for the natural period a platform for any of the 6DoF.

$$T_3 = 2\pi.\sqrt{\frac{{RG_{33}}^2.\rho.\nabla + A_{33}}{\rho.g.A_{wl}}}$$

Equation 32

Equation 32 gives the formula for the natural period in heave. where RG_{33} is the radius of gyration of the model about the z-axis and A_{33} gives the added mass in heave of the platform.

$$T_{55} = 2\pi.\sqrt{\frac{{RG_{55}}^2.\rho.\nabla + A_{55}}{\rho.g.\nabla.GM_L}}$$

Equation 33 (Esber et al., 2019)

Equation 33 gives the formula for the natural period in pitch. GM_L is the longitudinal metacentric height. If the natural period in roll is calculated, GM_T should be used. The indexes 3 and 5 have been explained in . A_{55} is the added mass in pitch (kg/m^2). (Esber et al., 2019) derived that the magnitude of pitch response is proportional to the metacentric height. This is useful in terms of platform design. Pitching reduces the power output. An inclination of approximately 10° can reduce the power output by over 15%. A 5° reduction in platform inclination can reduce losses in power output by nearly 10%.

The natural period in surge is largely dependent on the stiffness of the mooring system that holds it in place. Suppose the stiffness of the mooring system is increased while all other model properties remain constant. In that case, it can be expected that the period of oscillation will decrease and vice versa. During wave tank testing, springs are often used to replicate mooring stiffnesses at model scale; An increase in spring stiffness is also likely to dampen down the magnitude of platform surge. The relationship between the surge natural period T_k and spring stiffness is shown in Equation 34 below, the general formula for the natural period of a platform. This applies to all other 6DoF.

$$T_k = 2\pi \sqrt{\frac{I_{kk} + A_{kk}}{C_{kk}}}$$

Equation 34

For Equation 34, I_{kk} is either mass or inertia and and A_{kk} is either added mass or added moment for the motion of interest respectively, and C_{kk} represents the stiffness in the k^{th} degree of freedom. The stiffness is made up of both the hydrostatic stiffness of the platform and the mooring stiffness.

Understanding the theory and formulae behind the forces and the design factors that influence platform motions go a long way to understanding what takes place during wave tank testing. It also facilitates a post-mortem of the results to be completed to improve upon some of the design issues that came up during the testing campaign. However, it is essential to note that theoretical relations are just that, and they alone cannot be used to assess device performance; this is why wave tank testing is completed in the first place.

2.3 Main Types of Offshore wind Platforms

Three main categories of FOWTs will be discussed in this section: the spar-buoy, the semi-submersible and the tension leg platform (TLP), shown below in Figure 11. The industry is still immature, and testing is ongoing for new designs. Between them, the principles of design of these three main categories of FOWT explain the principles of design on all the latest technology entering the sector.

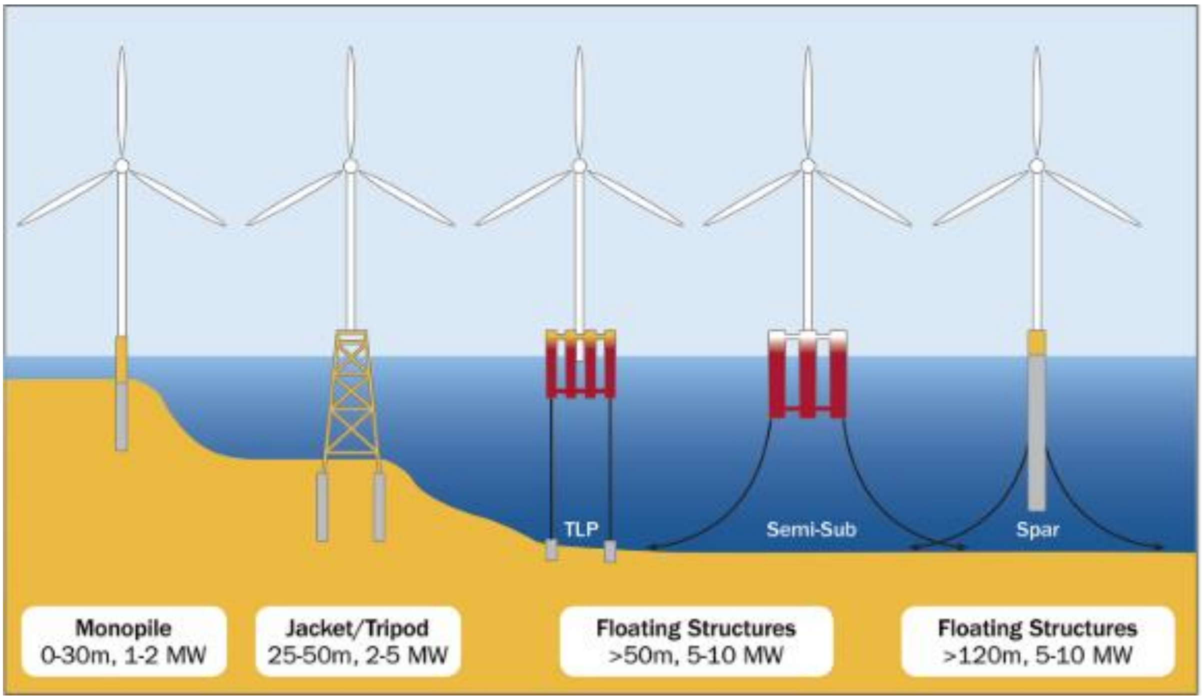

Figure 11 - Types of fixed and floating offshore wind foundations (Bailey et al., 2014)

Spar-buoy platforms, shown below in Figure 12, consist of a deep and relatively narrow substructure that is ballasted heavily to keep the centre of gravity below the centre of buoyancy and to provide a restoring moment for motion resistance (Ghigo et al., 2020). The concept is based on technologies deployed by the oil and gas industry at depths of over 2000m. Examples include a platform used by Shell in the Gulf of Mexico (Shell, 2020). The spar-buoy design is simple, highly stable, effective at preventing wave-induced motion and has a low installed mooring cost. Its mooring system is usually catenary or taut, and the line materials generally used are steel cables, anchor chains or fibre ropes (Butterfield et al., 2007). Catenary moorings consist of long steel chains and or wires whose weight and curved shape holds the floating platform in place. The lower section of the mooring chain rests on the seafloor; this supports the anchor and acts as a counterweight to platform motions in stormy conditions. Catenary moorings are relatively simple to install compared with taut-leg configurations. However, they have a large footprint, of which a large amount is resting on the seafloor, resulting in substantial disruption to the seafloor (James & Marc Costa Ros, 2015). Spar-buoy substructures must be extremely deep and heavy to provide the required restoring moment to keep the turbine upright. The 10,000-tonne Hywind Scotland substructure was 91m deep, with a draught of 78m and 13m above the waterline (Equinor, 2020). Due to this large draft and weight, very few ports have the water depths and infrastructure necessary for in-shore assembly. The turbine and platform had to be assembled in full in Norway and then undertook a 4-day tow to their site off the northeast coast of Scotland due to a lack of suitable ports nearby. In the quest to harness stronger winds far offshore, long-distance tow-outs are likely. Long-distance tow-outs are high risk as they require a long weather window that often is not achievable except in the calmest weather; consequently, a shorter towing operation is preferable. At present, the draft of spar-buoy platforms prevents their large scale deployment for offshore wind projects. Ireland's deepest port is located on the west coast of Ireland in Foynes, Co. Limerick. With a maximum quayside depth of just over 10.5m and a maximum depth of 30m in the estuary, port installation of spar-buoy platforms would not be feasible there or at any other ports on the island of Ireland (Spfc.ie, 2021).

Figure 12 – Hywind wind farm in Scotland with a spar-buoy floating platform (Equinor, 2020)

TLPs consist of a structure with ample buoyancy restrained through a tension leg mooring system. When inclined, the windward cable(leg) is tauter than the leeward leg, creating a restoring moment to counteract motions due to wind and wave loads (ETI, 2015). TLPs have a low mass and can be assembled nearshore or on the dry dock; however, a complex mooring system with high loads results in more complex installation and higher maintenance costs (Heidari, 2017). TLPs are more suitable for assembly in shallow ports. TLPs have an installed draft of about 30m, but the portside depth is a lot less. TLPs are assembled portside and transported to the site using a specialist vessel, where they are then pulled down to the required draft. The taut-leg configuration provides excellent stability; however, high vertical loads on the mooring lines means that the feasibility of these moorings is site-dependent because installation is limited to when specific seabed requirements are met (Hannon et al., 2019). The TLP is generally considered to be among the least developed floating foundations designs(DNV GL, 2018). Even so, the TLP was one of the first floating foundations to be installed. The Blue H technologies TLP, shown in Figure 13 below, was 560-tonne TLP tested between 2008 and 2009 (Blue H Technologies, 2017). The Pelastar TLP concept was designed for 6MW and planned to be scaled up to 10MW, but the concept has not yet been tested at full scale (Hurley & Nordstrom, 2014)

Figure 13 – Blue H Technologies TLP concept tested in 2008 (Blue H Technologies, 2017)

The semisubmersible design achieves stability by exploiting the buoyancy force, and this is achieved through a large waterplane area. When the platform inclines in any direction, a large buoyancy force is induced, which creates a large enough restoring moment to counteract the wind inclining moment (Hannon et al., 2019). Semisubmersible platforms are suitable for nearshore assembly, can be easily towed to the farm and have a low installed mooring cost. However, wave-induced motions are higher, reducing power production. Fabrication is more complex and expensive than other designs (ETI, 2015). Like certain spar-buoy platforms, semisubmersible platforms use catenary moorings. Semi-submersible platforms have been deployed at full-scale across Europe. The WindFloat Atlantic development, first installed in 2019, consists of three 8.4MW turbines placed on top of the Windfloat semi-submersible foundation, shown below in Figure 14. The platforms have been placed in a water depth of 100m at a distance of 20km from shore (PrinciplePower, 2019). The same company provided six platforms used for a 50MW development located 15km off the coast of Aberdeenshire, Scotland, in a water depth of between 60 and 80 metres. It is the worlds largest floating offshore wind farm (PrinciplePower, 2021).

Figure 14 – Windfloat Atlantic development off the coast of Portugal with semi-submersible foundation (PrinciplePower, 2019)

2.3.1 Platform design issues

Floating offshore wind is a rapidly maturing technology. Recent projects in Scotland, France, Spain, Japan, and Portugal have further solidified the viability and potential of floating offshore wind (IEA, 2019). While locating wind turbines out to sea eliminates some of the issues faced by land-based turbines, it does present unique challenges.

A sizeable proportion of the costs incurred over the lifetime of a FOWT is capital costs. Capital costs include connection to the grid, moorings, the platform, and the turbine. For fixed offshore projects, operation and maintenance costs can be 25-30% of the total lifecycle costs (Röckmann et al., 2017). Recent studies suggest that operation and maintenance for floating foundations would take up a lower proportion of the overall cost than fixed foundations, with operation and maintenance accounting for between 18 and 26% of the overall costs

(Katsouris & Marina, 2016). Offshore maintenance and operational costs are far higher than onshore for several reasons. Annual maintenance of 24h per turbine must be completed by three technicians with the aid of a small maintenance vessel. These vessels are expensive, and the cost of skilled labour is high. In addition to this, a subsurface inspection has to be undertaken every three years, and extensive preventative maintenance must be carried out every ten years (Myhr et al., 2014). For extensive repairs, the use of a crane vessel will be required. All maintenance work comes at a high cost, increasing with distance from the shoreline.

During these maintenance periods, turbines will not be operational, resulting in losses in power production. (Myhr et al., 2014) suggested that loss of power production due to downtime of FOWT during maintenance is between 6.2% and 6.6%. Adverse weather means that maintenance and repairs are dictated by weather windows that allow for safe access to the platform. (Sahnoun et al., 2015) suggested that access maximum wind speeds are as low as 8m/s with a significant wave height of 1.5m. If adverse weather conditions restrict access to the offshore wind site, downtimes may become significantly increased, while the likelihood of failures is also increased due to exposure to more extreme weather conditions (Seyr & Muskulus, 2019).

Most ports do not have the necessary infrastructure and specifications to build, service and launch offshore wind farms. Analysis of 96 European ports suggested that very few ports, other than a few in Norway, Spain, and Scotland, were currently equipped to accommodate all the requirements for the construction of large-scale Floating wind farms (James & Weng, 2018). Criteria for suitability is determined by draught (water-depth), quayside area, wet storage, onshore set-down area and crane capacity. Most turbines are assembled at or in the waters near the port using enormous machinery and specialised cranes and then towed out to sea (Scheffler et al., 2017). At site, semisubmersible platforms and TLPs draw ~20m and ~30m, respectively (Porter & Phillips, 2016). However, at the port, the platforms are not fully ballasted; consequently, they draw significantly less, approximately 10m. Finding ports with depths to suitable semisubmersible and Tension Leg Platforms is still challenging, particularly in Ireland, where the maximum quayside depth at any port in the Republic of Ireland is just over 10m (Spfc.ie, 2021)

Designing a platform that effectively reduces motions due to wind and wave loads while maintaining low costs and practical platform size is incredibly challenging. Despite the challenges, there is considerable promise that low cost, efficient turbines can be achieved, with wave tank testing facilitating accelerated technological development in the industry. In recent years, multiple projects have been installed (Equinor, 2020; PrinciplePower, 2019, 2021), all of which have been described above, and there are many more to come over the coming decade (Hannon et al., 2019). In Cork, Ireland, the 1.3GW emerald floating offshore wind farm is planned for completion in 2030, with the potential to power over 1 million homes (emeraldfloatingwind, 2020). In Norway, an 11 unit 88MW floating wind farm is planned for completion in mid-late 2022 and will power offshore oil and gas platforms in the North Sea (Equinor, 2021a).

2.4 Wave Tank Testing

2.4.1 Why wave tank testing

Wave tank testing helps assess the performance of a design in a controlled and accessible environment at a fraction of the cost of sea trials (Payne, 2008). Wave tank testing is necessary during the early stages of FOWT development because obtaining high-quality experimental data is critical to validate the performance of any WEC or offshore wind platform (Müller et al., 2019). Wave tank testing provides an ideal environment to collect this data. Modern wave tanks are equipped with all the instrumentation necessary to collect data on platform motions, aerodynamic performance, wave motions, mooring loads, and various other properties to ensure nothing is left to chance.

Wave tank testing is an effective way at de-risking the design of a FOW platform. Platform suitability and efficacy can be assessed at a small-scale, where the risk of technical and financial mishaps is far lower, all the while enabling concentrated learning and platform optimisation. Conducting similar tests in an ocean environment is far more expensive and challenging. At the same time, it also leaves the platform at the mercy of ocean conditions which are entirely uncontrollable (Steven Hughes, 1993). Sea trials are undeniably important towards the latter stages of offshore wind technology development; however, multiple iterations of wave tank testing should be completed before then.

The floating offshore wind industry is still relatively nascent. Wave tank testing allows smaller companies with low initial financial backing to enter the market. There has been a struggle to find a cost-effective design that effectively reduces wave-induced motions and that is practical for port-side assembly. Wave tank testing allows innovative platform designs to be assessed and improved throughout an iterative testing process, and developers can use the test findings to validate platform performance and efficacy and extrapolate results to assess full-scale performance and suitability. There will not be a "one size fits all" type solution to design offshore wind energy platforms. Depending on the installation location, certain platform designs may be more suitable than others. Each platform will have to be specifically tailored to the turbine mounted on the platform and the loads placed upon it as a result. Extensive wave tank testing will be crucial for platform validation and modifications throughout the design process. Successful tests at a reduced scale can help secure funding for further testing and technology development down the line.

Wave tank tests of floating offshore wind platforms are conducted to obtain the full system dynamics in all occurring load situations for full-scale prototypes. It also aids in the validation of numerical models for a particular design (Müller et al., 2014). Numerical simulations are used for analysing the coupled dynamics of FOWTs, and these models must be validated with reduced-scale tests. Numerical models are based on theoretical formulae, and there are often differences between what is expected to happen in theory and what happens during testing. Testing helps identify these differences and improve the accuracy of numerical models (Pham & Shin, 2019).

One of the many challenges faced by the FOW industry is reducing the cost of offshore wind technology. The term levelised cost of energy (LCOE) measures the average net present cost of electricity generation for a generating plant over its lifetime. The LCOE is an effective way to consistently compare the cost of electricity generation. The LCOEs for current projects are as high as €170/MWh, but most forecasting models predict a sharp decrease in the LCOE for FOWT over the coming years. For example, the LCOE for a 1GW FOW farm off the Irish coast in 2035 is estimated to be between €51/MWh and €107/MWh, depending on the installation location (Cummins & McKeogh, 2020). The LCOE of floating offshore currently wind does not compare well with other renewable energy sources. The hywind project mentioned above in section 2.3 has an LCOE of €164.6/MWh. The Windfloat project, a 25MW wind farm using semisubmersible platforms, had a slightly higher LCOE of €189.2/MWh(Ghigo et al., 2020). The LCOE of offshore wind platforms is comparably higher than the LCOE worldwide average for onshore wind, which is €77/MWh for large onshore wind projects (IWEA, 2018). Reducing costs will go a long way to increasing the worldwide capacity of FOW. In Japan, most of the offshore wind potential lies in deeper water, lending itself to the use of FOWT (IEA, 2019). However, high costs mean that Japan is unlikely to tap into this resource until costs reduce significantly. Like any other industry, increased competition will reduce the cost of offshore wind turbines (The Crown Estate, 2012). An increase in the turbine size will likely result in a reduction in costs. Indications point to the use of 15MW FOWT by 2030 and 20MW turbines by 2037. There is a danger that turbine technology is outpacing the technology needed to support them (Floating Offshore Wind Centre of Excellence, 2021). Wave tank testing will be critical to developing platforms capable of supporting such enormous turbines. Wave tank testing is central to reducing the LCOE of offshore wind energy, as it drives competition and allows newer, potentially cheaper technologies to enter the market.

2.4.2 Scaling for wave tank testing

Scaling model properties for wave tank testing of FOWTs can present challenges. Froude scaling is widely used to scale model properties for all forms of wave tank testing (Fowler, Kimball, Iii, et al., 2013). While viscous forces affect FOWT platform hydrodynamics, they are considered small compared to the inertia effects at both model scale and full scale (MaRINET1, 2015). Viscous effects exist mostly in the thin boundary layer around floating bodies (J. N. Newman, 2017). The Froude number, from which the method of Froude scaling is derived, is the ratio of Inertial forces to gravitational forces. It is given by the formula.

$$Fr = \frac{U_m}{\sqrt{gD}}$$

Equation 35

where U_m is the mean velocity in (m/s), g is the acceleration due to gravity (m/s^2), and D is the hydraulic mean depth. U_m has been used in lieu of the conventional "U" to avoid any confusion with the notation for total uncertainty. When carrying out Froude scaling, model properties are converted from full-scale to model-scale by dividing the quantity of interest by the appropriate scaling factor. In Table 2 below, λ is the model scale; if the scale was 1/50, then λ would be 50.

Variable	Unit	Scale factor
Length	[m]	λ
Wave Height	[m]	λ
Wavelength	[m]	λ
Water depth	[m]	λ
Time	[s]	$\sqrt{\lambda}$
Wave Period	[s]	$\sqrt{\lambda}$
Force	[N]	λ^3
Structural Mass	[kg]	λ^3
Pressure	[Pa = N/m^2]	λ
Moment	[Nm]	λ^4

Table 2– Froude scaling factors (Samuel, 2019)

Reynolds scaling is the standard for testing aerodynamic models. The lift and drag coefficients for wind turbine blades are very sensitive to Reynolds number. The Reynolds number is the ratio of inertial forces to viscous forces. It is given by the formula

$$Re = \frac{\rho U_m D}{\mu}$$

Equation 36

where U_m is the mean velocity (m/s), ρ is the density of water (m^3/s), μ is the viscosity of water (Pa.s), and the notation for D is the same as in Equation 35.

The challenge in testing scaled floating wind turbines is applying Froude scaling for the aerodynamic load of the wind. There must be a similarity in the hydrodynamic and aerodynamic loads based on the Froude and Reynold scaling laws. However, the two are incompatible at the model scale (Pham & Shin, 2019).

There are two main approaches to simulating the aerodynamic forces during wave tank testing. The 'simplified approach' and 'the full approach' (Gueydon et al., 2020). The full approach involves using a scaled rotor, whereas, in the simplified approach, the wind turbine is replaced with something to emulate the forces. Performance scaling is the best developed full approach method for testing FOWTs (Fowler, Kimball, Thomas, et al., 2013). Very basically, performance scaling involves designing a blade profile suitable for the flow conditions of a Froude scaled wind; it has been explained in greater detail in (Bozonnet et al., 2017; Schünemann et al., 2018). Geometrical scaling refers to a geometrically scaled rotor in wind speed, adjusted to achieve the desired thrust. Geometrically scaled turbines have proved unsuccessful in the past (Gueydon et al., 2020).

The simplified approach has often been preferred due to its simplicity and the ability to simulate aerodynamic forces without the need to create wind, which can be complicated to do correctly within the confines of a tank hall. The most basic method of simulating thrust uses a suspended weight and a pulley system. A non-elastic wire is attached at the hub location, extended horizontally to a pulley, and down to a vertically hanging mass (MaRINET1, 2015). The method was used in (Matha et al., 2015), and it was found that the use of the pulley system had limitations. The study concluded that due to the inertial forces experienced by the suspended mass and the friction of the line over the pulley, there were significant deviations in the thrust force experienced by the platform depending on the platform motions. It was also found that motions were significantly dampened. However, (MaRINET1, 2015) determined that the method was suitable and cost-effective in early-stage testing.

A thruster or fan emitting a constant thrust has been widely used to simulate turbine thrust. The geometry and mass of the rotor are not considered, provided the overall model properties are correctly scaled. This may involve placing masses at the top of the tower to correct inertia and CoG values. The method consists of a fan running at a constant speed to generate a pre-defined value of thrust (Oguz et al., 2018). The force delivered by this thruster is perpendicular to the virtual wind turbine rotor plane and is applied at the hub location. In an actual wind turbine, the forces and moments applied would be in 3 directions rather than just one. However, the thrust is considered the most important wind component for design purposes (Gueydon, Judge, O'shea, et al., 2021). The thrust force causes horizontal drift, which affects the tension in mooring lines. The force is applied a large distance from the CoG, and thus, the moment around the CoG is large. This can affect the submerged geometry of the platform, and consequently, the platform motions. The thruster must first be calibrated before use to ascertain the relationship between thrust and RPM. It can be helpful to attach an Arduino to the thruster so that the thruster can be controlled remotely from the control room, as described by (Gueydon, Judge, O'shea, et al., 2021). Arduino is an open-source electronics platform based on easy-to-use hardware and software. Arduino boards can read inputs and turn them into outputs. One limitation of the constant thruster is that, like the weighted pulley, it only accounts for the thrust force, and the thrust remains constant throughout the test, which is not a realistic wind condition in an ocean environment.

The development of the software in the loop (SiL) system has improved the accuracy of wind emulation during wave tank testing. The primary advantage of the SiL system is that aerodynamic forces are altered constantly throughout each wave run. The setup consists of a fan installed at the hub height that is powered by an electric motor. In the initial SiL system, the thrust was provided by a ducted fan (Azcona et al., 2019).

Figure 15 – Impeller Blade used for the first iteration of SiL (Azcona et al., 2019)

However, in subsequent designs, the thrust is provided by a drone with four propellers (Pires et al., 2020). The most recent iteration of the system has six propellers, with two blades added to simulate rotor torque, in addition to the simulation of rotor thrust. The main limitation of the initial design, with the ducted fan, is that the rotor moments caused by aerodynamic effects such as imbalances, wind shear, pitch failures, misalignments, or gyroscopic effects are not captured. The version described in (Pires et al., 2020) seeks to overcome those limitations. The SiL computes the correct rotor forces using a numerical model fed in real-time by the measured platform motions. The real-time simulation of the rotor aerodynamics provides the thrust force considering the effect of turbulent wind and control actions. As the simulation is coupled with real-time motion, the introduced thrust also accounts for aerodynamic rotor damping. The SiL system developed by CENER has been applied with great success to multiple test campaigns (Azcona et al., 2019; Pires et al., 2020). Figure 16 below summarises the process applied for the SiL system.

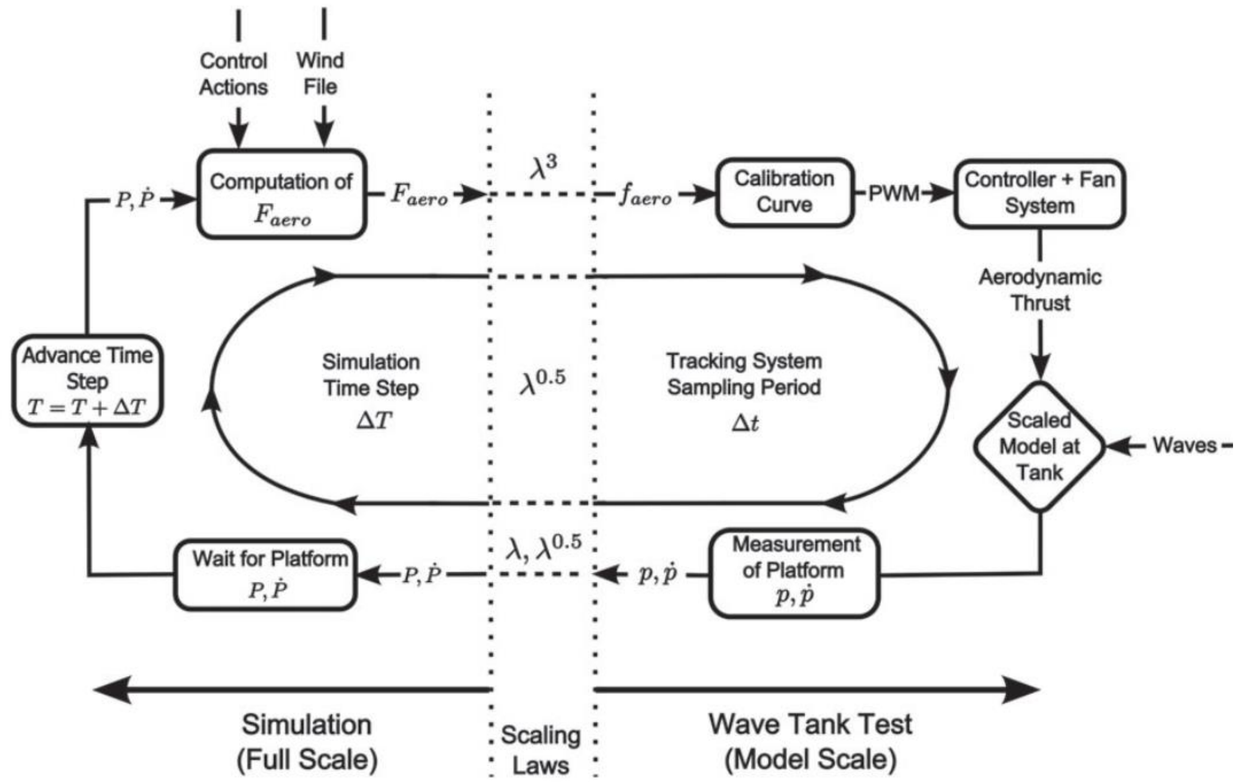

Figure 16– Diagram of the SiL method (Azcona et al., 2019)

Like wind turbines, all mooring line properties cannot be scaled correctly using Froude scaling. It is extremely challenging to correctly scale all mooring line properties like line diameter, line stiffness, and mass per unit length (Murphy et al., 2015). Attempts at achieving dynamic similitude between the full-scale model and testing model are given in (Bergdahl et al., 2016; Papazoglou et al., 1990). A simpler approach is to correctly scale a key mooring line property while altering the other ones to achieve the correct value for the key property. The key property will depend on the mooring system employed during testing. For a catenary system, where the tension in the line is provided by the weight of the line and the length of the line along the floor, the mass/unit length would be a dominant factor. In a linear spring system, the overall line tension could be the dominant factor.

In many cases, tank dimensions do not allow for a direct scaling of the geometry of the mooring line footprint. This may be a consequence of a restriction in the depth of the mooring system or the width of the mooring system. In this event, a truncated mooring system should be employed (Chakrabarti, 2005). There are a few approaches to truncation that have been used, with varying levels of success. In (Molins et al., 2015), mooring system truncation was accomplished with some success by increasing the mass of the lower parts of the cable. In (Harnois et al., 2015), numerical models suggested that the section of the catenary system that rested on the seabed during large displacements did not significantly affect hydrodynamic behaviour and could be truncated.

The "SMART" system was suggested by (Chakrabarti, 2005). The SMART system consists of a line running from the model's fairlead position to ring gauges downward at the elevation angle to a specified suspended weight fastened to the line and then fixed to a vertical pole. The restoring force follows the desired stiffness of a non-linear mooring system by adjusting the four variables; A, B, C, and the magnitude of the suspended mass. The SMART system layout is shown below in Figure 17.

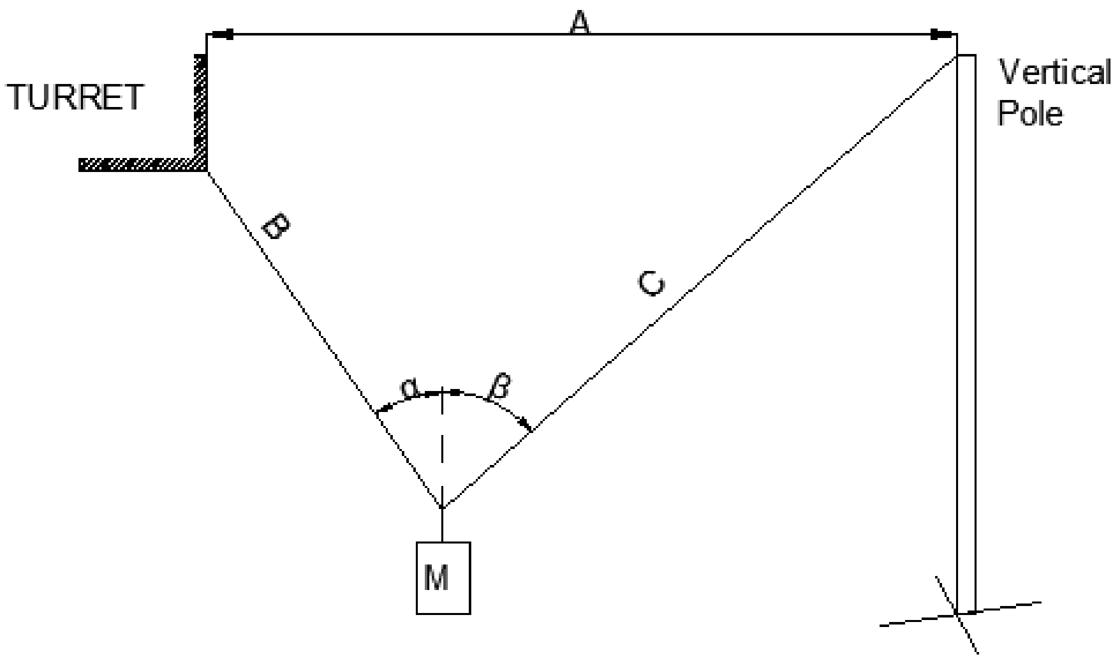

Figure 17 – SMART mooring line arrangement (Chakrabarti, 2005)

Truncation can also be achieved through the “taut line and spring” method, described in (Chester et al., 2018). This method involves using a series of springs, with their extensions limited at specific points to match the load-displacement curve of the catenary mooring system. When the extension of the spring is at a maximum, the load is then transferred to the other springs in the system, thus changing the effective spring constant of the system. Subsequent analysis indicated a good correlation between results from numerical models and results using the method. This method of mooring line truncation was used during the testing campaign.

2.4.3 Mooring requirements for wave tank testing.

Some of the challenges in correctly scaling the geometry of a mooring line footrpint have been mentioned above in section 2.4.2. Mooring systems have a significant influence on the motion of a floating offshore wind platform when it is subjected to wind and wave forces. Mooring line tension can influence the magnitude of device motions. Section 2.3 alluded to some of the main types of mooring systems used for floating platforms. These include catenary mooring systems, where the weight of a long length of chain running along the seabed is used to prevent platform motions. In a catenary system, the chain size can be selected based on a desire to keep the system's peak surge-sway offset under a certain value under operation conditions. This can limit the design constraints on the dynamic electrical umbilical (Allen et al., 2020). Taut and semi-taut mooring systems can also be used, here stability is achieved through the tension in the mooring line (Pegalajar-Jurado et al., 2018).

Chains are not the only material used for the FOW platform mooring lines. Wire ropes and synthetic fibre ropes are commonly used in lieu of or in combination with chains. Wire rope has advantages when compared with the use of chains. With a wire rope, the same breaking load and a higher elasticity can be achieved with a lower weight of material. However, the downside of wire rope is that it is generally more prone to damage and corrosion. Synthetic fibre rope has the benefit that the material is light weight and has a high elasticity. Typical materials that can be used are polyester and dyneema.

While emulating the footprint of these mooring systems can be challenging, another challenge is achieving the correct physical properties of the mooring line at model scale can also be challenging. Ultimately, it is not possible to achieve the correct physical properties of a mooring line at model-scale. For example, if the correct properties of mooring line bouyancy are to be achieved at model-scale, it may not then be possible to achieve the correct cable diameter or cable mass/ unit length. For this reason, a comprimise must often be made for what mooring line properties are deemed most important for the purposes of a particular experimental test campaign. In many cases, the most important property of a mooring system is the stiffness of the mooring lines.

Comprehensive analysis of mooring behaviour helps to better understand platform responses. Analysis of mooring lines should be conducted in both the frequency domain and the time-domain analysis. Frequency domain analysis involves comparing mooring line responses with the incoming wave conditions through the use of Response Amplitude Operators (RAO). This compares the wave power-spectral density (PSD) with the PSD of mooring response. This can be used to see how the mooring, and the platform, respond to wave motions at different frequencies (He & Wang, 2021). Analysis in the time domain is condcuted by comparing the time-series' of the mooring responses with model response in the various 6DoF. Time-domain analysis gives a aids in showing the model magnitude of device responses at each time-step during a wave-tank testing experiment (Rong et al., 2021).

Fatigue failure has become one of the critical failure modes of a mooring system (Xue et al., 2018). Thus, fatigue assesment of a mooring system is imperative during the design phase. Fatigue is a cumulative process made from an irregular load history (Homb, 2013). Two distinct approaches have evolved to predict fatigue. The S-N approach, using stress-life cumulatative damage models. This methodology considers the cumulatative fatigue damage where a failure occurs after a number of loading cycles N, at a particular stress range S. The other approach is the fracture mechanics approach, using fatigue growth models. This method examines the fracture behaviour of mechanical elements under dynamic loading. It is predicted that failures occur if dominant cracks have grown to a critical length where the remaining strength of the component is insufficient (Thies et al., 2014).

2.5 Uncertainty Analysis

2.5.1 Introduction

Uncertainty analysis is an important part of model test experiments. Incorporating uncertainty analysis into model tests makes it possible to assess the quality of experimental results. Aside from this, it also offers a perspective on improving testing procedures (ISO, 2008a). However, to date, uncertainty analysis is not generally incorporated into typical testing campaigns. The International Towing Tank Conference (ITTC) recently released guidelines on uncertainty analysis specific to a horizontal axis wind turbine(ITTC, 2017). These guidelines appear to be lacking in terms of the detail needed to carry out uncertainty analysis. Guidance can also be found in (ITTC, 2008); while this paper is mainly directed at uncertainty analysis of wave energy converters (WECs), some of the procedures can be passed over to floating offshore renewable energy (FORE) platforms. The ITTC guidelines, and those set out in (ISO, 2008a),(ISO, 2008b),(American Society of Mechanical Engineers, 2006) and (McCombes et al., 2010) give general advice. However, they are guidelines only; the industry lacks literature on a systemic approach for assessing experimental uncertainty for each platform. Such is the nature of testing in wave basins, specific guidance on a platform-by-platform level is required rather than general guidelines, as is currently the case. This lack of research is not unique to FORE platforms, as it is also the case for WECs. However, in recent years, more work has gone into uncertainty analysis on fixed oscillating water columns (OWCs) (Judge et al., 2021; Orphin, 2020; Orphin et al., 2017, 2018, 2021). Prior to the release of these studies, limited literature was available on the topic. Literature is particularly limited about uncertainty assessment for FOWTs. Most wave tank testing is completed without addressing experimental uncertainty or mentioning it without explanation (O'Donnell et al., 2017; Ward et al., 2020; Yang et al., 2019).

Uncertainty analysis is avoided because it is time-consuming. Wave tank testing campaigns have limited time frames within which tests can be run. As a result, tests to assess model responses in various wave conditions are prioritised over uncertainty tests. This ideology ignores the fact that the accuracy of these results cannot be quantified fully without an uncertainty analysis. As will be outlined later in this section, multiple test repetitions are required to get enough samples to carry out meaningful analysis. This adds time and cost to the testing campaign. However, in recent years, an increased emphasis has been placed upon uncertainty analysis, like in (A. N. Robertson, 2017) where uncertainty helped validate an inter-comparison between a numerical model and physical model tests. In (Desmond et al., 2019), a metric was created for calculating the uncertainty across an entire time series to examine the impact on experimental uncertainty of introducing aerodynamic and rotor gyroscopic loading on a model multirotor floating wind energy platform during physical testing. In (Qiu et al., 2014), the potential sources of uncertainty in the testing of offshore structures is discussed. These papers highlight the value that can be gained by carrying out uncertainty analysis and promote it as something that should be standard practice going forward. The inclusion of uncertainty analysis is slowly becoming a more common practice. However, as made evident by the lack of available literature on the topic, there is still a considerable amount of work to be done.

2.5.2 Uncertainty Classification

Before discussing the different types of uncertainty, it is vital to distinguish between accuracy (often referred to as bias) and precision. Together, the two are taken as measures of uncertainty. Accuracy and precision are often used interchangeably. Accuracy is the degree of veracity, while precision is the degree of reproducibility. In the case of wave tank testing, accuracy would be how close the results are at model scale are to the 'real value'. Precision refers to how repeatable the test results are. Figure 18 illustrates this graphically.

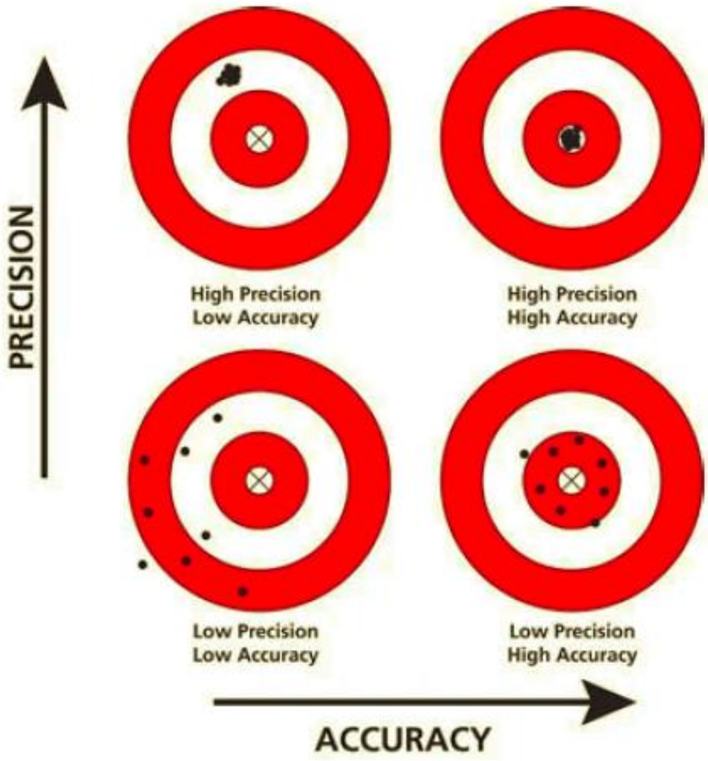

Figure 18- Accuracy vs Precision (Edvotek, 2021)

Accuracy and precision errors are also known as systematic and random errors. The American Society of Mechanical Engineers (American Society of Mechanical Engineers, 2006) uses this as a basis to classify different types of errors. The ISO (ISO, 2008a) uses another means of classification. Using the ISO method, uncertainties are classified into three separate categories: standard uncertainty (u_s), combined uncertainty (u_c), and expanded uncertainty (U).

Standard uncertainty can be grouped into two different types. Type A uncertainty and Type B uncertainty. In wave tank testing, Type A (u_A) uncertainty is found by applying statistical methods to multiple repeat measurements. The formula is shown below.

$$u_A = \frac{s}{\sqrt{n}}$$

Equation 37

where n is the number of repeat tests, and s is the standard deviation, which is given by,

$$s = \sqrt{\frac{\sum_{k=1}^{n}(q_k - \bar{q})^2}{n-1}},$$

Equation 38

In which q_k is the k^{th} observation and $\overline{q}$ is the mean.

Type B uncertainties are obtained based on a judgement from all relevant information available, such as:

- Previous test data.
- Testing experience/ Knowledge about the relevant materials.
- Manufacturer's specification/ platform manual.
- Data from calibrations.

The Type B uncertainty can be calculated for instrument calibration by applying a linear fit to end-end calibration data from whichever instruments have been calibrated throughout the testing process. The standard Type B uncertainty (u_B) is then given by the Standard Error of the Estimate(*SEE)*:

$$u_B = SEE = \sqrt{\frac{\Sigma\left(y_j - \hat{y}_j\right)^2}{M-2}}$$

Equation 39

where *M* is the number of calibration points, y_j is the data point and $\hat{y}_j$ is the fitted value.

It is not uncommon to have Type A and multiple Type B uncertainties for different parameters during wave tank testing (Judge et al., 2021; Orphin, 2020). This can be dealt with using the formula below.

$$u_s = \sqrt{u_A^2 + u_{B1}^2 + u_{B2}^2 + \cdots\ u_{Bn}^2}$$

Equation 40

Wave tank testing presents many sources of uncertainty, both type A and type B. Each of these individual sources of uncertainty contributes to the overall uncertainty of a given value. In wave tank testing, individual readings are taken for values such as wave height and wave period, and then these values are combined to calculate the uncertainty for the desired output. The processes by which these individual uncertainties are combined will be discussed in more detail in Section 2.5.4. Once the combined uncertainty (u_c) has been calculated, the expanded uncertainty (U) can be calculated using the formula below.

$$U = ku_c$$

Equation 41

where *k* is a coverage factor. The coverage factor, *k*, includes an interval about the result of a measurement, *y*, that may be expected to encompass a large percentage of the distribution of values that could reasonably be attributed to a particular measurand. In other words, the coverage factor, *k*, should be chosen to provide an interval $Y = y \pm U$ (ITTC, 2008) corresponding to a particular level of confidence. Thus, for a lower level of confidence, the coverage factor will lower, resulting in a smaller interval. The coverage factor will be higher for a higher level of confidence, resulting in a larger interval. ITTC recommends that that results be reported with a 95% confidence interval. A more straightforward approach is suggested in (ISO, 2008b), where the distribution of values can be assumed as normal (also known as Gaussian) distribution. If the number of degrees of freedom is significant (V >30), where $V = n - 1$, *k* may be assumed as 2. For a smaller number of samples, it is suggested that a Student-t distribution (Student, 1908) Table, shown below in Figure 19, is used to find a value for *k* at the 95% confidence interval.

t Table

cum. prob	$t_{.50}$	$t_{.75}$	$t_{.80}$	$t_{.85}$	$t_{.90}$	$t_{.95}$	$t_{.975}$	$t_{.99}$	$t_{.995}$	$t_{.999}$	$t_{.9995}$
one-tail	**0.50**	**0.25**	**0.20**	**0.15**	**0.10**	**0.05**	**0.025**	**0.01**	**0.005**	**0.001**	**0.0005**
two-tails	**1.00**	**0.50**	**0.40**	**0.30**	**0.20**	**0.10**	**0.05**	**0.02**	**0.01**	**0.002**	**0.001**
df											
1	0.000	1.000	1.376	1.963	3.078	6.314	12.71	31.82	63.66	318.31	636.62
2	0.000	0.816	1.061	1.386	1.886	2.920	4.303	6.965	9.925	22.327	31.599
3	0.000	0.765	0.978	1.250	1.638	2.353	3.182	4.541	5.841	10.215	12.924
4	0.000	0.741	0.941	1.190	1.533	2.132	2.776	3.747	4.604	7.173	8.610
5	0.000	0.727	0.920	1.156	1.476	2.015	2.571	3.365	4.032	5.893	6.869
6	0.000	0.718	0.906	1.134	1.440	1.943	2.447	3.143	3.707	5.208	5.959
7	0.000	0.711	0.896	1.119	1.415	1.895	2.365	2.998	3.499	4.785	5.408
8	0.000	0.706	0.889	1.108	1.397	1.860	2.306	2.896	3.355	4.501	5.041
9	0.000	0.703	0.883	1.100	1.383	1.833	2.262	2.821	3.250	4.297	4.781
10	0.000	0.700	0.879	1.093	1.372	1.812	2.228	2.764	3.169	4.144	4.587
11	0.000	0.697	0.876	1.088	1.363	1.796	2.201	2.718	3.106	4.025	4.437
12	0.000	0.695	0.873	1.083	1.356	1.782	2.179	2.681	3.055	3.930	4.318
13	0.000	0.694	0.870	1.079	1.350	1.771	2.160	2.650	3.012	3.852	4.221
14	0.000	0.692	0.868	1.076	1.345	1.761	2.145	2.624	2.977	3.787	4.140
15	0.000	0.691	0.866	1.074	1.341	1.753	2.131	2.602	2.947	3.733	4.073
16	0.000	0.690	0.865	1.071	1.337	1.746	2.120	2.583	2.921	3.686	4.015
17	0.000	0.689	0.863	1.069	1.333	1.740	2.110	2.567	2.898	3.646	3.965
18	0.000	0.688	0.862	1.067	1.330	1.734	2.101	2.552	2.878	3.610	3.922
19	0.000	0.688	0.861	1.066	1.328	1.729	2.093	2.539	2.861	3.579	3.883
20	0.000	0.687	0.860	1.064	1.325	1.725	2.086	2.528	2.845	3.552	3.850
21	0.000	0.686	0.859	1.063	1.323	1.721	2.080	2.518	2.831	3.527	3.819
22	0.000	0.686	0.858	1.061	1.321	1.717	2.074	2.508	2.819	3.505	3.792
23	0.000	0.685	0.858	1.060	1.319	1.714	2.069	2.500	2.807	3.485	3.768
24	0.000	0.685	0.857	1.059	1.318	1.711	2.064	2.492	2.797	3.467	3.745
25	0.000	0.684	0.856	1.058	1.316	1.708	2.060	2.485	2.787	3.450	3.725
26	0.000	0.684	0.856	1.058	1.315	1.706	2.056	2.479	2.779	3.435	3.707
27	0.000	0.684	0.855	1.057	1.314	1.703	2.052	2.473	2.771	3.421	3.690
28	0.000	0.683	0.855	1.056	1.313	1.701	2.048	2.467	2.763	3.408	3.674
29	0.000	0.683	0.854	1.055	1.311	1.699	2.045	2.462	2.756	3.396	3.659
30	0.000	0.683	0.854	1.055	1.310	1.697	2.042	2.457	2.750	3.385	3.646
40	0.000	0.681	0.851	1.050	1.303	1.684	2.021	2.423	2.704	3.307	3.551
60	0.000	0.679	0.848	1.045	1.296	1.671	2.000	2.390	2.660	3.232	3.460
80	0.000	0.678	0.846	1.043	1.292	1.664	1.990	2.374	2.639	3.195	3.416
100	0.000	0.677	0.845	1.042	1.290	1.660	1.984	2.364	2.626	3.174	3.390
1000	0.000	0.675	0.842	1.037	1.282	1.646	1.962	2.330	2.581	3.098	3.300
z	0.000	0.674	0.842	1.036	1.282	1.645	1.960	2.326	2.576	3.090	3.291
	0%	50%	60%	70%	80%	90%	95%	98%	99%	99.8%	99.9%
	Confidence Level										

Figure 19 - Student-t distribution table (Tdistributiontable, 2020)

2.5.3 Sources of experimental uncertainty in wave tank testing

Wave tank testing is a complex mesh of activity where many different systems are in operation at any one time; for this reason, experimental uncertainties are common during wave tank testing. Sources of uncertainty are likely to be found during wave tank setup, throughout the testing process, and during data analysis.

Laboratory effects are a definite source of uncertainty in wave tank testing. Each wave tank will be different from another wave tank in some way or another. Ocean waves are extremely sensitive to the bathymetry of the area in which they are being propagated (Boccia et al., 2015). Likewise, waves propagated in a wave tank are extremely sensitive to the shape and design of a wave tank. The depth and dimensions of a wave tank have a huge bearing on the waves produced within the wave tank. Every wave tank has different means to deal with reflections in the tank; certain facilities, like the FloWave facility at the University of Edinburgh, are surrounded by paddles (FloWave, 2022). Force feedback paddles adjust their motion to mitigate against the effect of wave reflection and produce a wave that is as close as possible to the inputted wave parameters. Many other tanks will have force feedback paddles only on one side of the wave tank. In such a case, a beach is employed at the other end to reduce reflections. The efficacy of the beach at reducing reflections depends on its porosity, slope, roughness, and depth (EurOtop, 2018). The degree to which reflections are reduced in the wave tank will dictate the uncertainty caused by reflection in the tank. The type of wavemaker used in the tank is also a source of uncertainty. Certain wavemaker designs and systems can produce more accurate and precise waves than others. The ability of a tank to reproduce the inputted wave parameters as accurately as possible will have a significant bearing on the uncertainty in the wave measurement. (Orphin, 2020) tested in two extremely different facilities in the Australian Maritime College Model Test Basin and the Queen's University Belfast Portaferry Coastal Wave Basin with stark differences between the results.

Wave tank testing is not yet an automated process. Therefore, humans are very much involved throughout the whole process, which causes measurement uncertainties. Different methodologies in wave tank setup, wave calibration, and testing are likely due to varying levels of experience of those conducting testing (Qiu et al., 2014). In addition, analysis is conducted differently by different people. As part of the MaRINET2 project, a study was recently concluded to quantify the degree to which carrying out the same experiment with the same test plan in different facilities affects the results obtained (Davey et al., 2021; Gueydon, Judge, O'shea, et al., 2021; Ohana et al., 2021). The studies found that not only did different wave conditions in each basin cause discrepancies in results, but different methodologies for both testing and analysis had a significant influence also (MaRINET2, 2021a).

Uncertainties are likely to arise unless the model setup is carried out meticulously; even in such a scenario, some uncertainties will not be mitigated. Where mooring lines are used, the position of the mooring lines on the model, along with the anchoring position, can have a considerable bearing on uncertainty. Springs must be calibrated, and mooring lines must be cut to a length such that the platform sits in the correct position in the tank, usually the centre of the tank, such that waves can be targeted to the device location. If this is not done correctly, it is likely to cause uncertainties. Any wires or cables used to power part of the platform or extract data from the platform must be positioned so as not to affect the motion of the platform or obstruct the motion tracking system.

Instruments used during testing, such as wave gauges, motion tracker systems (Qualisys), pressure transducers, the wind emulation system, load cells, and the data acquisition system used, are significant sources of uncertainty. Uncertainties in measurement are caused by accuracy of the instrument, the least count error of the instrument (the number of decimal places to which data is given), instrument calibration, instrument position, noise in the readings, frequency of the readings, and drift on the instruments over time.

One of the more challenging aspects of wave tank testing is to create a model from full-scale specifications. All of the measured quantities of the model platform must be scaled down correctly from full-scale. In most cases, due to factors like material limitations, it can be challenging to correctly scale down the platform dimensions while also correctly scaling the weight and moments of inertia of the platform. The dimensions of the platform must be scaled correctly, and consequently, it is usually the case that the weight of the scaled platform is affected by this. This is resolved by adding ballast to the platform in a specific location, thus correcting the weight and inertia issues. While this is done to the highest degree of accuracy possible, uncertainties cannot be avoided. The dimensions of the manufactured model are likely to deviate slightly from the specifications provided to the manufacturer (A. N. Robertson et al., 2018). The use of welding to join sections together is likely to alter the wetted area of the platform.

Water temperature is likely to fluctuate slightly throughout the testing campaign. The water density, viscosity, surface tension and buoyancy will change as the water temperature changes. From an analysis perspective, it would not be feasible to account for a constantly fluctuating water temperature test by test. Consequently, the water temperature is assumed constant at a particular value, leading to minor uncertainties.

Many of the sources of uncertainty mentioned above do not contribute significantly to the overall uncertainty in any given test. This is not to suggest that they should not be accounted for when conducting an uncertainty analysis. In many cases, if these uncertainties were eliminated, the overall uncertainty would not reduce significantly. (A. N. Robertson et al., 2018) and (A. Robertson et al., 2020) investigated the most significant sources of uncertainty in model testing of FOWTs. The studies determined that the main contributors to model uncertainty were the mooring stiffness, the vertical CoG and inertia about the y-axis for pitch response, the wave amplitude, and the platform draft.

2.5.4 Combined Uncertainty (u_c)

The combined uncertainty (u_c) gives the uncertainty for a particular output due to multiple uncertainties for different variables. In other words, the combined uncertainty is an estimated value for the standard deviation of a result (Taylor & Kuyatt, 1994). There are a few different methods used to calculate uncertainty. The Taylor-Series Method (TSM), also known as the GUM (Guide to the expression of uncertainty in measurement) and the Monte Carlo method (MCM) (ISO, 2008b, 2008a), are the two primary methods used to calculate the combined uncertainty. The ASME (American Society of Mechanical Engineers) method is also widely used, and it is very similar to the TSM; however, a different notation is used, as was explained in Section 2.3.2. Thus, for simplicity, only the ISO methods will be dealt with in detail in this section.

As has already been mentioned, in many cases, a measurand Y is not measured directly but is obtained from N other quantities $X_1, X_2, X_3, \ldots, X_N$ through a functional relationship f:

$$Y = f\,(X_1, X_2, X_3, \ldots, X_N)$$

Equation 42

An estimate of the output quantity y is obtained by using input estimates $x_1, x_2, x_3, \ldots, x_N$ for N input quantities $X_1, X_2, X_3, \ldots, X_N$. Thus, the result of the measurement or the output estimate y is given by;

$$y = f(x_1, x_2, x_3, \ldots, x_N)$$

Equation 43

$u_c(y)$ denotes the combined standard uncertainty of the measurement result and represents the standard deviation of the measurand result y.

In the case of the Taylor Series Method, y is obtained using Equation 44 shown below:

$$u_c^2 = \sum_{i=1}^{N} \left(\frac{\partial f}{\partial x_i}\right)^2 u^2(x_i) + 2\sum_{i=1}^{N-1} \sum_{j=i+1}^{N} \frac{\partial f}{\partial x_i}\frac{\partial f}{\partial x_j} u(x_i, x_j)$$

Equation 44

The partial derivatives are also known as sensitivity coefficients. The term $u(x_i,x_j)$ is the estimated covariance, and $u(x_i)$ is the estimated uncertainty. The use of partial derivatives can often be challenging to deal with, and so alternative methodologies can be used to avoid this problem.

The Monte Carlo Method (MCM), as described in (ISO, 2008b), is a method that has been explored in the context of wave tank testing in multiple papers over the past number of years (Judge et al., 2021; Orphin, 2020; Orphin et al., 2018) where it was used to calculate the uncertainty of an Oscillating Water Column (OWC). The MCM has also been used to evaluate uncertainty in many industries ranging from medical practices (Koerkamp et al., 2011) to geotechnical engineering (Ching, 2011). Value is found in the MCM when the probability distribution function (PDF) of Y is nonlinear and when linearisation of the model does not provide adequate representation, e.g., due to asymmetry. Furthermore, unlike the TSM, the MCM does not contain approximations or errors because it propagates uncertainty through measurand functions. Finally, the MCM is said to be easier to implement (Orphin, 2020).

The MCM involves running N independent iterations of a particular model relevant to the experiment. Each iteration involves random sampling of value from a probability distribution that characterises each stochastic variable. A stochastic variable depends on the outcomes of random phenomena. There are numerous different probability distributions used in statistical applications: uniform distribution, Bernoulli distribution, Poisson distribution, and Gaussian distribution. The standard uncertainties, calculated as per Section 2.3.2, are then assumed to represent the standard deviations of a Gaussian probability distribution function. Each Monte Carlo iteration takes a random sample of the probability distribution function of each quantity to calculate the result. The standard deviation of the *N* Monte Carlo iterations is taken to be $u_c(y)$, the uncertainty associated with the result.

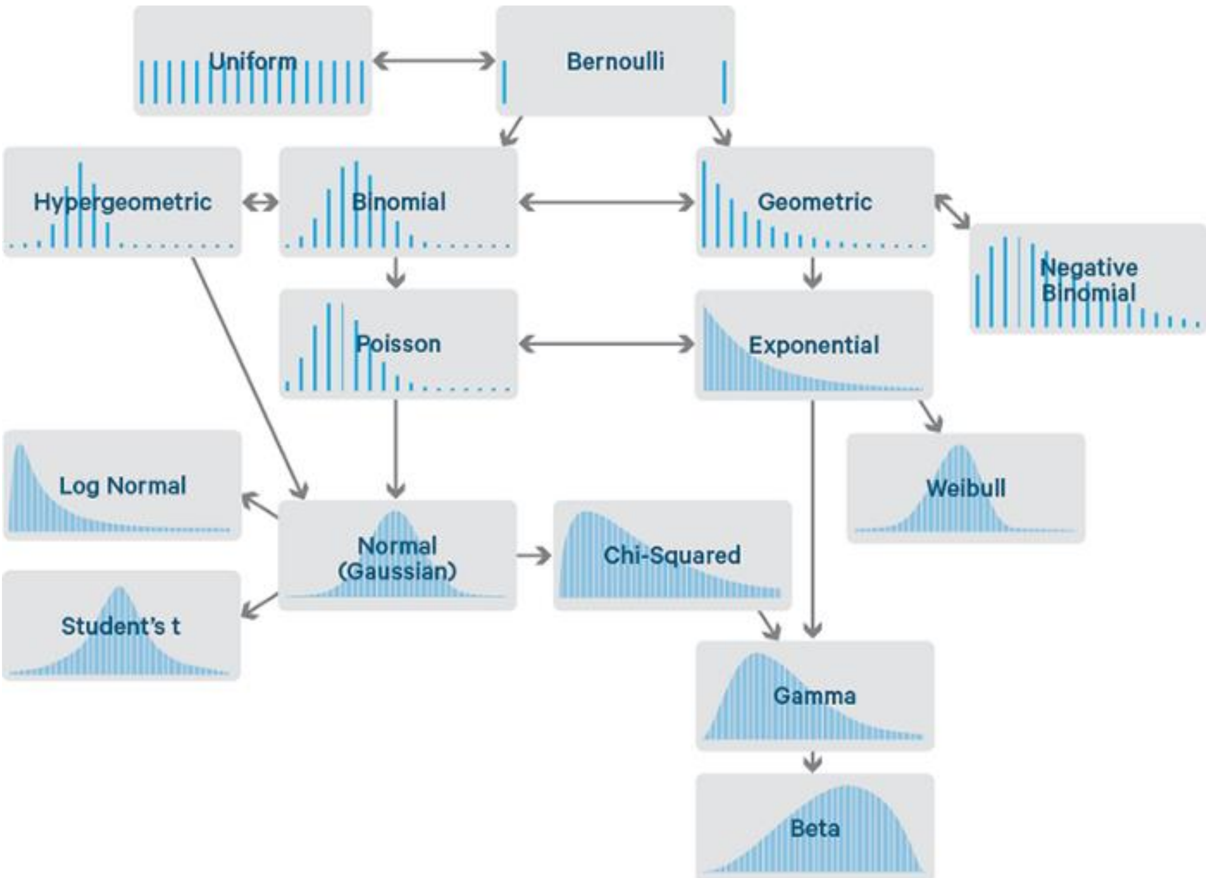

Figure 20 - A sample of different probability distributions (Menon, 2020)

2.5.5 Uncertainty Analysis of Irregular waves

Analysis of regular waves and their associated uncertainties is straightforward. For regular waves, the outputs from analyses come in the form of single value metrics. The response amplitude operator is typically used to characterise the response of a floating structure to the incident waves magnitudes (O'Donnell et al., 2021). The response amplitude operator for a regular wave is simply the ratio of the linear response amplitude to the ratio linear wave amplitude. Single metrics generated during regular wave analysis allow for uncertainties to be propagated using the MCM or TSM and allow for a simple comparison between testing carried out under different conditions. However, regular waves do not occur in a real wave environment and do not allow for a detailed assessment of the platform motions across a range of frequencies unless regular waves with a wide range of frequencies are tested; this can be time-consuming, and it is hard to know how small the frequency gap should be between each regular wave test. For this reason, regular waves are mainly used for numerical model validation purposes, to observe and monitor platform response to regular excitation forces that define the basic operation of the platform and to evaluate higher-order effects by

comparing linear and finite waves (Holmes, 2009). Hence, irregular waves and broad-spectrum waves are used more often. Comparison between different tests for irregular waves is more difficult. For irregular waves, a curve is generated to represent the platform's response across a range of frequencies. While this is extremely useful in understanding platform motions, it can present challenges when conducting an uncertainty analysis and comparing results from different sources. Uncertainty analysis for broad-spectrum waves is more challenging and time-consuming than regular waves. Where regular waves tend to have a run-time of below 180s at model-scale, irregular waves tend to run for between 20 and 40 minutes at model scale, depending on the scale of the model tested.

For this reason, single value metrics are desirable for irregular waves to allow for uncertainty analysis and comparisons between test results. The use of metrics for uncertainty analysis is not limited to the offshore renewable sector (Crosetto et al., 2000). Uncertainty analysis in the floating offshore wind sector has not been studied in much detail. Consequently, not many metrics have been developed for uncertainty analysis. However, recent progress in the development of procedures for uncertainty analysis for irregular sea-states has resulted in the development of metrics.

(A. N. Robertson et al., 2018) and subsequent papers were pioneering in their research into uncertainty analysis for FOWTs. In the initial 2018 paper, various metrics were used to quantify uncertainty. The low-frequency response level integral of the power spectral density (PSD) was calculated over a defined low-frequency range. Robertson also calculated the mean drift offset for comparison purposes; this metric was also used in (Paduano et al., 2020). The other two metrics used in the paper were the values of the RAOs at six discrete frequency points and the ten highest response maxima for surge, heave, pitch, and mooring tension. In (Desmond et al., 2019), a similar metric was developed for the calculation of uncertainty in irregular waves. (Desmond et al., 2019) critiqued the use of the ten highest response maxima, saying that examining the top 10 peaks does not give an appreciation for error across the whole time series. They found that the magnitude of the error range found with this method was not well correlated to the error measured across the whole time series. When considering the whole time series, 8 out of the top ten peak error ranges were exceeded for 85% of the time series. (Desmond et al., 2019) developed the P^5 metric; this is the error range which is exceeded 5% of the time for concurrent time series with five repetitions.

In (A. Robertson et al., 2020), the metric critiqued in (Desmond et al., 2019) no longer used. A new metric not used in the 2018 paper was added: the PSD sum in the wave frequency range. This is the integral of the PSD of surge, heave, and pitch motions over the wave-frequency range. The frequency limits for the low-frequency range and wave frequency range vary depending on the wave conditions. Other researchers have since sought to expand on the development of metrics, started in those papers (Gueydon, Judge, Lyden, et al., 2021). In (Gueydon, Judge, Lyden, et al., 2021), there was a focus on developing two metrics, one to examine the response of the platform in the wave frequency range and one to examine the location of the resonance peak of the platform.

The metric used to examine the response of the system in the wave frequency range, $M_{WF,}$ is calculated from

$$M_{WF} = \sqrt{\frac{\int_{f_1}^{f_2} S_{signal} df}{m_o}}$$

Equation 45 (Gueydon, Judge, Lyden, et al., 2021)

where f_2 and f_1 are the maximum and minimum frequency bounds for the wave frequency range, S_{signal} is the PSD of the signal, and m_o is the zeroth spectral moment.

$$m_0 = \int_{f1}^{f2} S_\eta df$$

Equation 46

The metric is designed for analysis of JONSWAP wave spectra, and its efficacy for analysis of other types of wave spectra is yet to be investigated. The other metric derived in (Gueydon, Judge, Lyden, et al., 2021), T_r, represents the period of resonance response and is given by:

$$T_r = \frac{\int_{f_e-\delta f}^{f_e+\delta f} S_{signal}^4 \, df}{\int_{f_e-\delta f}^{f_e+\delta f} f . S_{signal}^4 \, df}$$

Equation 47 (Gueydon, Judge, Lyden, et al., 2021)

where S_{signal} is the PSD of the signal, f_e is the eigen frequency, Δf is the frequency band around f_e that covers the peak shaped resonance response of the signal. Much like with M_{WF}, the efficacy of T_r for analysis beyond JONSWAP wave-spectra remains to be seen.

The use of the metrics such as M_{WF} and T_r allows for a more accurate comparison between data sets from different sources and uncertainty analysis to be completed.

2.6 Summary

This section emphasises the key role that wave tank testing plays in developing offshore renewable energy platforms. However, while wave tank testing is highly beneficial, uncertainties are likely to arise during the testing campaign.

In recent years there has been an increased research interest on the topic of uncertainty in wave tank testing of FOWTs. In (A. N. Robertson et al., 2018), some of the most significant contributors to uncertainty in wave tank tests of FOWTs were identified. Factors such as model inertia and CoG, mooring stiffness and wind emulation system are significant contributors to uncertainty during wave tank testing campaigns. There has been no study into the effect that these uncertainties could have on platform responses. Through an extensive wave tank testing campaign, this study aims to quantify the effect that these most prominent sources of uncertainty will have on platform motions using metrics. New metrics, which have been developed following on from Robertsons' 2018 study, will be used to complete this comparison. This study aims to use two very different floating wind concepts to assess the influence of these uncertainties and to determine whether model design has a bearing on the affect of these uncertainties.

3 Experimental Test Campaign

3.1 Introduction

This section presents the experimental test campaign conducted at the Lir National Ocean Test Facility in UCC. Two models were used for this testing campaign, and they will be hereby referred to as model A and model B. The details of model A will be presented below; however, the details of model B are highly confidential and thus, will not be presented. Model A and Model B are two completely different floating offshore wind platform concepts. These two models were chosen for this study to try and help understand the extent to which uncertainties influence test results and whether the influence of uncertainties is consistent for different model designs.

The approach taken to scale, design and fabricate the models used during testing is described. The tests used to measure the physical characteristics of the built model are then presented. The models are described, and the test facility, tank layout, and instrumentation are presented. Finally, the rationale behind the testing plan is explained in detail.

3.2 Model Descriptions

3.2.1 Model A

Model A, a 1/60 scale semisubmersible floating wind platform, was constructed solely for the purpose of the MaRINET2 wind round-robin testing campaign (MaRINET2, 2021b). The scale model represents a conceptual platform capable of holding a 10MW wind turbine. The floating structure consists of three vertical circular columns linked by three horizontal pontoons with a rectangular cross-section, the dimensions of which are shown below in Figure 21. The model is made mainly with aluminium; its mass, inertias, and CoG are controlled by lead ballast placed at specific locations within the model and by the inertia of the wind emulation system deployed at the top of the tower. The mass of Model A was measured using a standard weighing scale. The scale used had a maximum allowable mass of 150kg and was accurate to 0.01kg at the model scale. The draft of the model was measured once the platform was floating in the tank with the moorings attached. The model mass and draft are shown in Table 3 below.

	Model Scale	Full Scale
Model Mass	117.75kg	25,434tn
Draft	0.425m	25.5m

Table 3 – Table for Mass and Draft of Model A at Model scale and full-scale.

In this thesis, all model properties for model A will be reported at full-scale from here onwards. Estimation of initial model properties involved completing balance and hang tests and bifilar and trifilar tests, described below in Section 3.4. The position of the CoG of the model will be given with reference to known points along the body.

- The location of the x-axis is given with reference to the bow of the model.
- The location of the y-axis is given with reference to the centreline (line from tower to centre of the bow) of the model.
- The location of the z-axis is given with reference to the keel of the model.

CoG Position			
	x-axis	y-axis	z-axis
Distance from reference point	Bow	Centreline	Keel
Actual Reading(m)	26.58	0	13.2

Table 4- Initial Location of CoG of Model A

	I_{xx}	I_{yy}	I_{zz}
Inertia(tn.m^2)	31669819.8	34404167.1	20283328.1
Radius of gyration (m)	35.2870589	36.7788538	28.2398428

Table 5 - Initial Inertia Properties of Model.

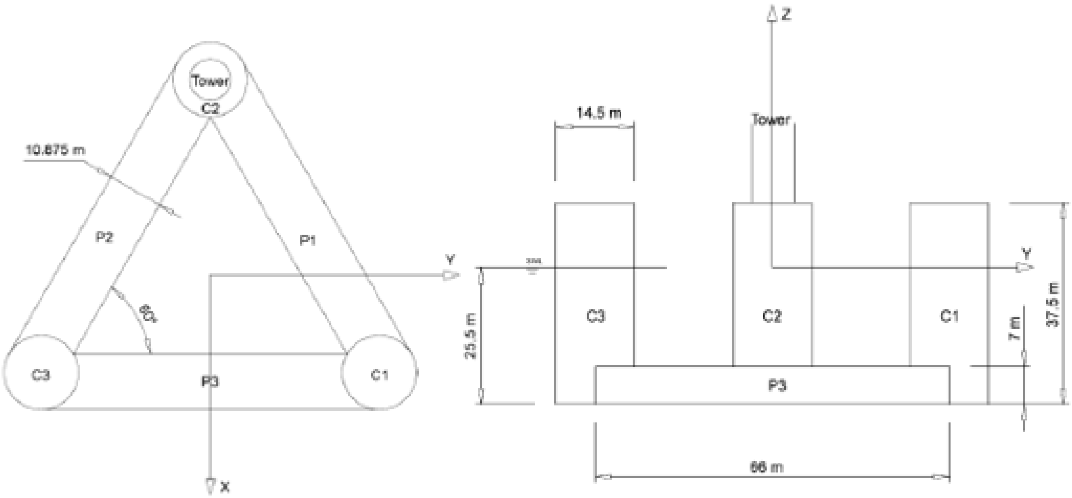

Figure 21 – Plan and elevation view of Model A with full-scale dimensions (MaRINET2, 2019)

Figure 22 – Model in the tank during testing.

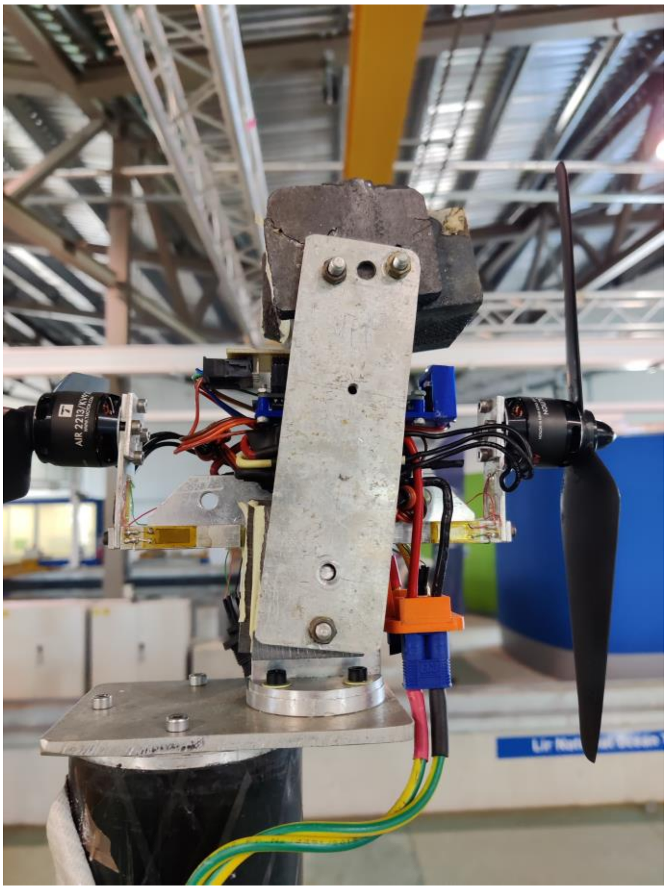

Figure 23- Ifremer Thruster used on Model A

Model A was initially set up in the tank as described in Section 3.7.1 in a water depth of 3m, 180m at full-scale. The “Ifremer thruster” was placed on top of the tower at the stern of the model. 2.98kg of lead was also placed on top of the tower to correct the inertia of the body. The thruster was calibrated and programmed to achieve fixed values of thrust (3, 5, 7 and 8N at model scale). The force delivered by the thruster is perpendicular to the wind turbine rotor plane and is applied at the wind turbine hub location. Given that only the thrust is emulated, the thrust generated can be scaled using Froude’s Law. In actual wind turbines, forces and moments would act in three directions at the hub location rather than just one under the influence of thrust only. However, for the reasons stated in 2.4.2, the thrust is the most important load in terms of wave tank testing.

Power was sent to the thruster using the power cable shown in Figure 22. The power cable was connected to the thruster at the top of the tower, as shown in Figure 23. It was then brought down through the tower and exited at the bottom of the tower. The power cable itself was quite stiff and rigid, which influenced the platform motions. In this study, the influence of the power cable was beyond the scope of this study; nonetheless, measures were used to reduce the impact of the cable. This was done by attaching the cable to a point above the water utilising a soft spring to reduce the influence of the cable bouncing. The cable was set up in the same way for each variation for consistency.

A Wi-Fi signal is emitted from an Arduino board attached to the thruster, which allows the thruster to be controlled remotely from a desktop. The thrust emitted from the thruster was not recorded. It was assumed that a constant thrust was present throughout.

The "MaRINET2" horizontal mooring system was used for the initial setup. This consisted of a stiff mooring line placed in series with a load cell and two springs in series. Ifremer provided the mooring lines for the MaRINET2 study. The exact same setup that was used for the MaRINET2 study, as described in (Gueydon, Judge, O’shea, et al., 2021)

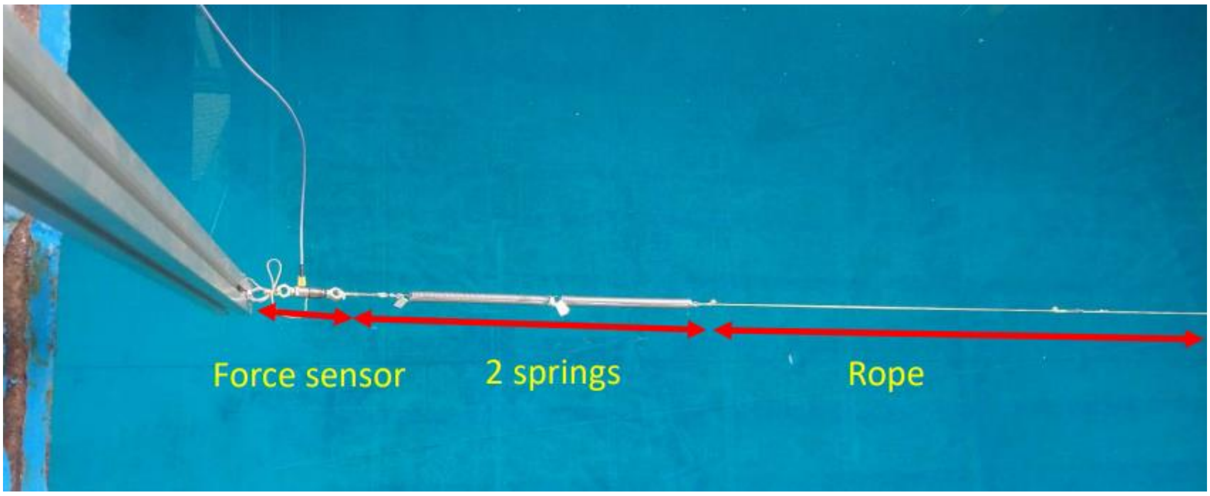

Figure 24 – Mooring system setup.

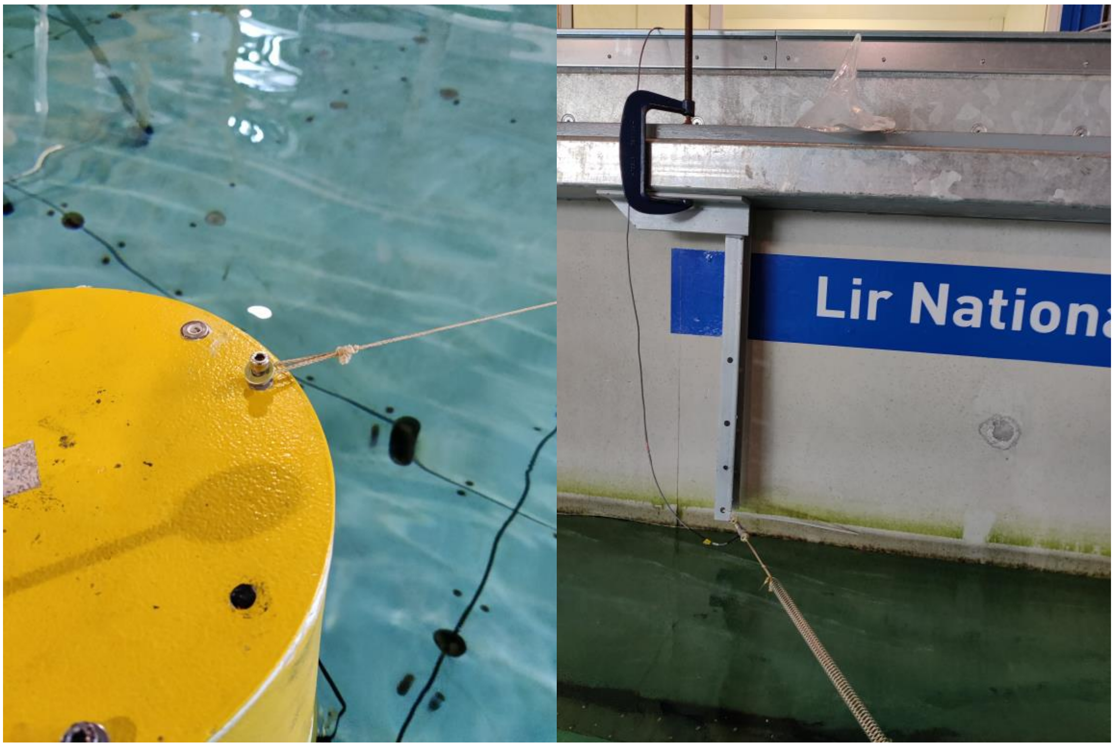

Figure 25 – Mooring line fairleads and attachments to tank wall for model A.

The mooring was attached to a fixed point on either the side of the tank, as shown in Figure 25, or to the footbridge at the locations shown in Section 3.7.1 below. The fairlead points were a screw that had been screwed into the top of the circular columns, as shown in Figure 25. Each mooring line consisted of a stiff, lightweight dyneema rope, two springs in series and a load cell attached at the end of the line attached to a fixed point. The dyneema rope was assumed to be inextensible under the loads present during this study. Thus, the stiffness of the mooring lines came from the springs only. The two springs in series were calibrated together, and they were assumed to behave as one spring. The value presented in Table 6 below represents the stiffness of the two springs in series.

	Tower	Port	Starboard
Spring stiffness (kN/m)	45.79639	45.76921	45.48099393

Table 6 – Stiffness of Mooring lines for initial mooring setup.

3.2.2 Model B

The full details of Model B are not presented in detail at any point throughout this thesis, as it is a novel, commercially sensitive, floating wind platform concept. The model was scaled and tested to assess the platform performance in various wave conditions and validate a numerical model developed by the parent company. The model is a hybrid design between two conventional FOWT concepts currently on the market. A catenary mooring system held the model in place in the tank. The model was equipped with the SiL wind emulation system. The SIL methodology calculates the correct wind turbine thrust and rotor moments based on real-time and full-scale simulations in Fatigue, Aerodynamics, Structures and Turbulence T (FAST), considering the measured platform motion during the experiments. The obtained force and moments were correctly reduced through Froude scaling and introduced in the platform model through a set of 6 propellers. The six-rotor blades turn so that both torque and thrust are simulated.

3.3 Model Design and Fabrication

Designing a scaled model with the same physical parameters as the full-scale design can present various challenges, some of which have been highlighted in Section 2.4.2. In the present research, the models were designed using Solidworks software. A key focus of this research was to ensure that the dimensions and volumes occupied by the model were as accurate as possible for the reduced-scale model.

The materials chosen for fabrication and the thicknesses of these materials were chosen based on the availability of materials within the necessary timeframe. The materials chosen must give the model the required strength while not contributing excessively to the overall weight of the model. This is usually done as an iterative process, where the availability of material is established from suppliers while also using tools such as Solidworks to assess the suitability of the material for the requirements of the project.

Mitigation measures must be implemented should the model not be built exactly as per specifications. The likelihood of a model being built to the exact specifications given to the manufacturer is extremely low, often through no fault of the manufacturer. Assumptions about the densities of the materials used or about the volume of the welds tend to be difficult to estimate correctly. Depending on the mass of the ballast used, if the position of the ballast within the model is not placed in the correct location to the nearest millimetre, it can affect the model inertia and CoG significantly. In this research, access points to the ballast within the model were included in the model design so that, if necessary, lead ballast could be carefully positioned internally to give the correct values for inertia and centre of gravity (CoG).

However, in some instances, the inertia and CoG of the model cannot be rectified to the extent necessary, regardless of any mitigation measures taken. Table 7 below shows the difference between the desired and actual parameters for model A.

	Desired	Actual	% difference
Mass (tn)	25530	25434	-0.38
Distance between Centre of Gravity z and keel of device	12.04	13.2	9.63
Radius of gyration x (m)	32.43	35.29	8.8
Radius of gyration y (m)	32.42	36.78	13.45
Radius of gyration z (m)	30.49	28.24	-7.38

Table 7 – Difference between desired and actual properties for model A.

3.4 In-air tests

3.4.1 Balance tests and hang tests to determine the location of the CoG

The determination of the location of the centre of gravity of any model is integral before any model tests can take place. Section 3.3 highlighted some of the challenges faced when building a scaled model. The likelihood of a model being built exactly as per specifications is low. For this reason, all model parameters, including the CoG of the model, must be checked before testing.

Checking the CoG for the x and y-axes of most models is straightforward. This is done by balancing the model along with a stable, narrow, and straight bar, or angle section that is parallel to the x-axis of the model (see Figure 26). The line along which the bar runs, when the model is in stable equilibrium whilst balancing on the bar, is the line along which the x-axis CoG lies. This line is then marked on the model for reference. The same method is applied to find the location of the centre of gravity in the y-direction. The intersection between the two lines established for the x and y axes is the location of the CoG of the model in the horizontal plane.

Figure 26 Measuring the CoG using a long angle section, the 90° silver bar shown in both images

The centre of gravity in the z-direction can be found using the method shown in Figure 26. The method shown in Figure 26 was not suitable for model B due to the characteristics of the model. Thus, the CoG of model B was found by hanging the platform fully vertically, with the keel of the platform perpendicular to the ground. The CoG is located along the line of the strap with which the platform was hung. The intersection between all three lines can then be used to establish the exact location of the CoG of the model.

These methods of measuring the CoG of the model are quick and easy; however, there are some drawbacks to the method. The long angle section, shown in Figure 26, used to balance the model must be of suitable thickness so that stable equilibrium can be achieved. The CoG of model A lied in the open space in the centre of the model; consequently, a mark could not be drawn at the exact location to show precisely where the CoG was located. This meant that the points marked on either side of the model had to be used to find the CoG. The likelihood that the bar is perfectly parallel to the x or y-axes while the model is in equilibrium is low. This would result in an error in the location of the points marked on either side of the model to show where the axis lies.

3.4.2 Moment of Inertia Bifilar and Trifilar tests

The methods chosen at LIR to determine the moments of inertia about each axis of any given model are the bifilar (F. H. Newman & Searle, 1951) and trifilar (Schwartz et al., 1957) methods. Both are variations of the same method. The bifilar method suspends an object by two parallel chords, or filars, of equal length. The trifilar method uses three parallel filars of equal length. The chords must be connected at equal distances from the CoG. Depending on the model design or the axis about which the moment of inertia is to be determined, one method might be more appropriate than the other. Once the model is suspended by the filars, a force is applied to the model so that it rotates freely about the desired axis. The time taken for an oscillation about that axis is recorded. Errors are reduced by recording up to 50 oscillations of the suspended platform. This way, the influence of human errors starting and stopping the stopwatch is decreased significantly. The experiment is then repeated between 3 and 5 times for each axis.

The inertia of a model when conducting a bifilar test is found using the by filling into the following formula.

$$I = \frac{mgT^2d^2}{16\pi^2 l}$$

Equation 48 (F. H. Newman & Searle, 1951)

Where I is the inertia of the model about any given axis(kg m^2), m is the mass of the model (kg), g is the acceleration due to gravity (9.81m/s^2), d is the distance between the filars(m), T is the period of oscillation (s), and l is the length of the filars (m).

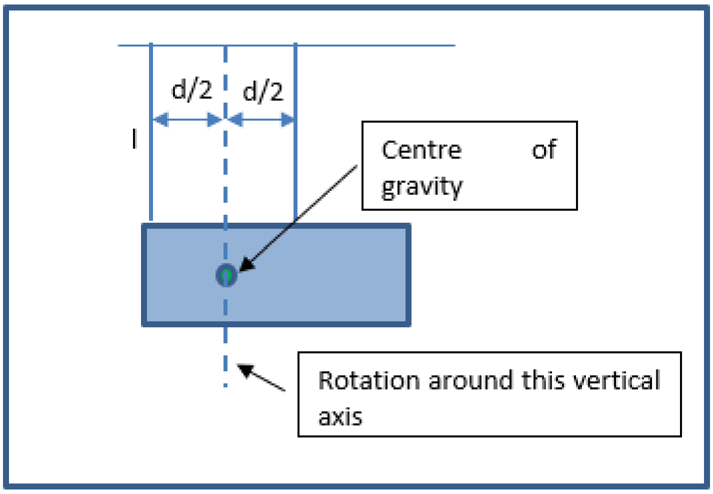

Figure 27- Labelling for bifilar method explained

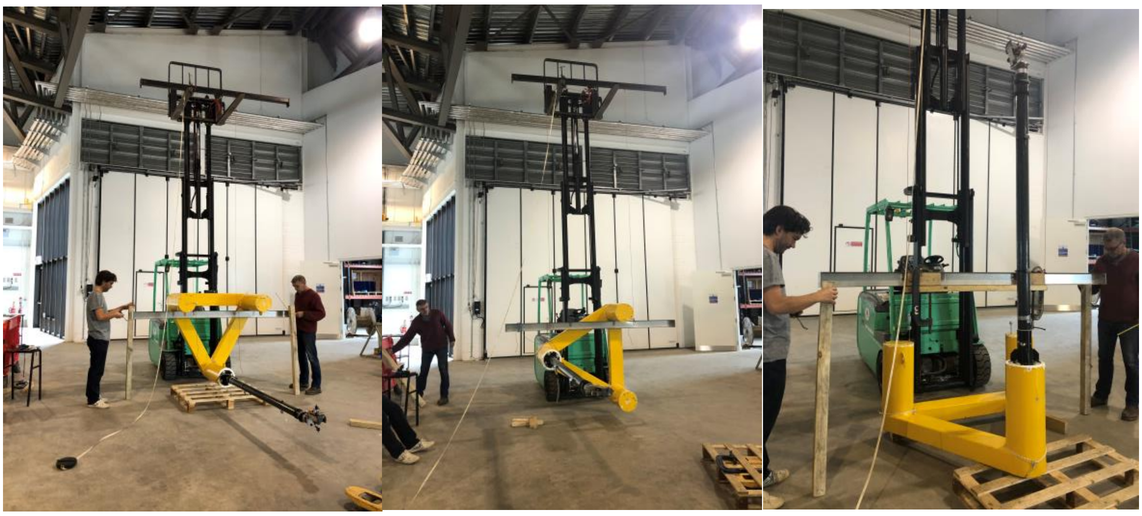

Figure 28 – Bifilar test for x, y, and z axes from left to right for model A.

A similar formula is used for the trifilar method

$$I = \frac{mgT^2d^2}{4\pi^2 l}$$

Equation 49 (Schwartz et al., 1957)

The same notation is used for both the trifilar and bifilar formulas.

Where the model is placed on an object like in Figure 28 or if a heavy material is used as the filars, the inertia of the platform and/or the filars must be established and then subtracted from the inertia found when carrying out the test on the model. This gives the value for the inertia of the model only.

The bifilar and trifilar methods are not without drawbacks; however, they are certainly the most straightforward and accurate methods of measuring the inertia of rigid bodies at a low cost (Hinrichsen, 2014). The uncertainty associated with the bifilar and trifilar methods was calculated by propagating the uncertainty associated with each input parameter through the MCM described above in Section 2.5.4. Each parameter had one or more sources of uncertainty associated with them. Where there is more than one source of uncertainty associated with a parameter, the formula shown in Equation 40 is used. Equation 40 is shown below again for clarity.

$$u_S = \sqrt{u_A^2 + u_{B1}^2 + u_{B2}^2 + \cdots u_{Bn}^2}$$

Equation 40

One thousand Monte Carlo simulations were used to calculate the uncertainty associated with the bifilar and trifilar methods. The uncertainty in the method used for each axis was calculated, and then an average uncertainty of the methods was found. The uncertainty in the inertia value measured for each axis was found by propagating the uncertainty for each input parameter using Equation 48 or Equation 49. The MCM estimated the uncertainty for each method. Uncertainties for the input parameters were found based on the accuracy of the instruments used to record the value, engineering knowledge, and the study of relevant literature on the topic. For example, uncertainty in the acceleration due to gravity, *g*, was 0.0057m/s^2 (ITTC, 2017). The error due to human response time for starting and stopping the stopwatch was approximately 0.25s (Jain et al., 2015). Other uncertainties included were the least count of the measurement tools used and errors due to parallax.

An average error of 3% was approximated as the error due to the bifilar and trifilar methods. Although (Gueydon, Judge, O'shea, et al., 2021) showed that the standard deviation of the values obtained for the inertia of the model by each of the different facilities during the MaRINET2 study was less than that, it was decided that a conservative approach should be taken when choosing an appropriate the variation in inertia.

3.5 Test Facility

Testing was completed at the LIR National Ocean Testing Facility, hereby referred to as LIR, in Ringaskiddy, Co. Cork. LIR is home to Irelands only infrastructure for small to medium scale laboratory testing of ocean and maritime systems. The facility is home to 4 different wave tanks at various scales and depths to emulate ocean waves and currents.

LIR's deep ocean basin (DOB), shown in Figure 29, was used to perform physical testing of both models. The dimensions of the DOB are as follows.

- Length: 35 m
- Width: 12 m
- Depth: 3 m

The basin is equipped with a moveable floor from 0m – 3m; this facilitates more efficient and accurate platform and instrumentation installation. The tank is equipped with 16 hinged, force feedback paddles, capable of producing waves up to 1.1m high and periods of up to 4s. An absorbing beach placed on the opposite side of the tank to the paddles. The absorbing beach, coupled with active paddle absorption from the force feedback paddles, limits the reflections within the tank, resulting in more realistic testing conditions. The basin is also equipped with a moveable instrumentation bridge, a footbridge, and an overhead crane. The paddles are controlled by the Edesign wave synthesis software. The paddles can produce a variety of different wave spectra. Depending on the spectrum chosen, several different wave parameters can be set for each wave run.

Figure 29-Lir DOB, view from behind the paddles.

3.6 Instrumentation used

Wave calibration was carried out before testing both Models; this consisted of running five identical PN waves. During model tests, wave probes are also used to measure the instantaneous wave elevations at various points throughout the tank. Eight different wave probes recorded data, sampling at a frequency of 128Hz at model scale, were set up in the tank as described below in Section 3.7. The six wave probes in a line, positioned between the model location and the wave probes, were installed to analyse the reflections in the basin. The wave probes operate by measuring the resistance of the water between a pair of 1m long parallel rods. The resistance between the rods is proportional to the immersion depth. Electrolysis is prevented using an AC drive from a low impedance current amplifier (Edinburgh Designs, 2021). The wave probes must be calibrated before use and at regular intervals throughout each testing campaign. Wave probe calibration is carried out by fixing the wave probes to a frame and moving the probes upwards and downwards at 50mm intervals. Six calibration points were used, including the start and finish (zero) position (a 200mm range). By varying the immersion depth by a known distance, a relationship is established between the immersion depth and the voltage response to which a linear fit is applied.

Qualisys motion tracking system is used to track the platform motions. Qualisys works by using four motion-tracking cameras set up to focus on the area of the tank where the platform would be moving. The camera pick up the motions of the Qualisys markers on the model, shown below in Figure 30, and output their X, Y, and Z coordinates relative to a global origin at each time step. The sampling frequencies used during testing for Model A and Model B were 64Hz and 100Hz, respectively. The coordinates of each marker on the models are then used to create a rigid body for the model. Qualisys then outputs the motions of the rigid body as its 6DoF. The Qualisys markers are spread around the model as much as possible; this ensures the rigid body gives an accurate representation of the platform motions. Model A was fitted with four reflective markers, one on each of the outer columns on the bow of the model and two on the tower. A similar approach to marker distribution was employed for model B.


Figure 30 - Qualisys motion tracking markers on Model A and view of the type of markers used

Mooring line loads are recorded using load cells. Load cells are calibrated by hanging a steadily increasing set of weights off a string attached to a load cell and then taking the weights off in the same order that they were added. The load cells used are strain gauges; a strain gauge is constructed of a very fine wire, set up in a grid pattern and attached to a flexible backing. When the shape of the strain gauge is altered, the electrical resistance changes. Calibration sets the relationship between the change in electrical resistance and the load-induced on the load cell. A mixture between futek 10lb and EFE 200N load cells were used for both Model A. Model B used futek 10lb load cells only.

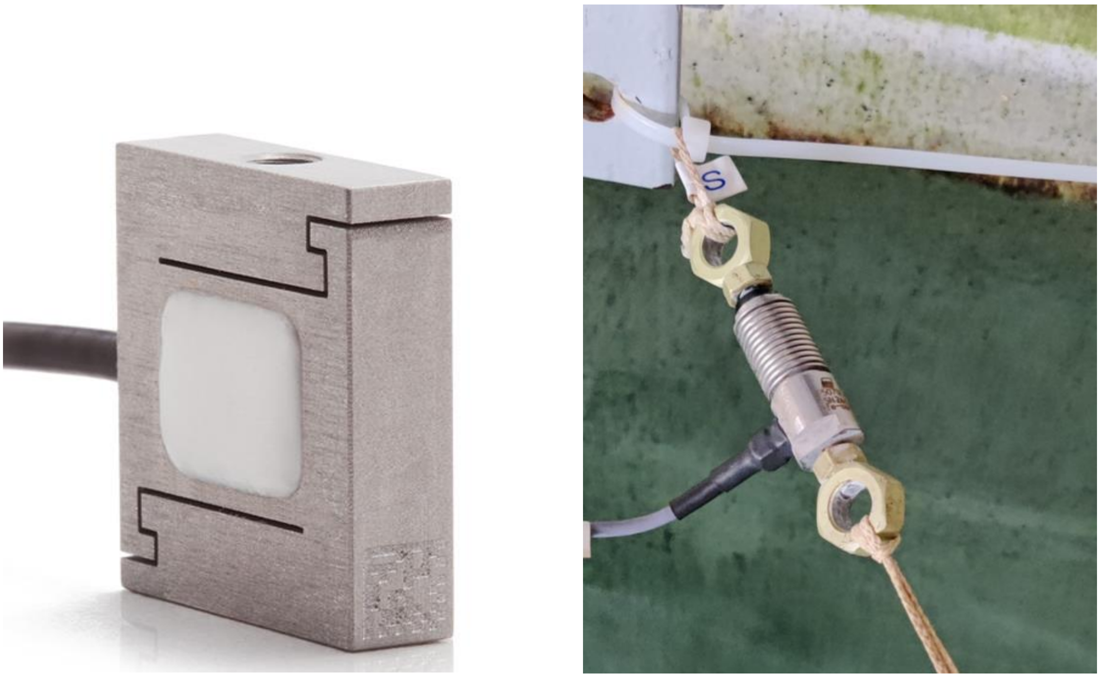

Figure 31 – Futek 10lb load cell (left) and EFE 200N load cell (right)

For ease of analysis, all data files for each test were merged at the lowest recording frequency of all the data recorded. The files were merged in .mat and .txt files

3.7 Wave Tank Testing Setup

3.7.1 Model A

The x-axis of the tank was assumed to lie along the centreline of the tank, with the positive direction pointing towards the paddles from the model location. The y and z axes were according to the right-hand rule.

	Purpose	X-value (Distance from the paddles	Y-value
WP1	Starboard Probe	18.3m	-3.9m
WP2	Model Location	18.3m	0m
WP9	Reflection Probe 1	13.9m	0m
WP10	Reflection Probe 2	14.055m	0m
WP11	Reflection Probe 3	14.2m	0m
WP12	Reflection Probe 4	14.4m	0m
WP13	Reflection Probe 5	14.9m	0m
WP14	Reflection Probe 6	15.8m	0m

Table 8 – Probe locations calibration model A.

The probe locations were the same for testing except for WP2, which was removed entirely and replaced with the model. The wave probes used are described above in Section 3.6

	X-value (Distance from the paddles	Y-value
Starboard	14.7m	-5.9m
Port	14.7m	5.9m
Tower	24.9m	0m

Table 9 – Mooring line fastening points for model A.

3.7.2 Model B

The x-axis of the tank lay along the centreline of the tank, with the positive direction pointing towards the paddles from the model location. The y and z axes were according to the right-hand rule. The location of the mooring fasten points will not be given in this section

	Purpose	X-value (Distance from the paddles	Y-value
WP1	Starboard Probe	16.9m	-3.9m
WP2	Model Location	16.9m	0m
WP9	Reflection Probe 1	13.45m	0m
WP10	Reflection Probe 2	13.605m	0m
WP11	Reflection Probe 3	13.75m	0m
WP12	Reflection Probe 4	13.95m	0m
WP13	Reflection Probe 5	14.45m	0m
WP14	Reflection Probe 6	15.35m	0m

Table 10 – Probe locations calibration model A.

The probe locations were the same for testing except for WP2, which was removed entirely and replaced with the model.

3.8 Test Plan

The full test lists for Model A and Model B are shown below in Appendices 7.1 and 7.2. Table 12 below summarises the tests completed as part of this study. Pink Noise (PN) waves were chosen to give the platform response for as broad a range of frequencies as possible. The upper and lower frequency bounds were set based on the capabilities of the paddles in the LIR DOB. Unlike JONSWAP or Pierson- Moskowitz (PM) wave spectra, where the wave PSD varies across the frequency range, the theoretical PN spectrum has a constant wave PSD between the assigned upper and lower frequency bounds. The significant wave height was set at 0.1m at model scale; this value was chosen based on previous experience. It was observed that 0.1m was the maximum achievable significant wave height for PN waves, without wave breaking occurring before the waves reached the model location. The inputted wave parameters are shown below in Table 11 and the calibration and analysis process is explained below in Sction 3.9. For each variation carried out, 5 PN tests were conducted, along with three repeats of Surge, Heave and Pitch Decay tests; where possible and where necessary, the decay tests were done with and without the wind emulation system active.

	Min Freq (Hz)	Max Freq (Hz)	Sig Wave Height (m)	Run Time (s)	Repeat Time (s)
Model Scale	0.258	1.111	0.1	660	600
Full Scale(1/60th)	0.0333	0.1434	6	5112.34	4647.58

Table 11 – PN wave parameters

Model	Variation Number	Wind System	Mooring System	Inertia
A	1	Thruster Ifremer	MaRINET2	Baseline MaRINET2
A	2	Thruster Ifremer	MaRINET2	Inertia Variation A
A	3	Thruster Ifremer	MaRINET2	Inertia Variation B
A	4	Pulley	MaRINET2	Baseline MaRINET2
A	5	Pulley	MaRINET2	Inertia Variation A
A	6	Pulley	MaRINET2	Inertia Variation B
A	7	Thruster Ifremer	Mooring Var A	Baseline MaRINET2
A	8	Thruster Ifremer	Mooirng Var B	Baseline MaRINET2
B	9	SiL	Catenary	Baseline Model B
B	10	SiL	Catenary	Model B Variation A
B	11	SiL	Catenary	Model B Variation B
B	12	Thruster MaREI	Catenary	Baseline Model B

Table 12 – Summary of tests carried out with variations indicated

The different variations were chosen to show the potential impact that the parameters that contributed most significantly to experimental uncertainty could have on the platform motions. These most prominent sources of uncertainty, i.e., the inertia and CoG, the mooring system, and the wind emulation system, were chosen based on the research conducted in (A. N. Robertson et al., 2018). The magnitude of the variations was dictated by previous experimental experiences and evidence from publications on the topic. The extent of the variations, accompanied by an explanation for these changes, are shown below in Section 3.10. The initial setups are explained for model A and model B are explained in Section 3.2.1

and Section 3.2.2 above. Throughout each variation, the mass and draft of each platform remained constant. Variations 1-12 will be hereby referred to as *V1*, *V2*, *V3*, ….., and *V12.*

3.9 Wave Calibration

Wave Calibration was performed before both model test campaigns. This section aims to highlight the repeatability of waves in the LIR DOB. Previous studies in the facility have shown that uncertainty due to the repeatability of the paddles is very low for both regular and irregular JONSWAP waves (Judge et al., 2021). While a study has not yet been carried out to investigate the repeatability of PN waves in the basin, given the results of previous investigations, it was expected that the repeatability of PN would be no different from JONSWAP or regular waves. The results obtained during wave calibration proved that this was the case. The calibration waves were compared using the following metrics:

The significant wave height, H_s, the average height of the highest one-third of waves, which is given by

$$H_s = 4\sqrt{m_0}$$

Equation 50

where m_0 is the zeroth spectral moment, given by

$$m_0 = \int_0^\infty S_\eta df$$

Equation 51

The zero-up crossing period, T_z, is given by

$$T_z = \sqrt{\frac{m_0}{m_2}}$$

Equation 52

where m_0 is the zeroth moment, and m_2 is the second moment; however, for the calculation of T_z, the zeroth and second moments are calculated between the max frequency generated, *f1* and the minimum frequency generated, *f2*, rather than between 0 and infinity, like in Equation 51, so therefore

$$m_0 = \int_{f1}^{f2} S_\eta df$$

Equation 53

$$m_2 = \int_{f1}^{f2} f^2 S_\eta df$$
Equation 54

The energy period, T_{-10}, is the variance weighted mean period of the one-dimensional period density spectrum; it is given by

$$T_{-10} = \frac{m_{-1}}{m_0}$$
Equation 55

where m_0 is the same as in Equation 53 and m_{-1}, the 1st negative moment is given by,

$$m_{-1} = \int_{f1}^{f2} f^{-1} S_\eta df$$
Equation 56

The final metric used for the comparison between the repeat waves is the significant wave steepness S_s (Brodtkorb et al., 2000); an estimate of which can be deduced from

$$S_s = \frac{2\pi H_s}{g{T_z}^2}$$
Equation 57 (Brodtkorb et al., 2000);

where g is the acceleration due to gravity, 9.81m/s^2. Unlike in Equation 50, H_s is not calculated using the m_o from Equation 51 but instead using the m_0 from Equation 53. Thus, S_s is only calculated for waves that lie between *f1* and *f2*.

For all PN waves used in this study,

f1 = 0.0333Hz

f2 = 0.1434Hz

where *f1* and *f2* are the upper and lower frequency bounds.

Calib No	Frequency Range (Hz)	Input H_s (m)	Actual H_s (m)	T_z (s)	T_{-10}	S_s
1	0.0333-0.1434	6	6.00	10.74	13.21	0.35
2	0.0333-0.1434	6	6.05	10.66	13.12	0.36
3	0.0333-0.1434	6	6.06	10.66	13.11	0.36
4	0.0333-0.1434	6	6.09	10.65	13.09	0.36
5	0.0333-0.1434	6	6.06	10.66	13.12	0.36
Average			6.05	10.67	13.13	0.36

Table 13 – Comparison between calibration waves at model A full-scale.

Calib No	Frequency Range(Hz)	Input H_s(m)	Actual H_s(m)	T_z(s)	T_{0_1}	S_s
1	0.0333-0.1434	6	-0.94%	0.62%	0.62%	-1.46%
2	0.0333-0.1434	6	-0.03%	-0.14%	-0.12%	0.11%
3	0.0333-0.1434	6	0.17%	-0.11%	-0.14%	0.31%
4	0.0333-0.1434	6	0.63%	-0.24%	-0.30%	0.83%
5	0.0333-0.1434	6	0.17%	-0.13%	-0.08%	0.20%
Standard Deviation			0.58%	0.35%	0.35%	0.86%

Table 14 – Deviations from the average value at model A full-scale.

The PN waves were created using the Edesign wave synthesis software that is used to control the paddles. As mentioned in Section 3.8, these use of PN waves is favourable because it gives and even distribution of wave frequencies between the pre-defined upper and lower bounds and gives a picture of platform motions across a wide range of frequencies. These upper and lower bounds are set based on the capabilities of the paddles and the tank.

The results that are shown in Table 13 and Table 14 highlight that there is a slight variation between the five repeat waves. The PSD of each wave time-series was obtained using a FFT. The data was then smoothed with a moving average of 7 points to eliminate any noise in the data output. The inputted wave parameters have been explained Calibration wave 1 has the most significant deviation from the average; even for this wave case, H_s, T_z and T_{-10} are less than 1% away from their respective average values. The significant wave steepness has a deviation of just over 1%. Overall, the standard deviation of each of the metrics is less than 0.21%; reflecting the repeatability of the wave repeats. Reflections were present within the tank; however, the purpose of this paper is not to quantify the effect of the reflections on platform motions, and so they have not been considered in the analysis. The effect of the reflection has neither been quantified nor removed. Given the repeatability of each wave run, the assumption was made that the magnitude of the reflections in the tank does not change from repeat to repeat.

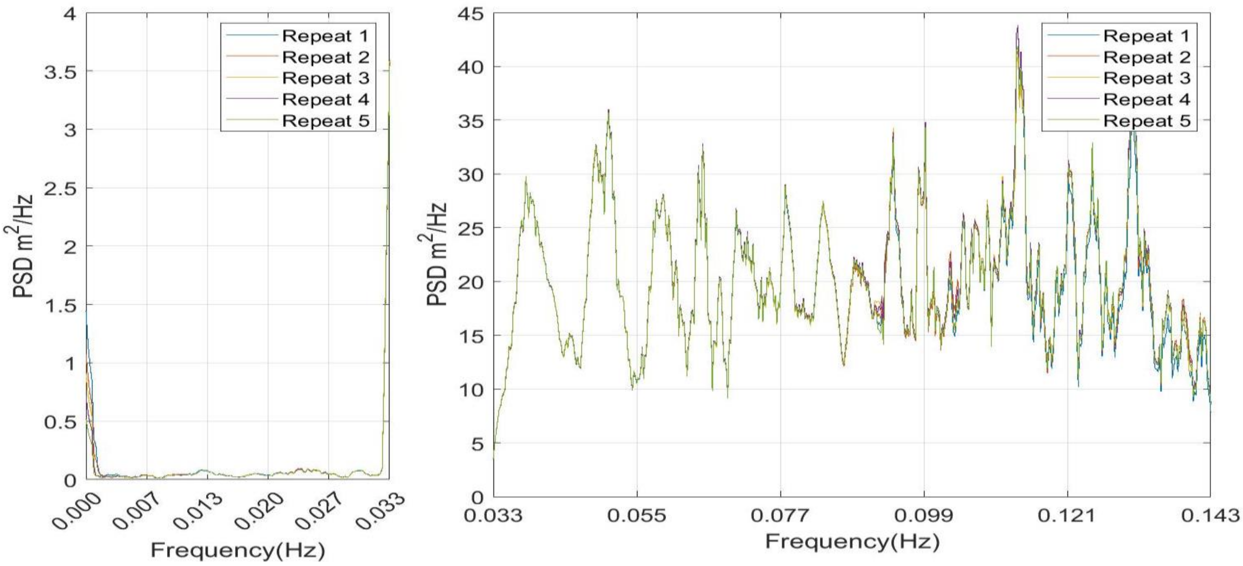

Figure 32 – PSD of the PN time series for each repeat in the low-frequency range (left) and the wave-frequency range(right).

Figure 32 emphasises what has already been demonstrated in this section. The repeatability of the PN spectrum varied depending on the wave frequency. Within the wave frequency range, the repeatability of the waves decreased with increasing wave frequency. The paddles in the DOB are 2.5m hinged paddles and are designed to produce lower frequency waves with larger amplitudes than some of those produced in the PN spectrum. As a result, their ability to create highly repeatable waves decreases with increasing wave frequency. Overall, the repeatability of the waves was not considered a primary contributor to uncertainty in the tank and so will not be investigated further.

3.10 Test Setups

3.10.1 Model A Inertia Variation A – *V2* and *V4*

The only difference between *V1*, *V2*, and *V3,* as outlined in Table 12, is the inertia and CoG of the platform. The mass of the body and the configuration of the mooring system remained the same. The change in inertia was based on the difference between the expected model parameters of model A and the realised model parameters, shown in Table 7. While a difference between the expected and realised model parameters is expected, only so many features can be incorporated into the initial model design that allows for a correction of the discrepancies between the two designs. In the case of model A, its initial function was for an interfacility study and not to assess the performance of the model or validate a numerical model. Consequently, the model parameters were inconsequential if they remained the same in every facility involved in the study (Gueydon, Judge, O'shea, et al., 2021). The motivation for this variation was to assess what effect such a change in the moment of inertia would have on the platform motions.

The inertia of model A was on average 14% larger than expected when it arrived in the lab. Therefore, the pitch inertia, I_{yy}, of model A was reduced by 13.69%. This was accepted because it was not possible to increase the inertia by that magnitude, and so, KG_z, of model A was reduced by 8.6%. The updated inertia and CoG values are shown in Table 15 and Table 16.

CoG Position			
	x-axis	y-axis	z-axis
Distance from reference point	Bow	Centreline	Keel
Actual Reading	26.94	0	12.069

Table 15- Model A Inertia Variation A; location of CoG at full-scale.

	I_{xx}	I_{yy}	I_{zz}
Inertia (tn.m^2)	27249528.2	29694236.7	20357461.4
Radius of gyration (m)	32.73	34.17	28.29

Table 16 – Model A Inertia Variation A; Inertia Values at full-scale.

The inertia was changed by removing masses attached to the thruster at the top of the tower and repositioning them to the columns on the platform. 1.2kg (259.2tn) was removed from the top of the tower, and 0.4kg (86.4tn) was placed onto each column.

3.10.2 Model A Inertia Variation B – *V3* and *V6*

Model A inertia variation B was decided based on the type B uncertainty in the bifilar and trifilar method. This was the inertia case for *V3* and *V6*. Using the MCM, an error of 3% was approximated for the bifilar and trifilar methods. In the end, the I_{yy} of the model for inertia variation B was reduced by 3.6% compared with inertia variation A. This equated to an overall

17.38% decrease compared to the initial I_{yy} reading. This change in inertia equated to a further 2%, and overall, 10% reduction in the KG_z value.

CoG Position			
	x-axis	y-axis	z-axis
Distance from reference point	Bow	Centreline	Keel
Actual Reading	27.06	0	11.799

Table 17 – Model A Inertia Variation B; location of CoG at full-scale.

	I_{xx}	I_{yy}	I_{zz}
Inertia(tn.m^2)	26218126.1	28423619.7	20225089.8
Radius of gyration (m)	32.11	33.43	28.20

Table 18 - Model A Inertia Variation B; Inertia Values at full-scale.

When compared with the initial setup, 1.5kg (324tn) was removed from the top of the tower, and 0.5kg (108tn) was placed on each of the columns.

3.10.3 Model A Wind emulation system variation – *V4*, *V5*, and *V6*

For *V1*, *V2*, *V3*, *V7*, and *V8*, the thruster wind emulation system described in Section 3.2.1 was used. However, for *V4*, *V5*, and *V6*, a weighted pulley system was employed. Like the thruster, a weighted pulley emulates thrust only. The weighted pulley was chosen as an alternative wind emulation due to its low cost and easy setup. The success of the method would determine whether it is a viable option for low-budget wave tank testing projects in the future. The model inertia was the same in *V4* as in *V1*, and *V5* was the same as *V2,* and *V6* was the same as in *V3*. The thruster was left on top of the model as before, and then a line was attached to the CoG point of the nacelle and led horizontally to a pulley a distance away from the model. The line was fed through the pulley and attached to a weight equal to the equivalent thrust force that the thruster would have produced.

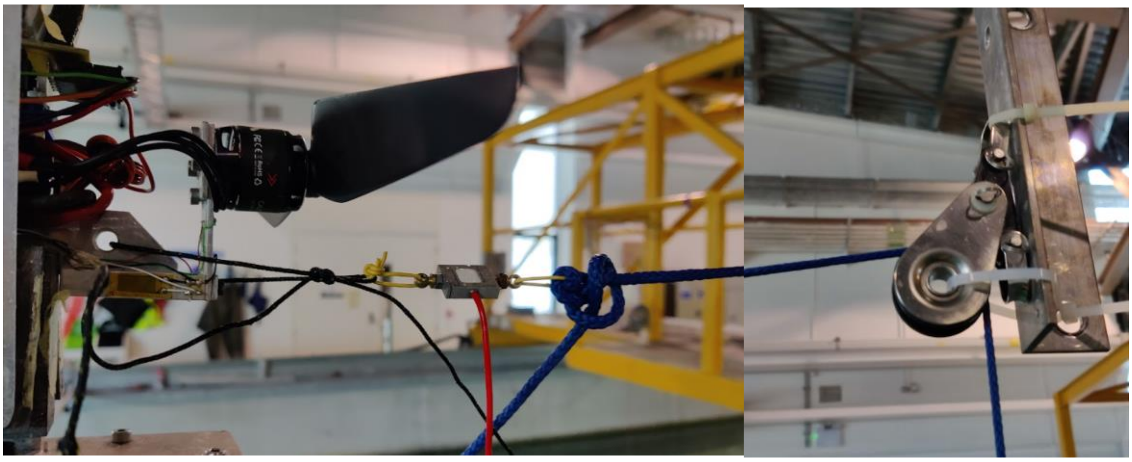

Figure 33 – Pulley system employed for V4, V5, and V6. The attachment point to the thruster (left) and the pulley used(right).

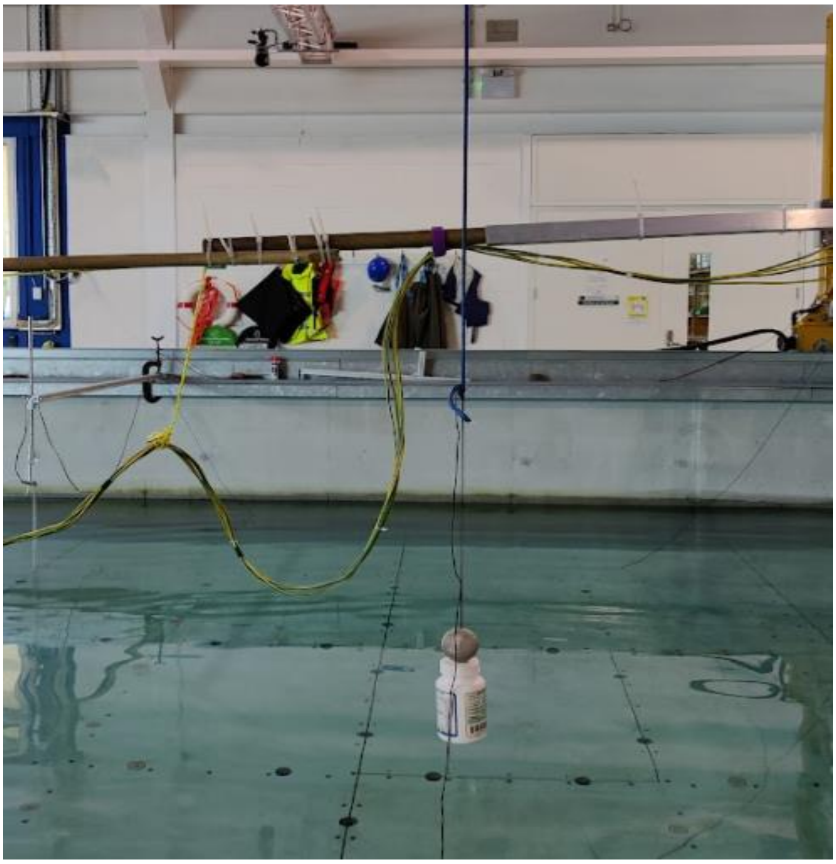

Figure 34- Weight attached to simulate thrust

Figure 35 - Close-up view of the pulley used during testing

The ball-bearing pulley used was selected from those available in the facility at the time. The pulley had a trough of width 8mm. The centre had a diameter of 10.2mm. The outer diameter of the pulley was 40.44mm, and the inner diameter was 33mm. There were other pulleys available on-site with larger diameters and lower friction coefficients; however, they had no slot, so if the model was to sway, yaw or roll at any point, the concern was that the line would slip out of the notch. Then the test would have to be voided.

The pulley system emulated thrust forces by placing weights into the container shown in Figure 34. The mass of lead pellets placed in the container dictated the thrust experienced by the model. Table 19 shows how the masses should have been added and how they were added. The values in brackets are the full-scale values. Lead pellets with an average mass of 3.5g allowed the mass to be adjusted with a high degree of accuracy. It was not always possible to get the mass precisely right. However, the masses were always accurate to within 0.14%. The thrust forces that the pulley system has sought to emulate are the thrust forces generated by the ifremer thruster (shown in Figure 23) and have been described in Section 3.2.1.

Thrust Force Model Scale (***Full-Scale***)	Correct Mass to be applied	Actual Mass applied
3N (648kN)	0.3058kg (***66.0528tn***)	0.3066kg (***66.2256tn***)
5N (1080kN)	0.5097kg (***110.088tn***)	0.5094kg (***110.0304tn***)
7N (1512kN)	0.7136kg (***154.1232tn***)	0.7135kg (***154.116tn***)
8N (1728kN)	0.8155kg (***176.1408tn***)	0.8144kg (***175.9104tn***)

Table 19 – Masses added to the pulley to emulate thrust.

3.10.4 Model A Mooring Variation A – *V7*

V1 – V6 used the same mooring system, this was the linear-horizontal mooring system that was used during the MaRINET2 study, as described in Section 3.2.1. Model A Mooring Variation A was used for *V7*. The value chosen was based upon the potential uncertainty in the value for the spring constant, *k*. While linear mooring systems are not used in practice, this comparison is intended to demonstrate how chnages in mooring stiffness can influence device responses. A decrease in the spring stiffness of 3% was chosen for *V7*. This was based on the error in the load extension method of spring calibration. The method involved adding known masses to the spring and measuring the extension. The sources of error included; errors due to parallax, errors in measuring from an inconsistent point and inconsistent stiffness' of the springs used in the system. This error was then rounded up so that the uncertainty due to the method of spring calibration was not underestimated. Much like with model fabrication, when giving the specifications of a spring to a spring maker, the likelihood that the spring will be precisely as per the specifications is low. A 3% reduction in the spring stiffness relative to the initial setup would have given an average spring stiffness of 44.31kN/m. However, in this case, the actual reduction was less than 3%, as the springs that arrived had a stiffness very similar to the initial system. The actual reduction was just 0.7%.

	Tower	Port	Starboard
Spring stiffness (kN/m)	44.89955	45.53127	45.70711

Table 20 - Mooring Variation A; Spring Stiffness'

3.10.5 Model A Mooring Variation B –*V8*

Model A Mooring Variation B was used for *V8*. A 3% increase in the spring stiffness relative to the initial setup was chosen for *V8*. However, much like for *V7*, the springs were not as per the desired specifications. The actual springs that arrived were stiffer than planned. Had a 3% increase in the stiffness occurred, then the spring stiffness for *V8* would have been on average 47.05kN/m. Instead, the actual springs arrived with an average stiffness of 53.49kN/m; this reflected a 17% increase in the average spring stiffness compared with the initial setup.

	Tower	Port	Starboard
Spring stiffness (kN/m)	52.69488	53.45744	54.30765

Table 21 – Mooring Variation B; Spring stiffness'

3.10.6 Model B Inertia Variation A –*V10*

Model B Inertia Variation A was used for *V10* of the testing campaign. Model B was far heavier than model A. As a result, it was more challenging to adjust the inertia of the model by moving weights around the model. Existing masses positioned at the top of the tower and within the tower were relocated. The masses were evenly distributed to locations on the model above the still water line so as not to affect the hydrostatic stiffness of the model. Moving these masses reduced I_{yy} by 8.4% and KG_z by 9.8% compared to the initial setup.

3.10.7 Model B Inertia Variation – *V11*

All the available masses had been moved for Model B Inertia variation A. Consequently, for inertia variation B, used for *V11*, it was not possible to reduce I_{yy} or KG_z further. Some of the masses removed from the top of the tower were moved back to their original location. This has the effect of increasing both the I_{yy} and KG_z of the model relative to the original setup. Compared to the initial setup, I_{yy} was 4% less, and KG_z decreased by 5.6%.

3.10.8 Model B wind emulation system variation –*V12*

The software in the loop system utilised for *V9*- *V11* can be expensive to use if there is not a system available "in-house". SIL can be complicated to set up in terms of installation and in terms of formatting the data correctly so that the SIL can interpret the data and adjust the outputted thrust and torque accordingly. As a result, it was decided that a comparison between the SIL system and a simple thruster would be beneficial. This was completed in *V12*; the physical properties of model B for *V12* were the same as the physical properties in *V9*. The thruster used is shown below in Figure 36. Masses had to be added to the thruster so that inertia and CoG of the platform and the UCC thruster was the same as the inertia of the platform and the SIL system. Unlike the Ifremer thruster, where propeller blades provide the thrust, the UCC thruster provides thrust through impeller blades.

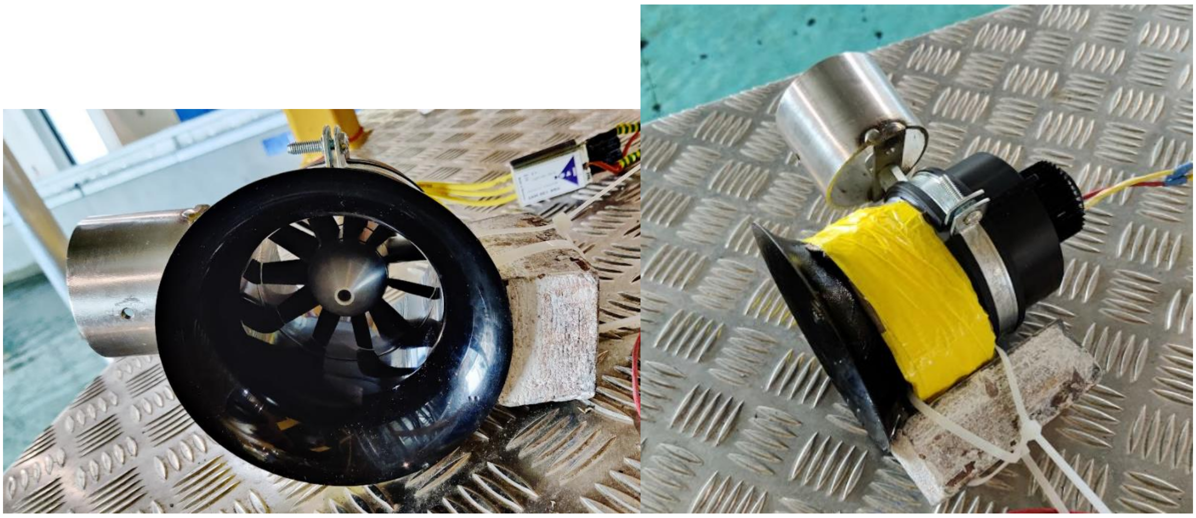

Figure 36 – Thruster used for Variation 12

Another critical difference between the UCC thruster and the Ifremer thruster was the ease of operation. The Ifremer thruster was controlled with the help of an Arduino board that allowed it to be operated from a PC in the control room. The UCC thruster was switched on and off with a dial placed on the DOB footbridge. The dial was dimensionless; as a result, the thruster had to be calibrated so it could produce a thrust equal to the average thrust produced by the SIL system. The average thrust produced was approximately 10.5N. The constant thrust used in *V12* was set as the average thrust from the SIL system in *V9*.

The thruster was calibrated by fastening it to a large, light, and smooth piece of polystyrene. The polystyrene was placed in the tank, as shown in Figure 37. A lightweight, inextensible line with a load cell attached at the end was attached to a fixed point and then attached to the thruster itself. The thrust was recorded on the load cell, and the dial was turned until the thrust arrived at 10.5N. This point on the dial was marked so that the thrust could be replicated for each repeated test. The thrust was decreased and increased to this point on several occasions during the calibration to check for errors due to drift in the loadcell or hysteresis.

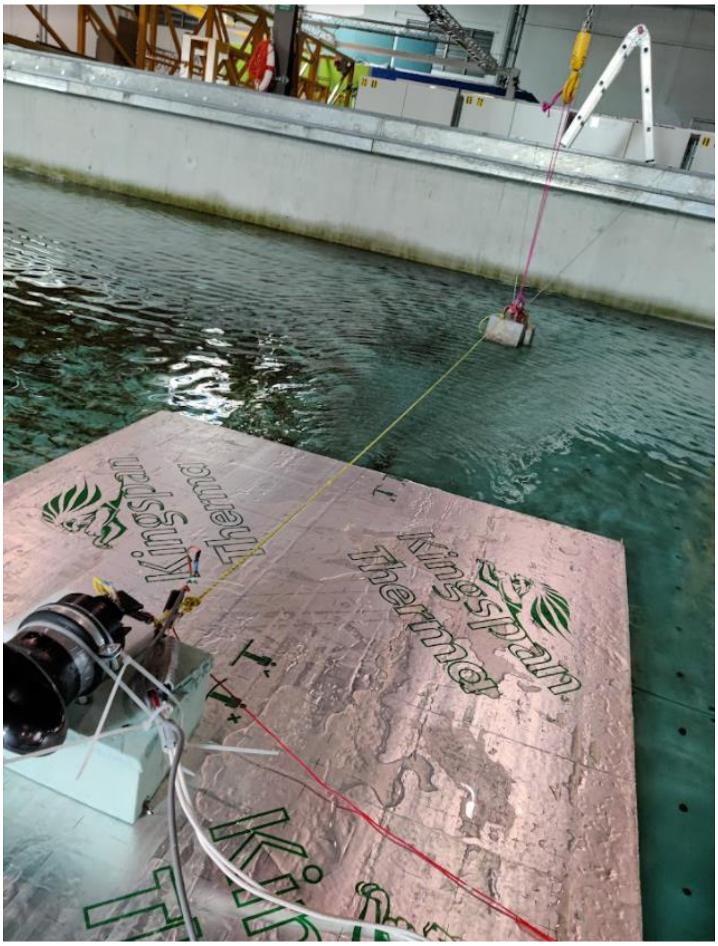

Figure 37 - UCC Thruster during the calibration procedure.

3.10.9 Summary

Table 22 gives a summary of the variations completed. The base case for model A is *V1*, and the base case for model B is *V9*.

Variation	Wind System	% change in k relative to base case	% change in I_{xx} relative to base case	% change in I_{yy} relative to base case	% change in I_{zz} relative to base case	% Change in KG_Z relative to base case
1	Thruster Ifremer	-	-	-	-	-
2	Thruster Ifremer	-	-7.24086	-7.09682	0.18258	-8.56818
3	Thruster Ifremer	-	-9.01328	-9.10622	-0.14367	-10.61364
4	Pulley	-	-	-	-	-
5	Pulley	-	-7.24086	-7.09682	0.18258	-8.56818
6	Pulley	-	-9.01328	-9.10622	-0.14367	-10.61364
7	Thruster Ifremer	-0.7	-	-	-	-
8	Thruster Ifremer	17%	-	-	-	-
9	SiL	-	-	-	-	-
10	SiL	-	-8.46244	-8.46244	2.34979	-9.86534
11	SiL	-	-4.01243	-4.01243	-3.53144	-5.61131
12	Thruster MaREI	-	-	-	-	-

Table 22 – Summary of variations made.

3.11 In-water decay tests

Decay tests are performed to assess the natural period of oscillation of the model about each degree of freedom. Decay tests can also be used to identify the damping ratio and added mass of a model. The damping ratio is a dimensionless measure describing how many oscillations in a system decay after a disturbance. Added mass is the inertia added to a system because an accelerating or decelerating body must move (or deflect) some volume of surrounding fluid as it moves through it. During this study, surge, heave, and pitch decay tests were performed for each variation. For model A, decay tests were performed with the water depth set to 0.9m in the tank, and this allowed the individuals conducting the experiments to manually conduct each of the decay tests from within the tank. For model A, the z CoG was below the still water line, and the mooring lines were attached to the top of the outer columns above the CoG and the still water line. To conduct the surge decay tests, a line was attached to the tower column at a point such that, when the line was pulled horizontally and released, a pure surge motion was induced. This location had to be found iteratively and changed depending on the model and mooring properties.

Heave decay tests were performed by applying an equal force at equal distances from the line of the x CoG along the line of the y CoG. Pitch decay tests were performed by applying a force on either side of y CoG such that the moments about the CoG due to the forces applied were equal in opposite directions. This was achieved using a spring balance pulling up at the stern and using lead masses at the bow, and the two were released at the same time to induce a pitching motion.

For model B, decay tests were more difficult to perform. The draft of model B was such that it was not possible for the decay tests to be performed from within the tank. This meant that the oscillations had to be performed from the moveable footbridge, which was positioned above the tank; the footbridge is shown in the background of Figure 22, Figure 23, and Figure 30. A visual basis was used to decide which tests contained pure oscillations and which tests contained impure oscillations. If the oscillation was impure, then the test was not considered for evaluation. For example, if the device pitched or yawed when conducting a surge decay test the then the test would be restarted.

4 Analysis and Discussion

This chapter examines the effect that each of the variations had on the platform responses. The repeatability of the platform response is first assessed by comparing the PSDs for the 6DoF and the mooring responses. The repeat tests are then compared using three metrics. Two of which, T_r and $M_{WF,}$ have been described in Section 2.5.5, and the other, a new metric $T_{r,\,mag,}$ which will be explained in this section. The influence of the changes in inertia for both models is first assessed, followed by the influence of different wind emulation systems for both models. Finally, the effect of the mooring system variations for model A is investigated. The change in platform responses brought about by each variation is assessed using a combination of any of the three metrics mentioned above. This is a progression from what has been done in (A. N. Robertson et al., 2018) and aims to further develop an understanding into magnitude and effect of uncertainties during wave tank testing of FOWT's. The conclusions from each set of variations are also presented.

4.1 Repeatability

4.1.1 Model A

Section 3.8 and 3.9 highlights how the wave spectra were created and why PN waves were chosen for the analysis. As seen in Section 3.9 the paddles in the DOB can produce highly repeatable PN waves, particularly at lower frequencies. Five wave runs were completed for each testing condition, and an average of the motions was taken from the five repeats. Simillar to the wave data, the PSD of the platform responses were obtained from the qualisys data using an FFT, where the data was smoothed with a moving average of seven points to remove any noise. The PSDs could then be used for comparison purposes and to output the response metric for each test. Using the average values, comparisons between the different variations were then carried out. The validity of this method relies on the repeatability of the platform motions for each repeated test. An initial comparison between each repeat was completed visually, and then the repeats were compared using the metrics. The metrics used for the repeat comparison are used to compare the effect of each variation on model responses. The visual comparison, shown in Figure 38, was completed by comparing the PSD of the platform response in each of the 6DoF and the PSD of the mooring response. The repeat tests completed during *V7* were used to conduct this comparison.

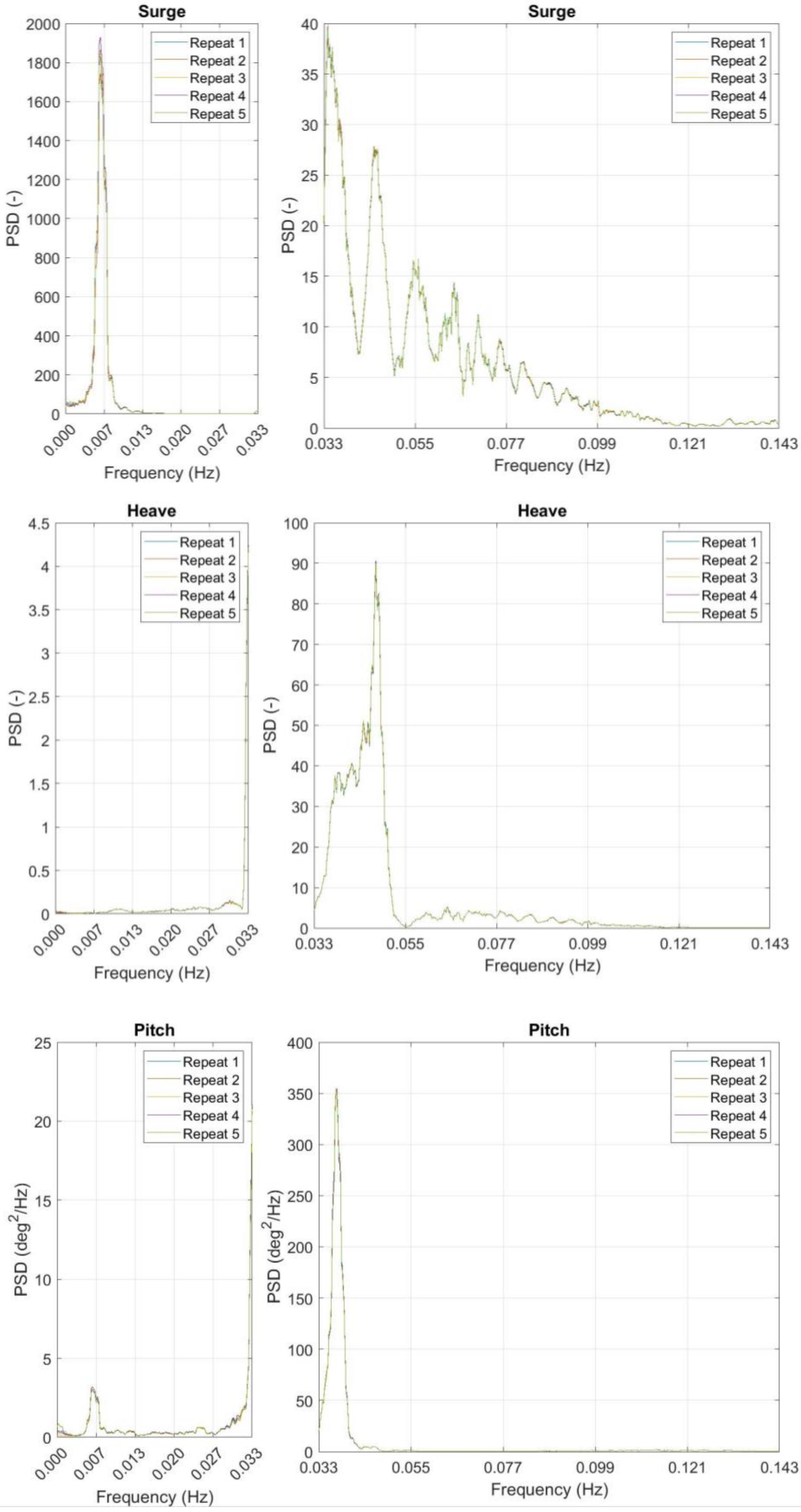

Figure 38 – Variation in PSD for surge, heave, and pitch for repeats of Model A

The primary motions of interest for this research are surge, heave and pitch. Figure 38 demonstrates that the responses of the model in these main motions of interest are very repeatable within the wave frequency range, the right-hand plots in Figure 38. However, in the low-frequency plots, the PSD of the surge response for each repeat is less repeatable. This is emphasised due to the fact that surge is a low-frequency response, so surge responses are largest in the low-frequency range. The 85-minute time series allows for a fully developed sea-state in the wave frequency range for PN waves, but it does not allow for a fully developed sea-state in the low-frequency range (Gueydon, Judge, O'shea, et al., 2021).

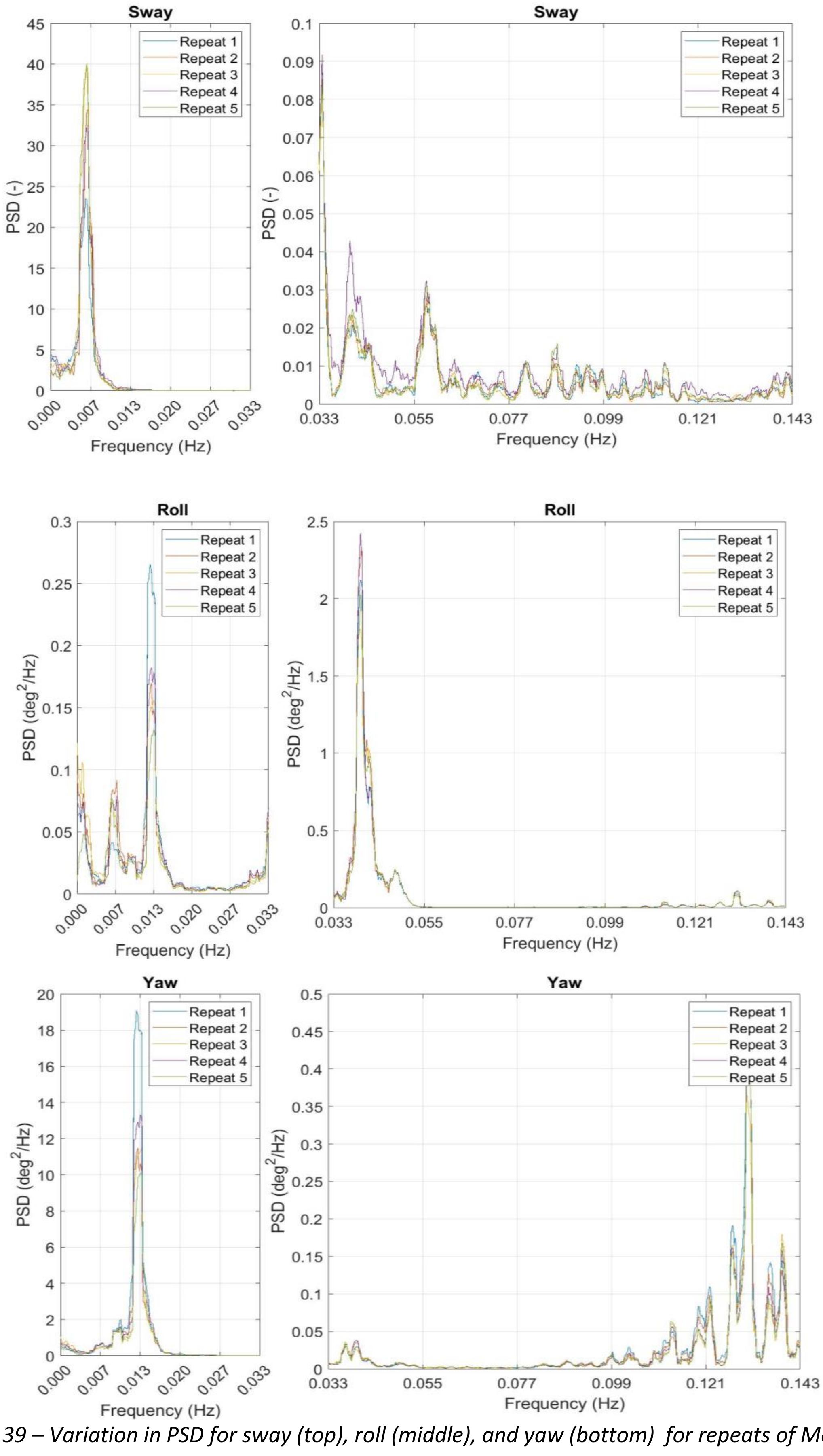

Figure 39 – Variation in PSD for sway (top), roll (middle), and yaw (bottom) for repeats of Model A.

The platform responses in sway, roll and yaw were not a primary focus of this study. The differences between the repeats are more evident for these responses, as demonstrated by Figure 39. One of the reasons for the poor repeatability is that the magnitude of platform responses for these motions was a lot lower than for surge, heave, and pitch. As a result, any variance between the magnitude of the responses for each repeat would be a lot more evident for these lower magnitude responses.

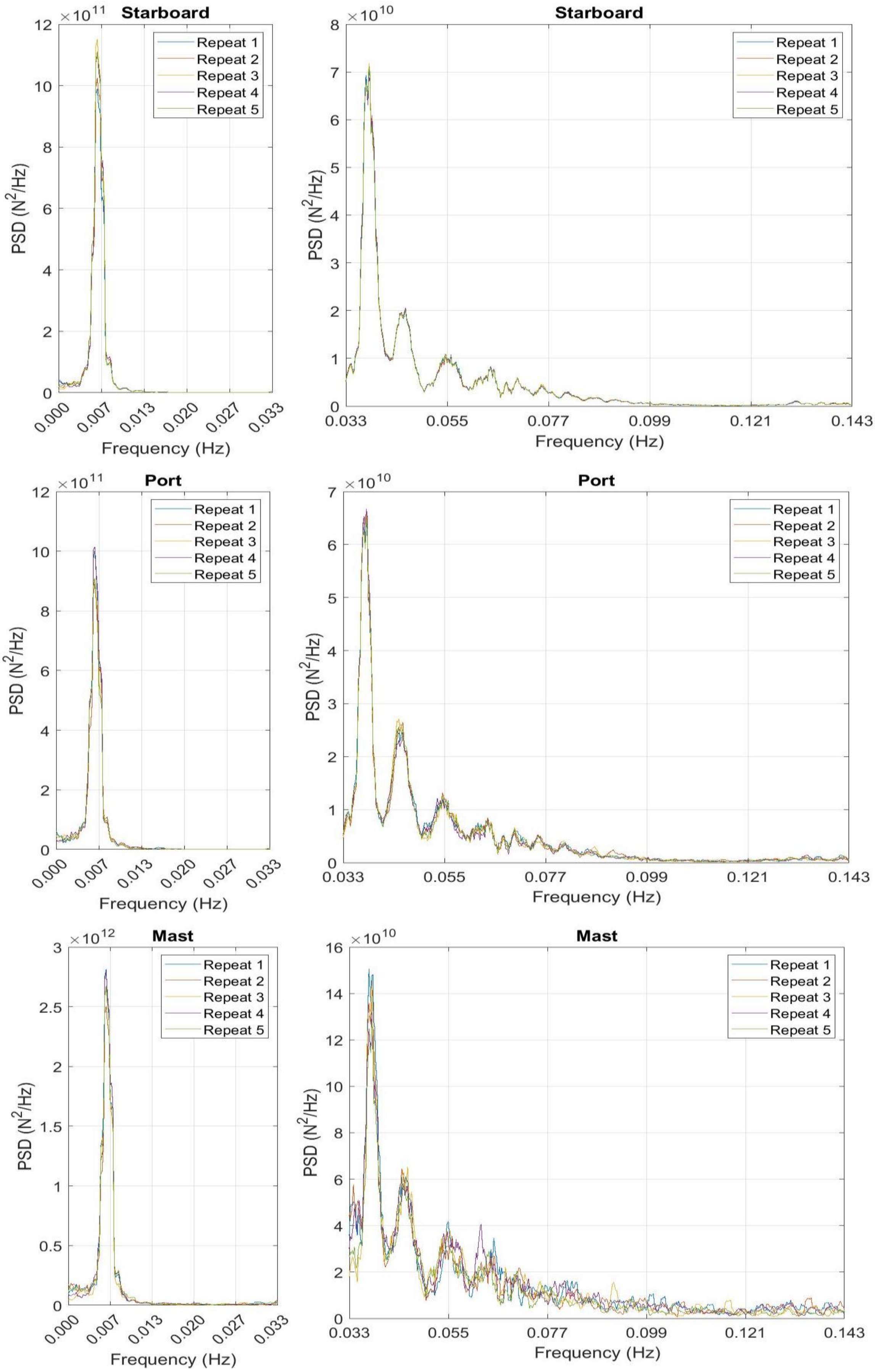

Figure 40 – Variation in PSD of mooring line responses for repeats of Model A.

There is a high level of repeatability for the mooring responses in the wave-frequency range, as demonstrated by the plots in Figure 40. However, the signal for mooring response is noisier than the individual motion responses. Mooring line responses are dictated by platform motions in all 6DoF. As a result, any variance in the platform responses will be reflected in the mooring response. In addition, the surge response of the platform is the dominant factor that influences the repeatability of mooring responses in the low-frequency range. Consequently, the variance in the surge response for the low-frequency range is reflected in the mooring responses for this range.

While it is useful to compare data graphically, metrics aid a straightforward comparison between repeat tests or different sets of results. The repeatability of the primary responses of interest is compared using the metrics introduced in Section 2.3.5. The metric M_{WF} shown in Equation 45 has been sufficiently explained. Graphical data aids the explanation of the metric T_r, Equation 47 and a new metric $T_{r,\,mag}$, which will be introduced in this section. The metric T_r represents the period of resonance response and uses a formula like that used to calculate the peak wave period, T_p. Where T_p is the frequency between zero and infinity at which the PSD of the wave signal is greatest. T_r is determined based on the frequency, within the bounds of two frequencies set equal distances on either side of the eigenfrequencies, at which the PSD of the platform response is greatest. The regions shaded in red in Figure 41 highlight the regions used when calculating T_r. The plots shown in Figure 41 are the PSDs of platform motions for *V7*. Table 23 shows how the maximum and minimum frequency bounds were found. All eigenfrequencies (f_e) were found by conducting decay tests to the model. Decay tests were performed with and without wind emulation acting on the model and are described in Section 3.11.

	Eigen Frequency (f_e) Hz (Period (s))	Delta f (δf) Hz	Lower Bound (f_e-δf) Hz (Period (s))	Upper Bound (f_e +δf) Hz (Period (s))
Heave	0.048 (20.66)	0.005809	0.04260 (23.47)	0.054222 (18.44)
Pitch	0.0380 (26.35)	0.005809	0.03215 (31.11)	0.043765 (22.85)
Surge	0.0067 (149.54)	0.005809	0.00088 (1138.95)	0.012497 (80.02)

Table 23 – Frequency bounds used for calculation of T_r.

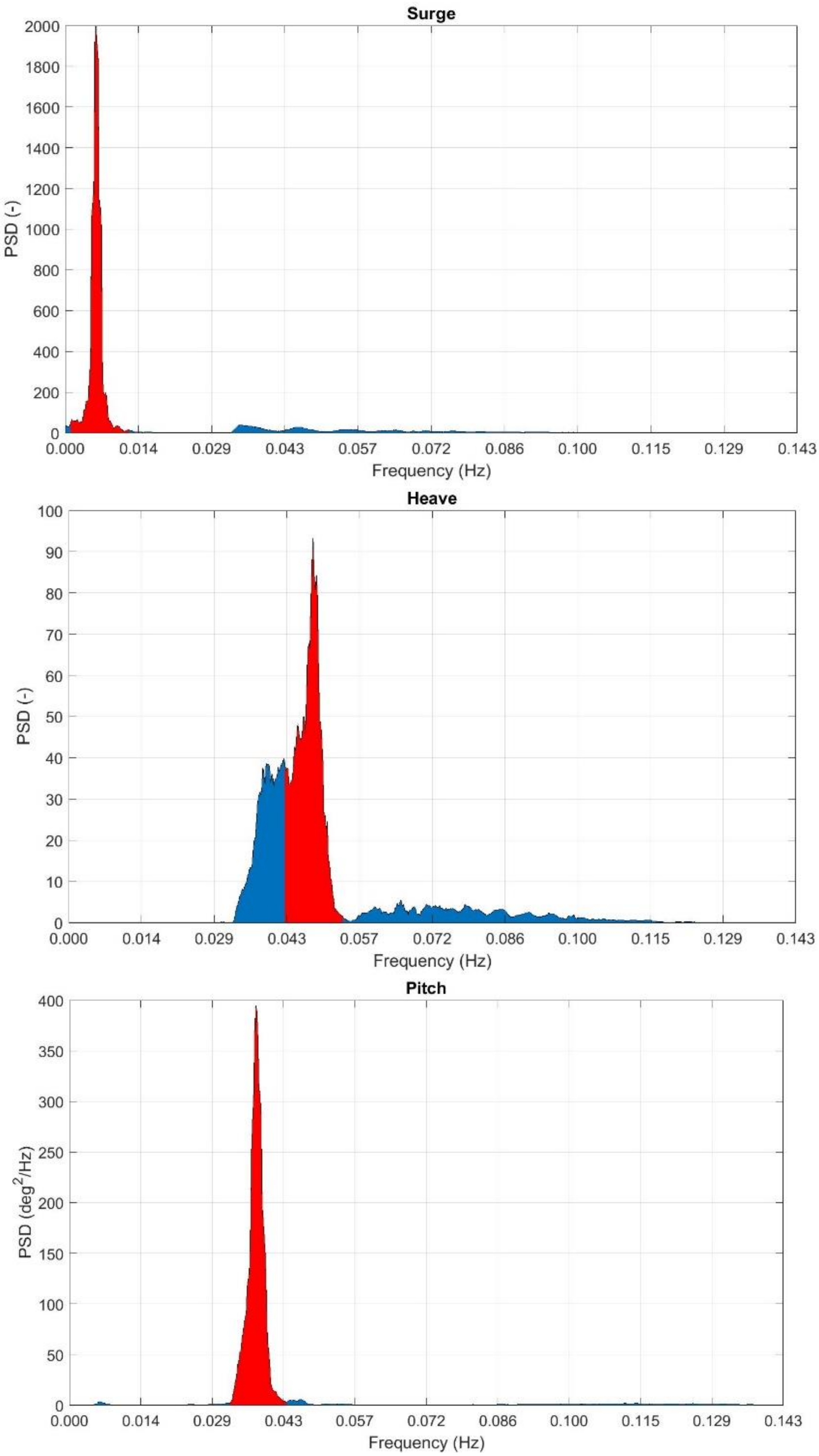

Figure 41 – Regions with bounds of f_1 and f_2 for the calculation of T_r and $T_{r,\ mag}$.

$T_{r,\,mag}$ is calculated using the formula shown below.

$$T_{r,mag} = \int_{f_e-\delta f}^{f_e+\delta f} S_{signal} df$$

Equation 58

where the notation is the same as in Equation 47. $T_{r,\,mag}$ is the integral under the red section of the PSDs shown in the plots in Figure 47. Comparison between the different repeats is more straightforward using the three metrics. The metrics T_r and $T_{r,\,mag}$ are only calculated for the three main motions of interest: surge, heave and pitch. This is because during testing, for each variation, decay tests were performed for these three motions only. As a result, the frequency range needed to calculate these metrics could only be found for the three main motions of interest.

The metric M_{WF} shown below represents the magnitude of platform response in the wave-frequency range. M_{WF} can be calculated for all measures of platform response. However, in most cases, it is not necessary to present any responses other than the three primary responses of interest. For the benefit of demonstrating repeatability, M_{WF} will be shown for all measures of platform response recorded during testing.

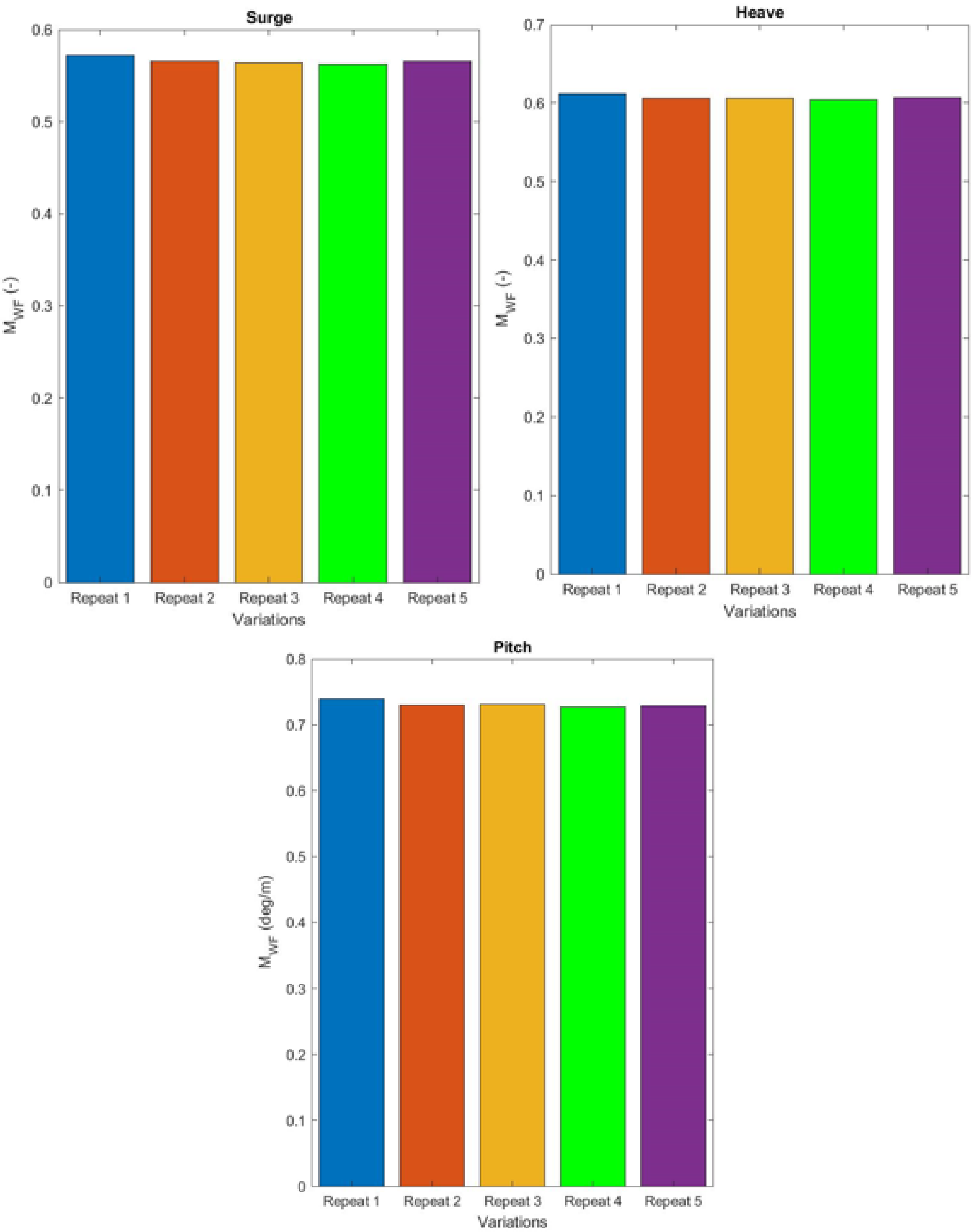

Figure 42 – Variation in M_{WF} in surge, heave, and pitch for repeats of Model A.

The plots shown in Figure 42 indicate good repeatability of the platform responses in the wave-frequency range. This is more significant for pitch and heave because their natural periods lie within the wave-frequency range. There is minimal variability between the values obtained for each repeat test. Surge, heave and pitch had standard deviations of 0.7%, 0.5% and 0.6%, respectively. On the other hand, sway, roll and yaw, shown in Figure 43 below, had standard deviations of 7.3%, 2% and 4.4%. The magnitude of these motions, in comparison to the magnitude of the three main motions of interest, are much smaller, so it was expected that their standard deviations would be bigger. The starboard and port mooring line responses had a standard deviation of just less than 0.8%, and the standard deviation of the tower mooring was just over 3%.

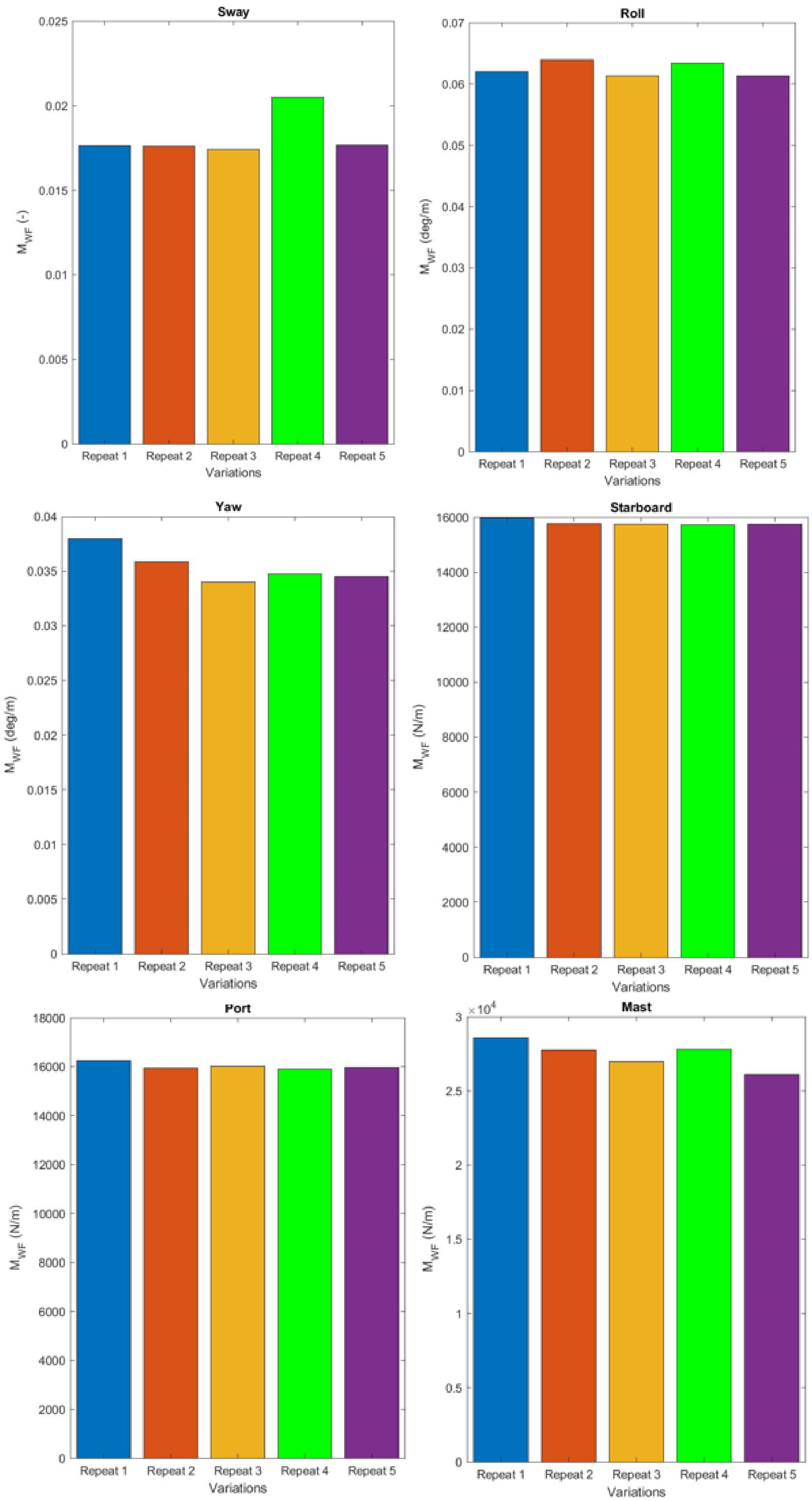

Figure 43 – Variation in M_{WF} in sway, roll, yaw, and mooring line responses for repeats of Model A.

The repeatability of resonance response can be assessed using both the T_r and $T_{r,\,mag}$, with the former representing the period of resonance response for the platform and the latter giving an indication of the magnitude of resonance response. Both metrics combine to demonstrate what can be viewed by looking at the PSD. However, the data is presented with one single metric, making it easier for uncertainty analysis and comparison.

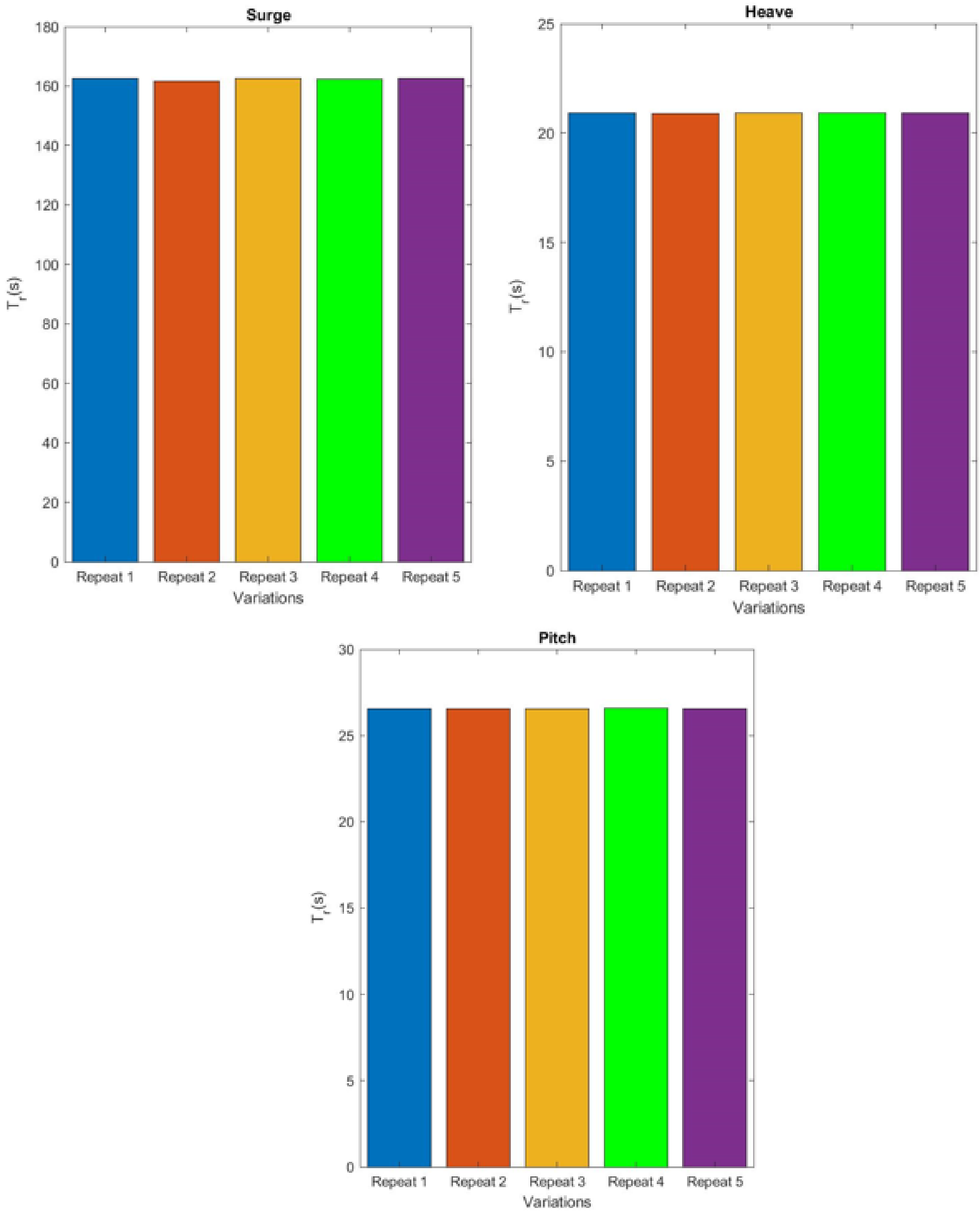

Figure 44 – Variation in T_r in surge, heave, and pitch for repeats of Model A.

The repeatability of the period of resonance response for the platform was excellent, as demonstrated by Figure 44. This can be difficult to determine precisely using the PSD only. For surge, heave and pitch, the standard deviation in T_r for the five repeat tests was less than 0.03%. The repeatability of heave and pitch for $T_{r,\ mag}$ was far better than the repeatability of the surge response, both of which were less than 0.4%. This is because the resonance frequency of surge response lay outside the wave-frequency range, as was discussed earlier in this section with reference to the surge PSD plot. This resulted in a standard deviation of 2.8% for surge.

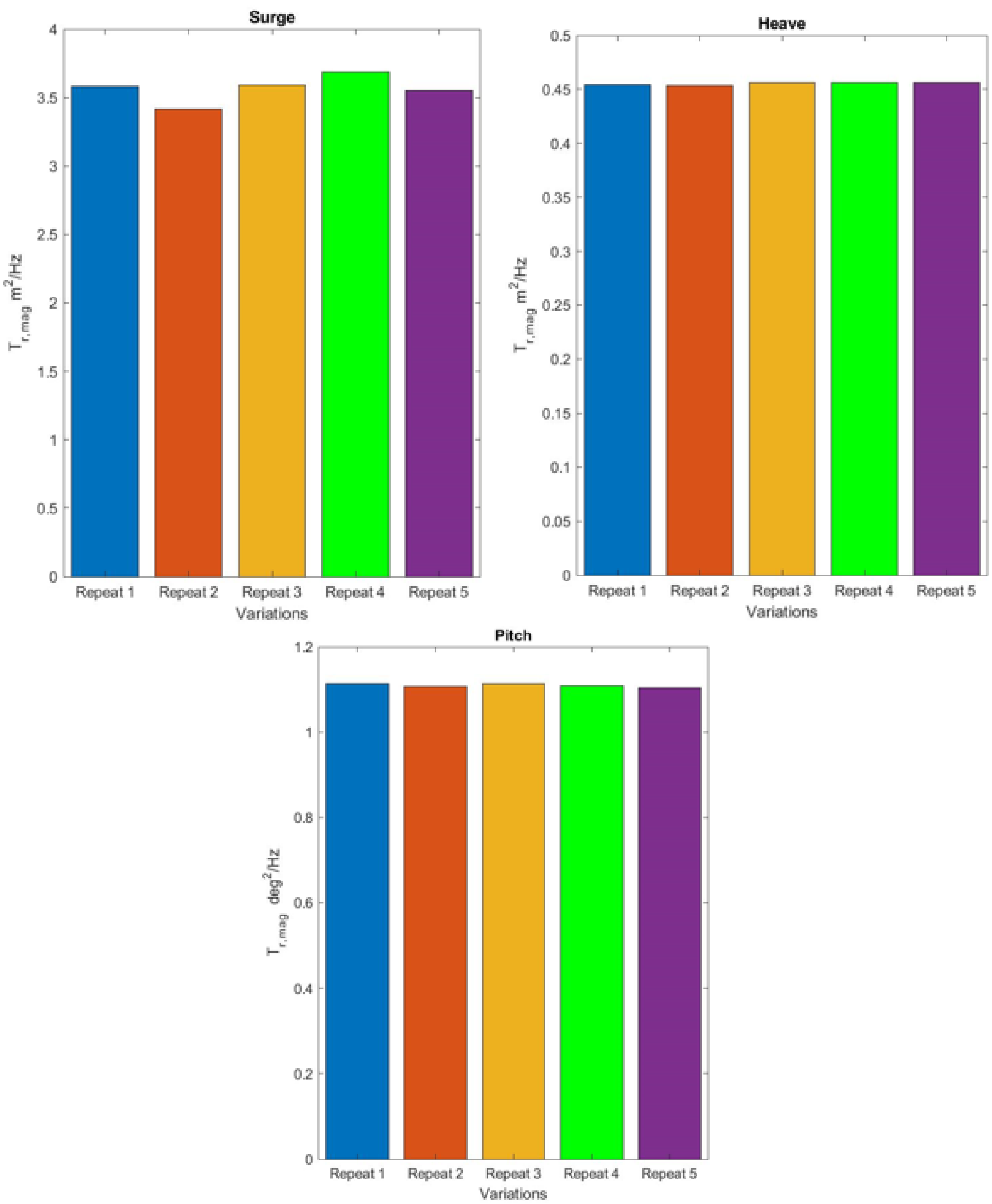

Figure 45 – Variations in $T_{r,\ mag}$ in surge heave, and pitch for repeats of Model A.

Taking the variability of all of the motions for all metrics into account, there is an acceptable level of repeatability for the tests conducted with model A. This was based on the fact that the main motions of interest for each metric, other than $T_{r,\ mag}$ for surge, had a similar level of repeatability to the calibration waves. It was decided that the variability in $T_{r,\ mag}$ for surge could not be mitigated due to the timeframe in which testing had to be completed. The use of the metric $T_{r,\ mag}$ is only possible for this length of test since the same wave conditions are propagated towards the model each time. If a comparison between model responses for different wave conditions was carried out, then $T_{r,\ mag}$ could not be used for surge or any low-frequency responses unless the analysis period allowed for fully developed low-frequency platform responses.

4.1.2 Model B

The repeatability of model B was assessed based on the variance in the values of M_{WF}, T_r and $T_{r,\ mag}$. The analysis of the repeatability of Model A proved that the combination of those three metrics gives a good representation of what is happening across the PSD of the platform. All model B values are presented at the model scale for confidentiality purposes. The platform response during the repeat tests in *V9* was used to complete this assessment.

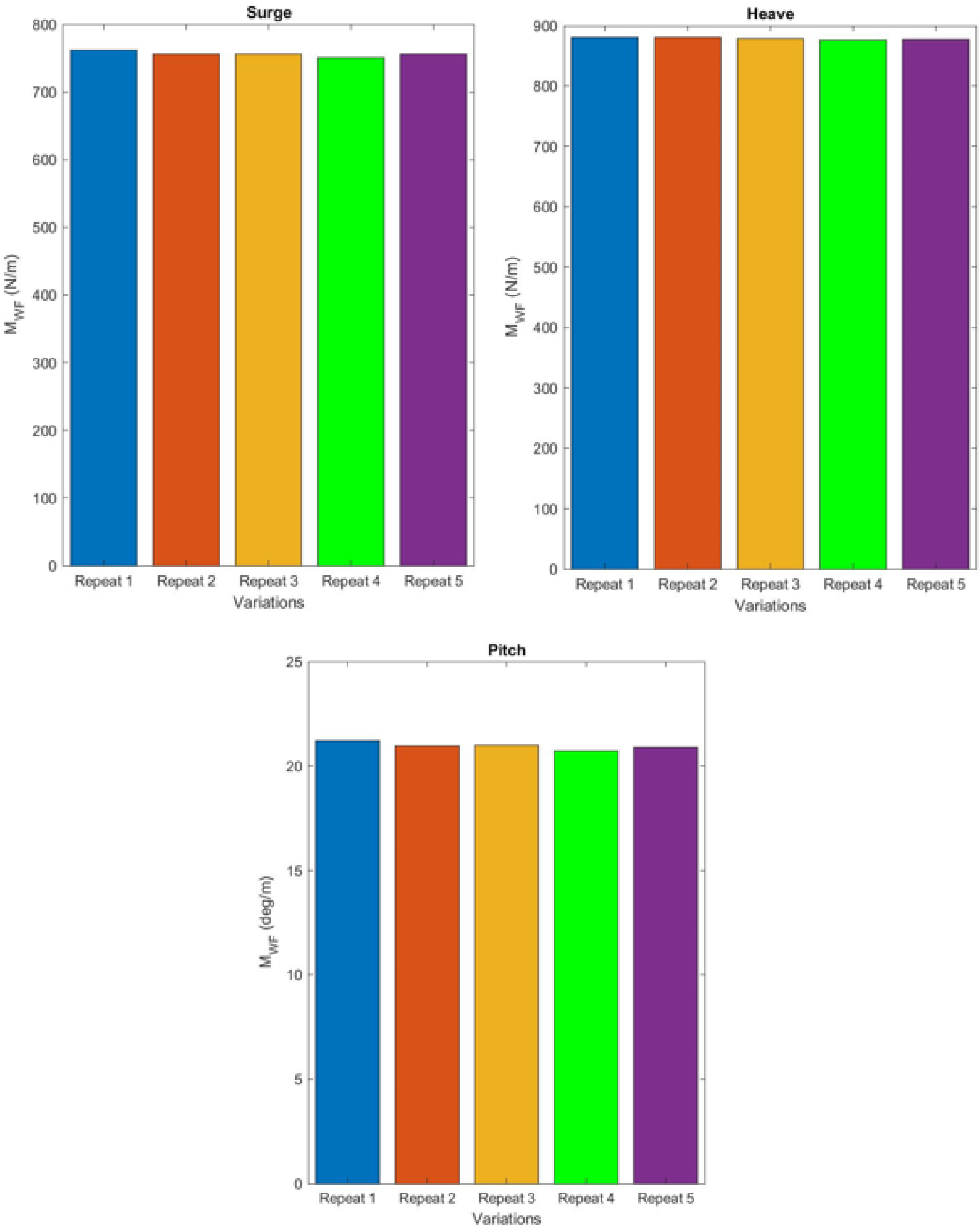

Figure 46 – Variations in M_{WF} in surge, heave, and pitch for repeats of Model B.

The repeatability of M_{WF} for surge, heave and pitch was very good for model B, as is evident from the plots shown in Figure 46. The relative standard deviations of the repeats for surge, heave and pitch are 0.6%, 0.3% and 0.8%, respectively. The standard deviations are similar to the standard deviations for the same values in model A, presented above in Section 4.1.1

Like with model A, the repeatability of model response decreases when considering sway, roll, and yaw. The relative standard deviations of each were 1%, 2% and 13%, respectively. The poor repeatability in yaw was expected as, unlike model A, model B consisted of more than one rigid body. Consequently, the yaw motions were highly irregular and unpredictable. As a result, this large discrepancy between repeat tests was not a cause for concern. Finally, the repeatability of the port, starboard and stern mooring responses were 0.3%, 1.1% and 7.3%, respectively.

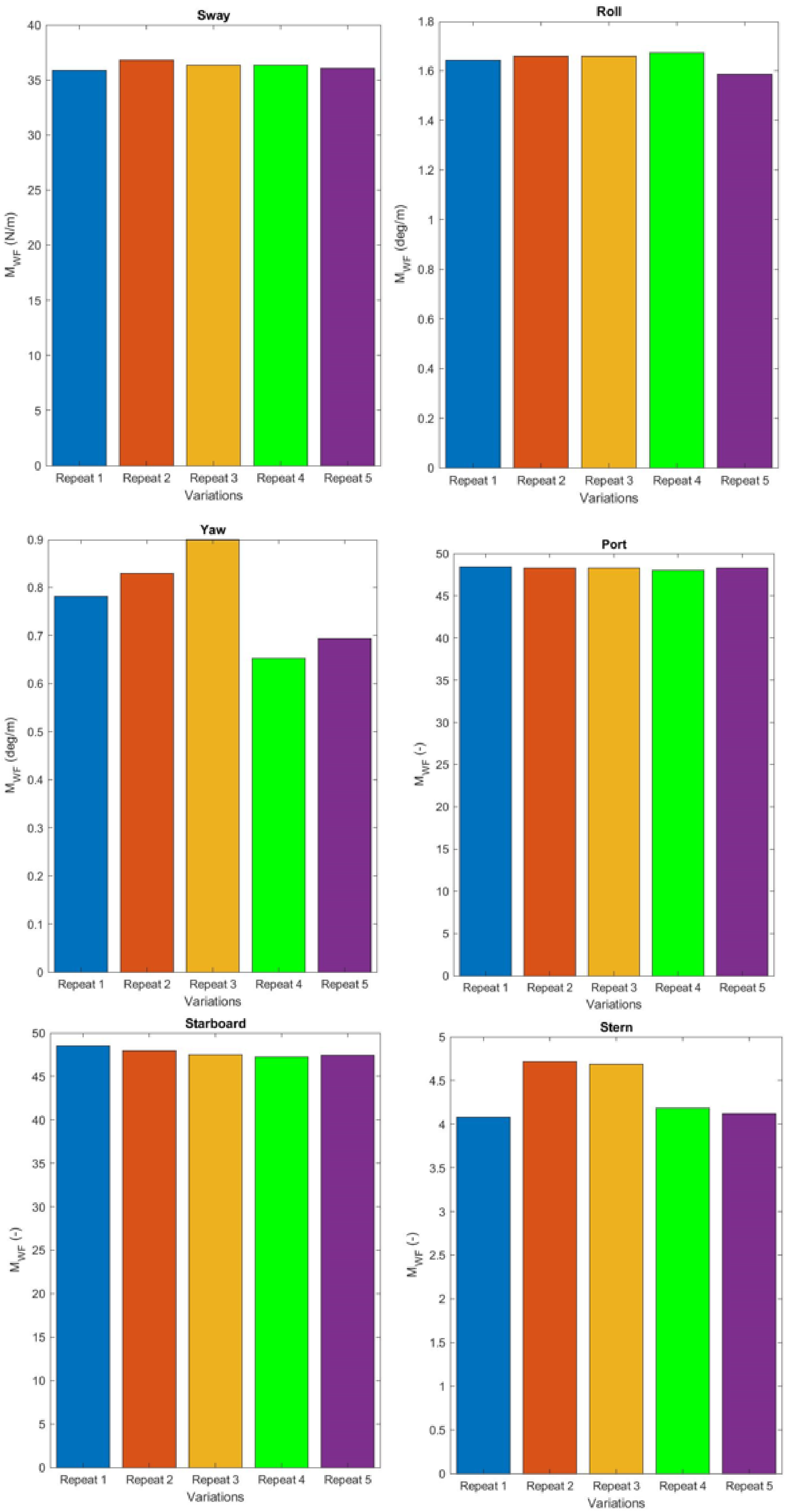

Figure 47 – Variation in M_{WF} in sway, roll, yaw, and mooring line responses for repeats of Model B.

Overall, the repeatability of all motions for M_{WF} was deemed acceptable. The main factor in arriving at this conclusion was the high repeatability of the three main motions of interest. The repeatability of M_{WF} for the main motions of interest for model B was less than the repeatability of the significant wave steepness, S_s, for the calibration waves, which was 0.86%. The plots shown in Figure 48 and Figure 49 below compare the repeat values of T_r and $T_{r,\,mag}$ for the surge, heave and pitch. Much like model A, there are very few discrepancies between each repeat for T_r. However, for $T_{r,\,mag}$, there is a slight variance between the repeats for surge and pitch, particularly surge. There are two main reasons for the discrepancies in surge. The first, which also applies to pitch, is that the body's motion was unpredictable due to the presence of more than one rigid body. The consequence of multiple rigid bodies is that the model as a whole is under the influence of two bodies. This results in combinations of motions between the two bodies that are not present for a single rigid body system. As a result, the likelihood of pure surge, or pitch, in a 6DoF sense is unlikely. This effect is amplified when resonance occurs. The second reason is that the surge resonance peak lies outside the wave frequency range. The run-time used during testing did not allow for a fully developed sea-state in the low-frequency range.

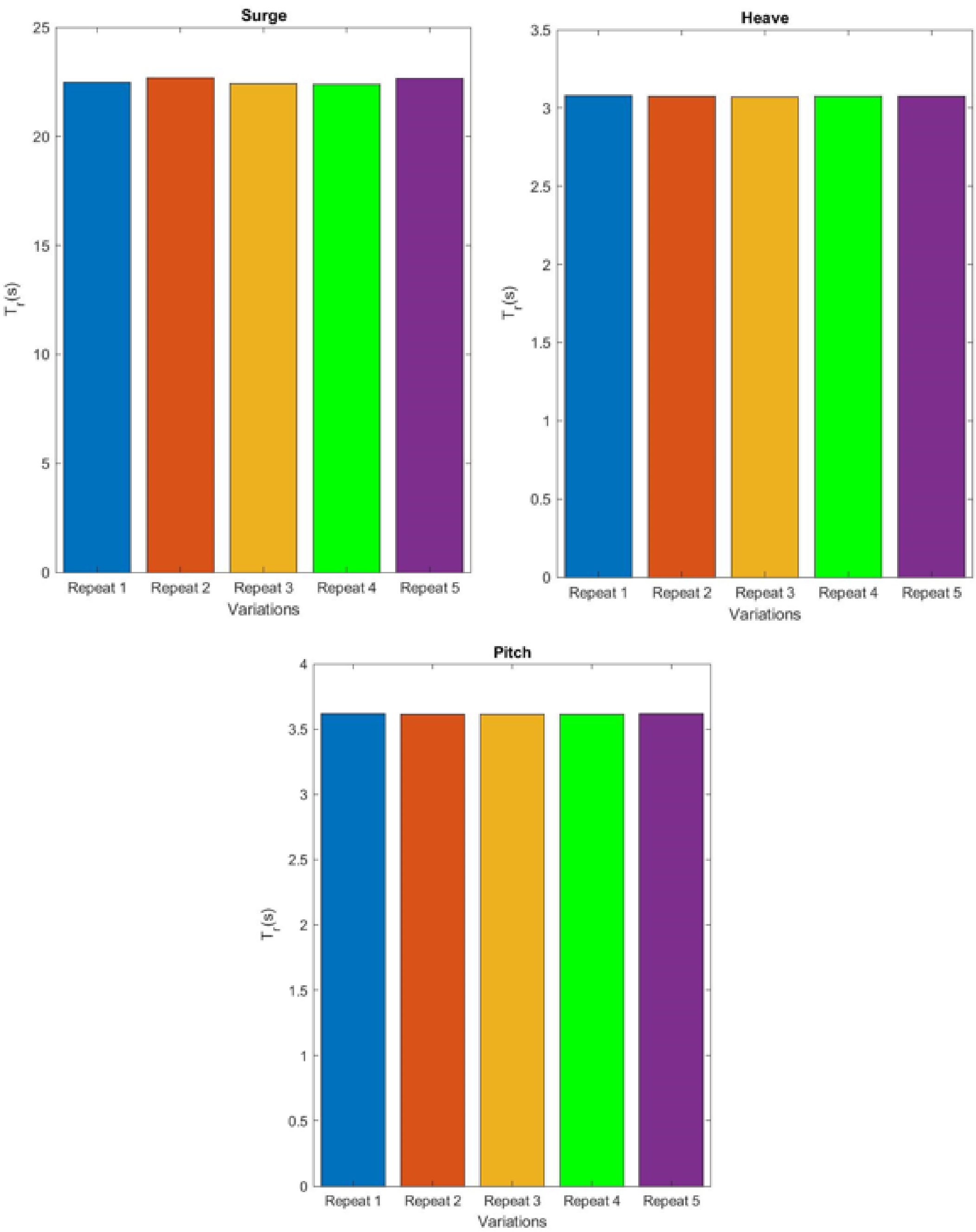

Figure 48 - Variation in T_r in surge, heave, and pitch for repeats of Model B.

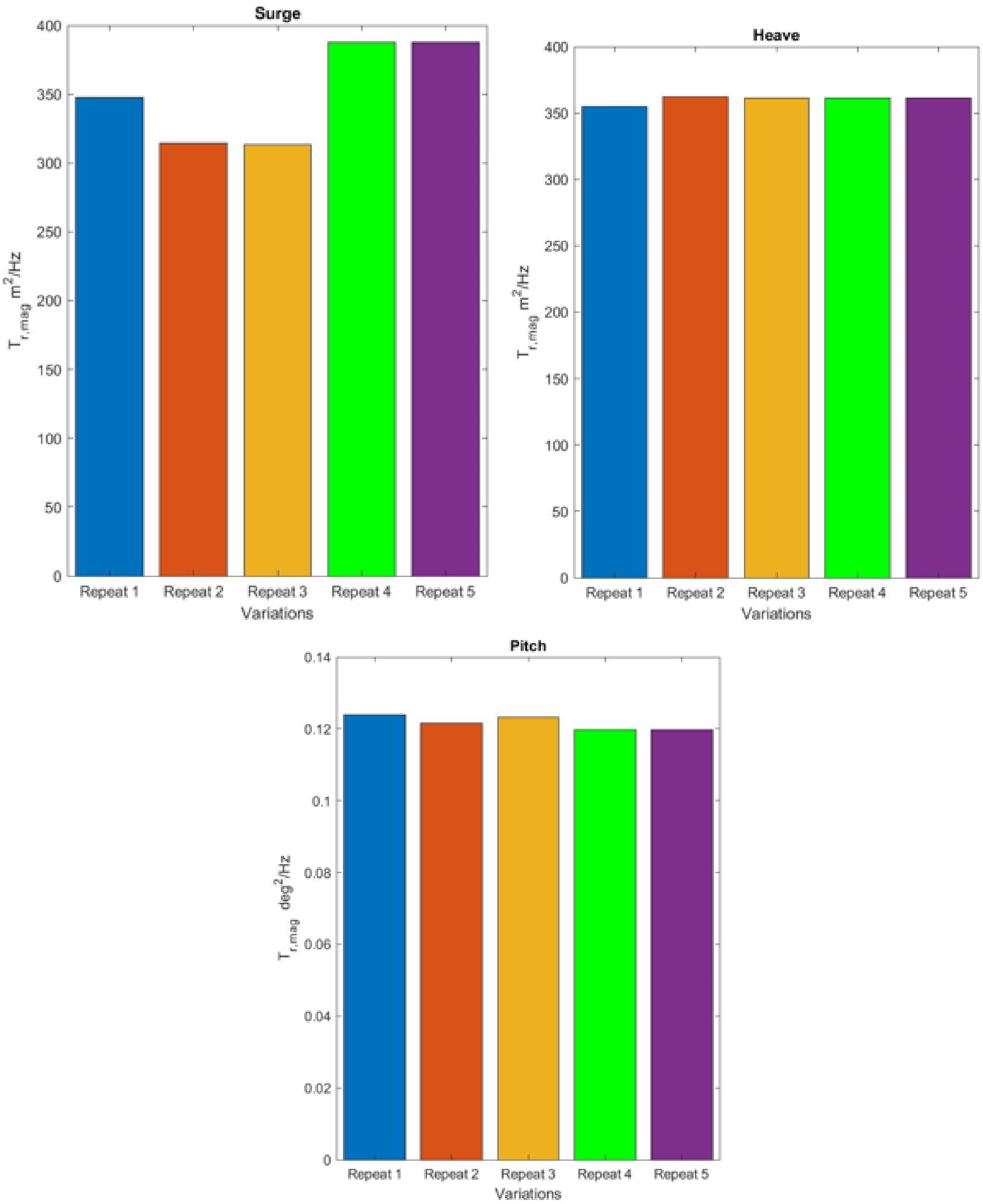

Figure 49 – Variation in $T_{r,\,mag}$

The relative standard deviations of T_r for surge, heave and pitch were 0.6%, 0.1% and 0.01%, respectively. While these values are slightly higher than those obtained during the model A tests, they are more than acceptable. The relative standard deviation of $T_{r,\,mag}$ for surge was 10.6%. For heave it and pitch, it was 0.8% and 1.6%. This increased variance relative to model A can be attributed to the model design and the presence of two rigid bodies.

Considering the variability of all motions for all metrics, it was concluded that there was an acceptable level of variance between each repeat test. This was based on the fact that the main motions of interest for each metric, other than $T_{r,\ mag}$ for surge, had a similar level of repeatability to the calibration waves. It was decided that the variability in $T_{r,\ mag}$ for surge could not be mitigated due to the model design and timeframe in which testing had to be completed. As a result, it was concluded that the method chosen to compare the effect of each variation on platform responses was appropriate.

4.2 Effect of changes in inertia on platform responses

4.2.1 Model A

The inertias of model A and model B were adjusted to assess the impacts of errors and uncertainties in platform inertia and CoG on platform responses. The effect of these changes has been determined by comparing the platform responses in an initial base case to the platform responses when the inertia and CoG of the platform have been adjusted. Table 24 below summarises the changes in model properties for this comparison.

Variation	Wind System	% change in k relative to base case	% change in I_{xx} relative to base case	% change in I_{yy} relative to base case	% change in I_{zz} relative to base case	% Change in KG_Z relative to base case
1	Thruster Ifremer	-	-	-	-	-
2	Thruster Ifremer	-	-7.24	-7.10	0.18	-8.57
3	Thruster Ifremer	-	-9.01	-9.11	-0.14	-10.61

Table 24 – Model Property changes for V1, V2, and V3 relative to the base case, V1

An assessment of the resonance period, T_r, is essential for commercial projects as it allows conditions when platform responses are most significant to be evaluated. In addition, it enables the calculation of the maximum loads on the structure and the mooring lines. During wave tank testing, there is a high probability that either the value of the inertia and CoG obtained during dry-tests will be incorrect due to uncertainty in the methods used to estimate these values or that the model will not be built exactly as per specifications. This comparison highlights the effect these uncertainties could have on the model response. The impacts of two variations to model A inertia and CoG are assessed during this section. The extent of these changes are shown in Table 24, and the rationale behind the changes have been presented in detail in Section 3.10.1 – 3.10.3 of this paper. The plots below show the effect that the changes in inertia had on platform surge. The plots shown are for the inertia variations conducted with the thruster.

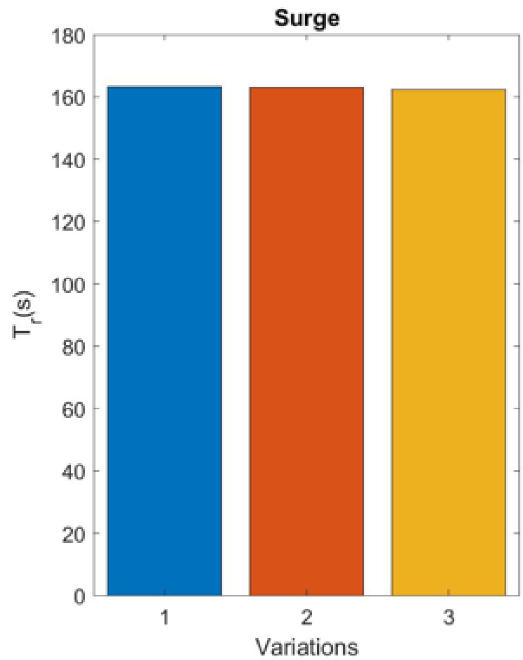

Figure 50 – Change in surge T_r with changes in inertia for model A

As predicted, the variation in inertia had minimal effect on the surge of the platform. Chapter 2 of this report highlighted that the surge period is predominantly affected by the mooring system and the hydrostatic stiffness of the platform in surge, with inertia having a negligible effect. Neither the mooring system nor the hydrostatic stiffness were affected by the inertia variation. The inertia about the x-axis, I_{xx}, is the only parameter that changed for these variations that might have affected T_r for surge. When changing CoG_z, the location of the centre of gravity in z and I_{yy}, the inertia about the y-axis, the value of I_{xx} was changed by default. The value of I_{xx} decreased by 13.9% between *V1* and *V2*. I_{xx} decreased by 17.2% from *V1* to *V3*. Changes in I_{xx} did not affect the period of resonance response. This would suggest that the other two factors, hydrostatic stiffness and mooring stiffness, would influence the period of resonance response most significantly. The latter will be investigated in Section 4.4.

Similarly, for heave, the change in inertia had little to no effect on the resonance frequency of the platform. This was another anticipated outcome of the experiment. The heave eigenfrequency, and thus the heave resonance frequency are dictated by the hydrostatic stiffness in heave and the inertia about the z-axis. Neither of these values were significantly affected by *V2* and *V3*.

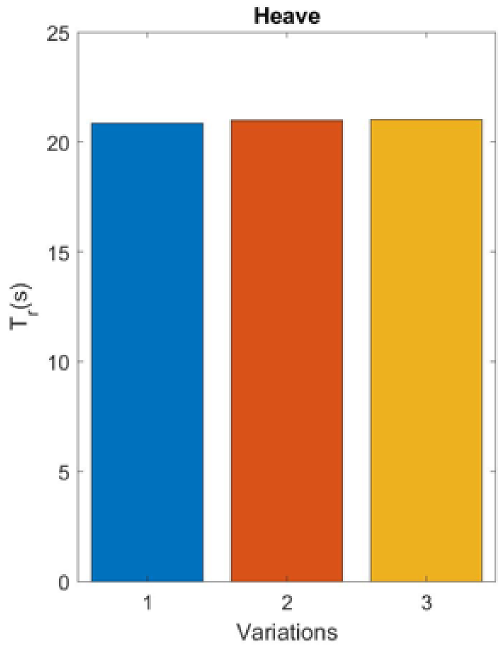

Figure 51 - Change in heave T_r with changes in inertia for model A.

It was anticipated that *V2* and *V3* would significantly affect the resonance frequency of the pitch response. For each variation, both the inertia about the y-axis, I_{yy}, and the location of CoG_z were adjusted. In turn, a change in the location of the centre of gravity affects the metacentric height, GM_L.

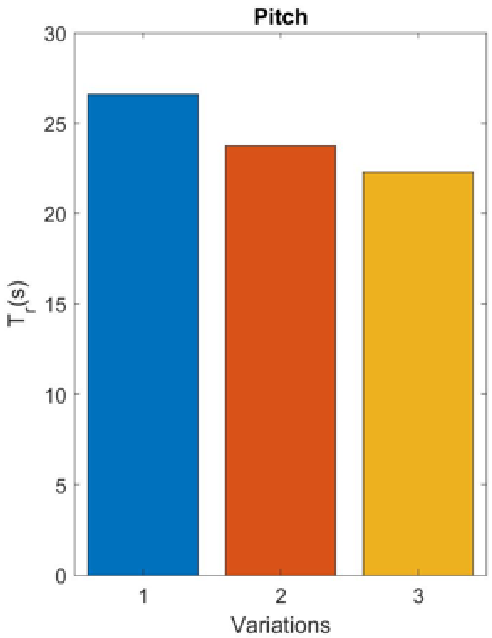

Figure 52 - Change in pitch T_r with changes in inertia for model A.

Figure 52 indicates a sharp decrease in the pitch resonance period, T_r, with decreasing inertia and increasing metacentric height. Decreasing KG_Z, the distance from the keel of the platform to the centre of gravity, has the effect of increasing the GM_L. Increasing GM_L alone would have the effect of reducing the natural period of the model in pitch. Likewise, decreasing the I_{yy} alone would have the effect of increasing the natural period in pitch. When both are decreased together, it significantly affects the pitch natural period of the platform. From *V1* to *V2*, KG_Z, was reduced by 8.6%, and I_{yy} was decreased by 13.7%. This had the effect of reducing the pitch resonance period of the platform by 10.7%, from 26.6s to 23.7s. From *V1* to *V3*, KG_Z was decreased 10%, and I_{yy} was decreased by 17.4%. This reduced the pitch period to 22.3s. This equated to an overall reduction of 16.1% relative to *V1* and a further decrease of 6% compared with *V2*. A far greater reduction in the resonance period was observed for a relatively small change in KG_Z and I_{yy} between *V2* and *V3* compared with *V1* and *V2*.

The magnitude of platform response has been assessed using the $T_{r,\,mag}$ metric and M_{WF} for surge. The magnitude of the platform response expected can be simplified and determined using the formula taken from (Gueydon et al., 2022).

$$X_{\omega k} = \frac{F_{\omega k}}{\sqrt{(-\omega^2.\left(I_{G_{kk}} + A_{G_{kk}}\right) + C_{G_{kk}})^2 + \omega^2 * (B_{G_{kk}} + \alpha)^2}}$$

Equation 59 (Gueydon et al., 2022).

where, $X_{\omega k}$ is the 6DoF motion vector at the CoG, $F_{\omega k}$ is the excitation force, $I_{G_{kk}}$ is the inertia about the CoG, $C_{G_{kk}}$ is the total stiffness at the CoG, ω is eigenfrequency, $B_{G_{kk}}$ is the linear damping, and α is an optimisation parameter; this parameter acknowledges that the level of damping in the wave is not always known.

However, Equation 59 is simply a theoretical relation and what happens in practice is not always in agreement. For example, for a decrease in the inertia and an increase in the metacentric height, a negative trend in pitch response from *V1*, *V2* and *V3* was expected. However, the variations in $T_{r,\ mag}$ for pitch, shown in Figure 53 below, demonstrate that theoretical relations do not always represent what happens in practice. The formula shown in Equation 59 contains simplifications, and these simplifications mean that sometimes not everything is accounted for fully, and the factors that have not been accounted for can influence the motion of the device. Hence why wave tank testing is completed in the first place. It should not be viewed that there should be a choice between one or the other when it comes to the use of theoretical relations and testing. The theory can be used to better explain what takes place during testing, and wave tank testing can be used to improve upon and refine theoretical relations, like that shown in Equation 59.

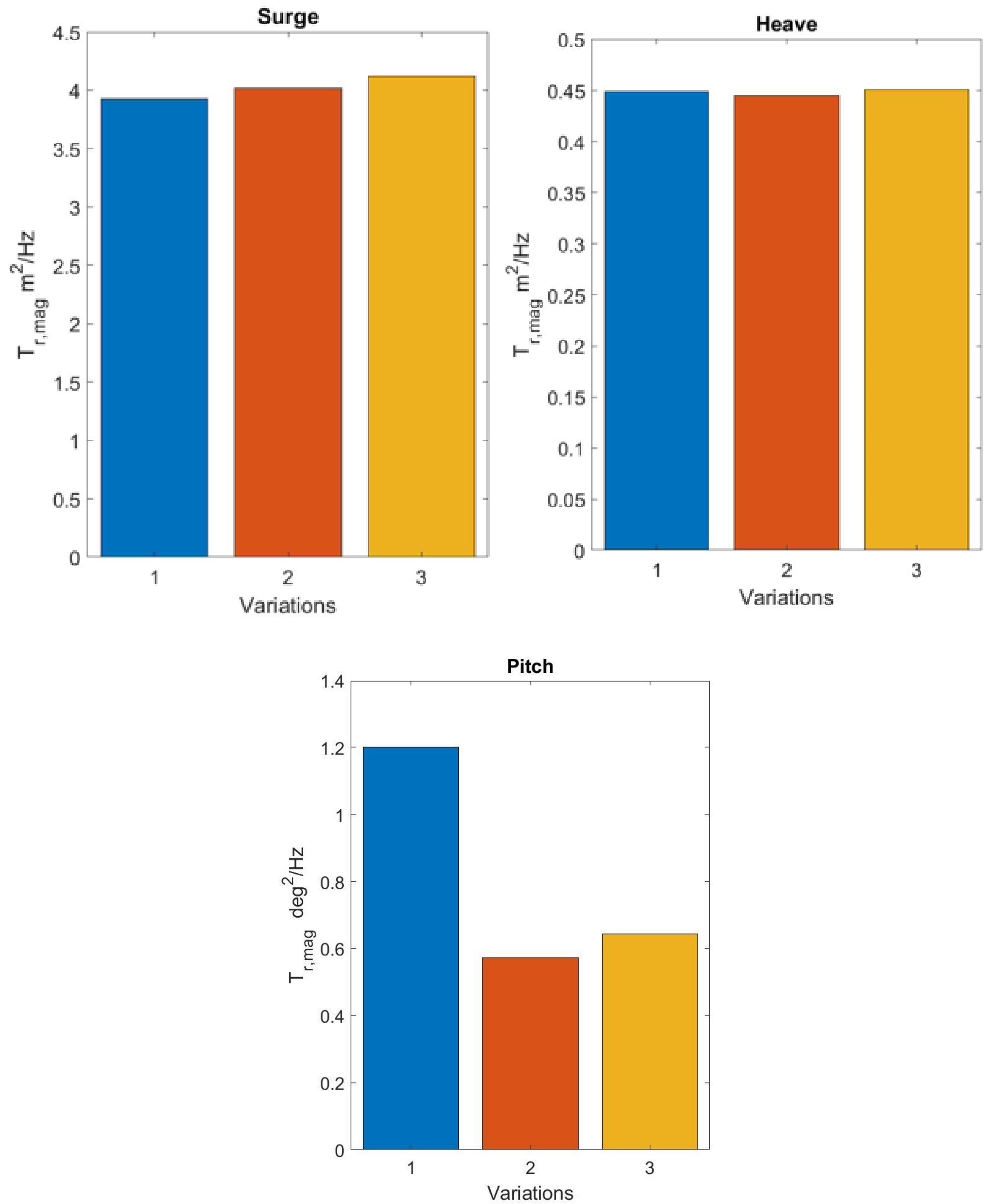

Figure 53 – Variations in $T_{r,\,mag}$ *for variation in inertia surge, heave, and pitch for model A.*

There was a 52% decrease in $T_{r,\,mag}$ for pitch between *V1* and *V2*. However, there was a 12% increase in the pitch response from *V2* to variation *V3* despite a further 1.4% decrease in the KG_Z and a further 3.6% decrease in I_{yy}. It is possible that the wave excitation force changed due to a change in the resonance period. According to Equation 22, the total wave force on a floating system is the sum of the excitation, radiation, and hydrostatic forces. A change in the resonance period could have changed the radiation force from the model and thus the magnitude of platform response.

The magnitude of heave response was not significantly affected by the change in inertia and CoG. All changes conducted were based on desired changes in I_{yy} and CoG_z. However, when changing these values, the inertia of the system about the other axes changed too. The heave inertia, I_{zz}, did change for the variations too. The value of I_{zz} for *V2* was 0.4% bigger than *V1*, and I_{zz} for *V3* was 0.3% smaller than *V1*. While I_{zz} did not significantly affect T_r, the magnitude of heave response, $T_{r,\,mag}$ changed slightly. $T_{r,\,mag}$ decreased by 0.8% between *V1* and *V2* due to an increase in I_{zz}. The decrease in I_{zz} between *V1* and *V3* increased $T_{r,\,mag}$ by 0.4%. The magnitude of the changes are small. However, in spite of this, it is clear that I_{zz} influences the magnitude of surge response to a greater extent than the period of resonant response.

The changes in I_{xx} did not have a significant influence on T_r or $T_{r,mag}$ for surge . The 13.9% decrease in I_{xx} for *V2* had the effect of increasing $T_{r,\,mag}$ by 2.3%. A further 3.3% decrease in I_{xx} resulted in a further 2.6% increase in $T_{r,\,mag}$. The large changes in inertia resulted in relatively small changes in the magnitude of surge response. This suggest that the stiffness of the floating system dictates the magnitude of surge response.

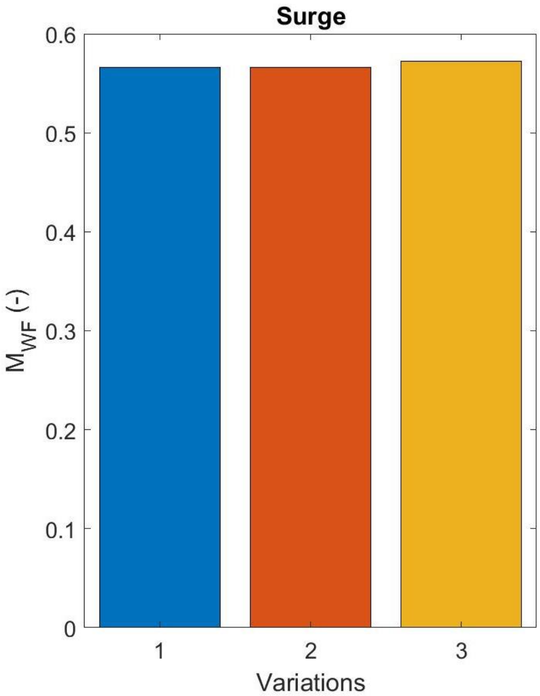

Figure 54 – Change in surge M_{WF} of model A with changes in inertia.

Figure 54 suggests that the uncertainties have less of an impact on surge response in the wave-frequency range. The effects of the variations appear to be amplified at resonance. M_{WF} for *V2* is very similar to M_{WF} for *V1*. M_{WF} for *V3* is 1% larger than for *V1*. The changes in inertia had minimal effect in the wave frequency range. Table 25 and Table 26 below summarise all the changes in results for the inertia and CoG variations.

Variation	Wind System	T_r Surge (s)	T_r Heave (s)	T_r Pitch (s)	$T_{r, mag}$ Surge (m^2/Hz)	$T_{r, mag}$ Heave (m^2/Hz)	$T_{r, mag}$ Pitch (deg^2/Hz)	M_{WF} Surge (-)	M_{WF} Heave (-)	M_{WF} Pitch (deg/m)
1	Thruster Ifremer	163.29	20.85	26.58	3.93	0.45	1.20	0.57	0.61	0.76
2	Thruster Ifremer	163.08	20.99	23.72	4.02	0.45	0.57	0.57	0.61	0.58
3	Thruster Ifremer	162.43	21.01	22.29	4.12	0.45	0.64	0.57	0.61	0.62

Table 25 – Values for metrics for V1, V2, and V3.

Variation	Wind System	T_r Surge (%)	T_r Heave (%)	T_r Pitch (%)	$T_{r, mag}$ Surge (%)	$T_{r, mag}$ Heave (%)	$T_{r, mag}$ Pitch (%)	M_{WF} Surge (%)	M_{WF} Heave (%)	M_{WF} Pitch (%)
1	Thruster Ifremer	-	-	-	-	-	-	-	-	-
2	Thruster Ifremer	-0.13	0.66	-10.77	2.30	-0.82	-52.32	-0.003	0.31	-23.69
3	Thruster Ifremer	-0.53	0.12	-6.02	2.55	1.18	12.35	1.02	-0.26	6.99

Table 26 - % change in V1, V2, and V3 relative to the base case, V1.

4.2.2 Model B

The inertia was adjusted for model B as well as for model A. For model A the inertia and CoG were iteratively decreased. For model B, *V10*, an initial decrease in both the inertia about the y-axis, I_{yy}, and the distance from the keel of the platform to the CoG, KG_z, was completed by moving all of the masses from the top of the tower and the masses within the tower to the outer columns of the platform. For *V11*, no more masses could be removed from the top of the tower. As a result, the x and y inertias and KG_Z could not be decreased further. For this reason, some masses were taken from the outer columns and placed back at the top of the tower. This increased the inertia and CoG of the platform. The exact changes for each variation are shown in Table 27 below.

Variation	Wind System	% change in k relative to base case	% change in I_{xx} relative to base case	% change in I_{yy} relative to base case	% change in I_{zz} relative to base case	% Change in KG_Z relative to base case
9	SiL	-	-	-	-	-
10	SiL	-	-8.46	-8.46	2.35	-9.87
11	SiL	-	-4.01	-4.01	-3.53	-5.61

Table 27 - Model Property changes for V9, V10, and V11 relative to the base case, variation 9.

Changes in I_{yy} and CoG_z were expected to influence model B in a similar manner to model A. Consequently, the changes made in *V10* and *V11* were not expected to affect surge and heave T_r values significantly.

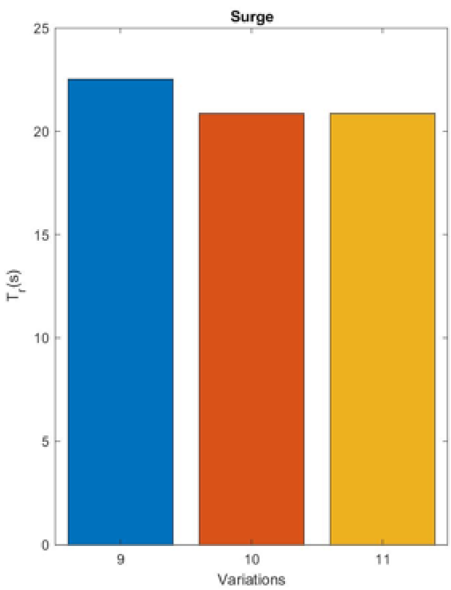

Figure 55 - Change in surge T_r with changes in inertia for model B

Unlike model A, the changes in inertia appeared to influence the surge resonance period of the platform. This was unexpected because neither the mass, hydrostatic stiffness or mooring stiffness were supposed to have changed with the variations conducted. The reduction in surge with the reduction in I_{yy} and increase in GM_L (decrease in KG_Z) would suggest a change in configuration that was not accounted for during the testing campaign. It is unclear what caused this 7.4% decrease in the surge period. While the value of I_{xx} did change by the same magnitude as I_{yy} for each of these variations, it was established for model A that changes in I_{xx} do not significantly affect T_r for surge. Also, the value of T_r only changed between *V9* and *V10* and not between *V10* and *V11*. This further suggests that something other than the inertia caused this change in T_r. Had this anomaly been flagged during the testing campaign, the tests would have been re-run to establish a potential cause for the change in T_r. Unfortunately, it was not possible to place the model back into the tank at the time of analysis.

Like with model A, the variations in inertia and CoG had a minimal effect on the heave T_r. This was not surprising. No change in the heave response period was expected for the reasons stated above with reference to model A.

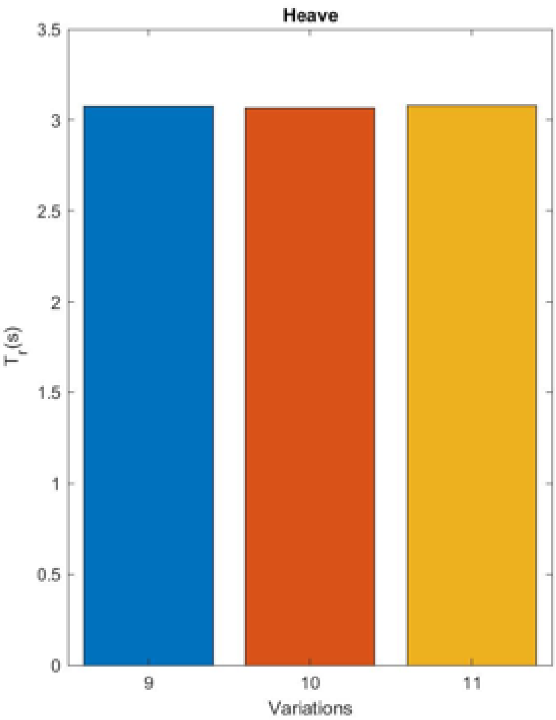

Figure 56 - Change in heave T_r with changes in inertia for model B.

Unlike model A, the changes in inertia and CoG did not significantly influence the pitch resonance period. The plot in Figure 57 below indicates minimal deviation between *V9*, *V10*, and *V11*.

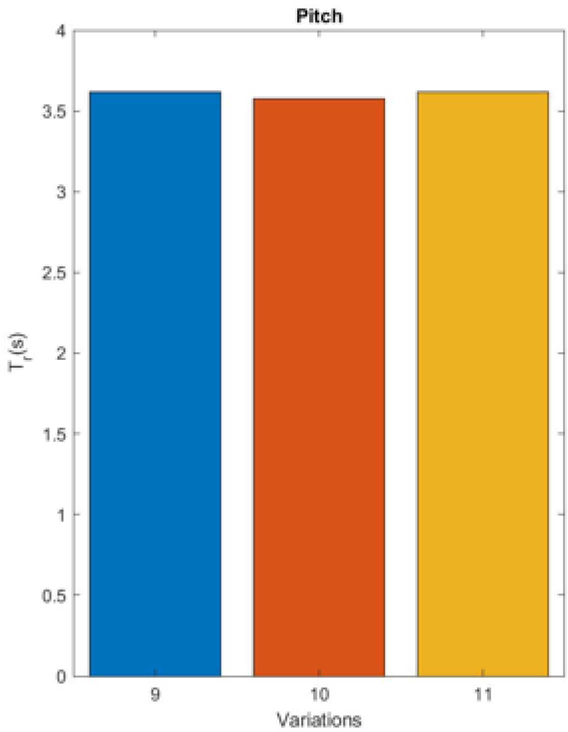

Figure 57 – Change in pitch T_r with changes in inertia for model B.

This was not an expected outcome of the tests as the platform pitch was highly irregular due to the presence of more than one rigid body. The presence of the extra rigid body meant that the pitch motion of model B did not behave like in model A. By comparing the pitch decay tests of model A and model B, shown below in Figure 58, it becomes clear that model B did not pitch like a single rigid body system. The body that was tracked was the upper body; as the upper body pitched, there was no data to show the motion of the lower body. Pitch in the tracked upper body was not always the same and did not always mean that the lower body was also pitching. The motion of each body was influenced by the other.

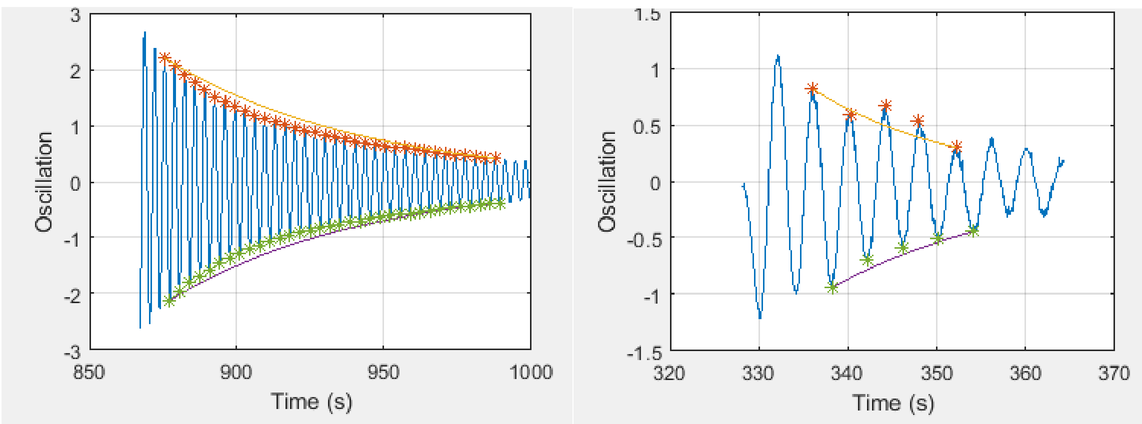

Figure 58 – Model A pitch decay test (left) vs model B pitch decay test (right).

The oscillations for model A are a lot purer, and the amplitude of each oscillation decreases with each oscillation. On the other hand, the amplitudes of model B do not decrease with each oscillation. This is because the motion of each rigid body influences the motion of the other and the platform as a whole.

The changes in inertia had a significant impact on $T_{r,\,mag}$ for model B. However, it is a lot more challenging to pinpoint an exact reason for the changes in $T_{r,\,mag}$ for each variation for model B than for model A. As mentioned above, model B has two rigid bodies; the interaction between the two bodies makes the effect of changes in model properties difficult to predict and understand.

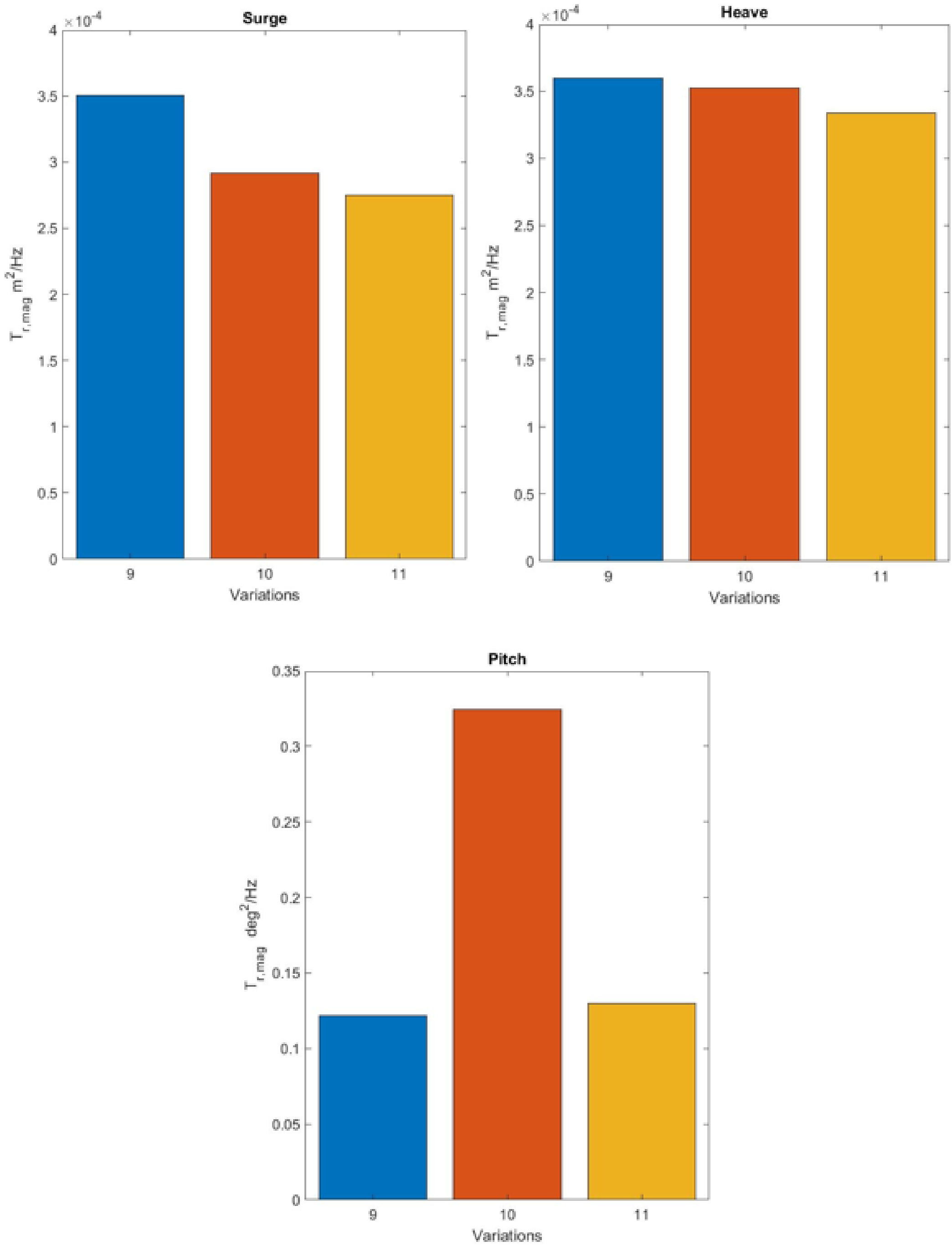

Figure 59 – Change in $T_{r,\,mag}$ in surge, heave, and pitch with changes in inertia for model B.

Heave should not have been significantly affected by the presence of two rigid bodies. As such, it has been assumed that model B heaves like a single rigid body system. The overall value of I_{zz} increased by 2.4% for *V10* and decreased by 3.5% for *V11*, and both adjustments are taken relative to the base case, *V9*. The model did not behave as expected. The exact cause of the steady decrease in $T_{r,\,mag}$ for heave is unknown.

The change in $T_{r,\ mag}$ between *V9* and *V10* for surge had to be discounted for model B. This is because of the anomaly that caused the resonance period of the platform to change inexplicably for these same inertia variations. It has been assumed that this anomaly would then have had an effect on the magnitude of platform responses also. As mentioned above, the platform design meant that the body motions were complicated by the presence of two rigid bodies. For this reason, the response in surge and pitch for model B is different to the response for model A. The influence of the submerged rigid body could not be quantified for this set of experiments. In surge, $T_{r,\ mag}$ decreased by 5.7% for a 4.4% increase in I_{xx}. According to Equation 59, the magnitude of platform response and the inertia are inversely proportional. The results obtained from this variation validate that.

It has already been established that model B does not pitch in the same manner as model A. This is due to the presence of more than one rigid body. Significant changes in the value of $T_{r,\ mag}$ for pitch were observed for each variation. An initial increase of 166% between variations 9 and 10 was observed for $T_{r,\ mag}$ for pitch. A change of this magnitude was for just an 8.4% decrease in I_{yy} and a 9.8% decrease in KG_z. It is possible that the anomaly that was first seen in the value of T_r for surge could have influenced this result. Other than that, there is no known explanation for the dramatic increase in the magnitude of resonance response for pitch. Given such a drastic increase between *V9* and *V10*, the results for pitch have been discounted for this variation. A summary of the effect that each variation had on the metrics is shown below in Table 28 and Table 29.

Variation	Wind System	T_r Surge (s)	T_r Heave (s)	T_r Pitch (s)	$T_{r,\ mag}$ Surge (m^2/Hz)	$T_{r,\ mag}$ Heave (m^2/Hz)	$T_{r,\ mag}$ Pitch (deg^2/Hz)	M_{WF} Surge (-)	M_{WF} Heave (-)	M_{WF} Pitch (deg/m)
9	SiL	22.51	3.07	3.62	0.0004	0.0004	0.12	0.76	0.88	20.96
10	SiL	20.86	3.07	3.57	0.0003	0.0004	0.32	0.83	0.87	28.01
11	SiL	20.84	3.08	3.62	0.0003	0.0003	0.13	0.76	0.86	20.80

Table 28 - Values for metrics for V9, V10, and V11.

Variation	Wind System	T_r Surge (%)	T_r Heave (%)	T_r Pitch (%)	$T_{r, mag}$ Surge (%)	$T_{r, mag}$ Heave (%)	$T_{r, mag}$ Pitch (%)	M_{WF} Surge (%)	M_{WF} Heave (%)	M_{WF} Pitch (%)
9	SiL	-	-	-	-	-	-	-	-	-
10	SiL	-7.34	-0.25	-1.17	-16.73	-2.09	166.21	9.35	-0.98	33.68
11	SiL	-7.40	0.18	0.001	-21.49	-7.21	6.71	0.41	-1.99	-0.74

Table 29 - % change in metrics for V9, V10 and V11 relative to the base case, V9.

4.3 Effect of wind emulation system on platform motions

Difficulties scaling wind turbine properties and creating non-turbulent wind in a confined indoor wave tank testing environment have led to the use of wind emulation systems to emulate wind forces for testing of FOWTs (MaRINET1, 2015).(MaRINET1, 2015). Where scaled-down turbines aim to emulate as many physical properties of the turbine as possible at model scale, wind emulation systems aim to emulate the aerodynamic forces at model scale correctly.

4.3.1 Model A

For model A, a comparison was made between a thruster provided by ifremer and a weighted pulley system. Both systems emulate the thrust forces in the x-direction. In theory, the two results should be similar to one another. However, mixed conclusions have been drawn from studies where the weighted pulley system has been used. One paper deemed it an acceptable method of wind emulation, and another stated it was an over-simplification and does not accurately emulate thrust forces (MaRINET1, 2015; Matha et al., 2015). The weighted pulley system is low-cost and simple to install. For that reason, it would be beneficial to determine whether the system is an effective wind emulation system. This is done by comparing the pulley system described in 3.10.3 and the thruster described in 3.2.1.

The two systems are compared using M_{WF}, T_r, and $T_{r, mag}$. The two systems are also compared through a visual comparison between the decay tests. The pulley system did not have a significant influence on the resonance periods of the platform. The values of T_r for surge, heave, and pitch all changed by less than 0.6% between *V1* and *V4*. This suggested that the model properties, like CoG, Inertia and hydrostatic stiffness, were not affected by the change in wind emulation system.

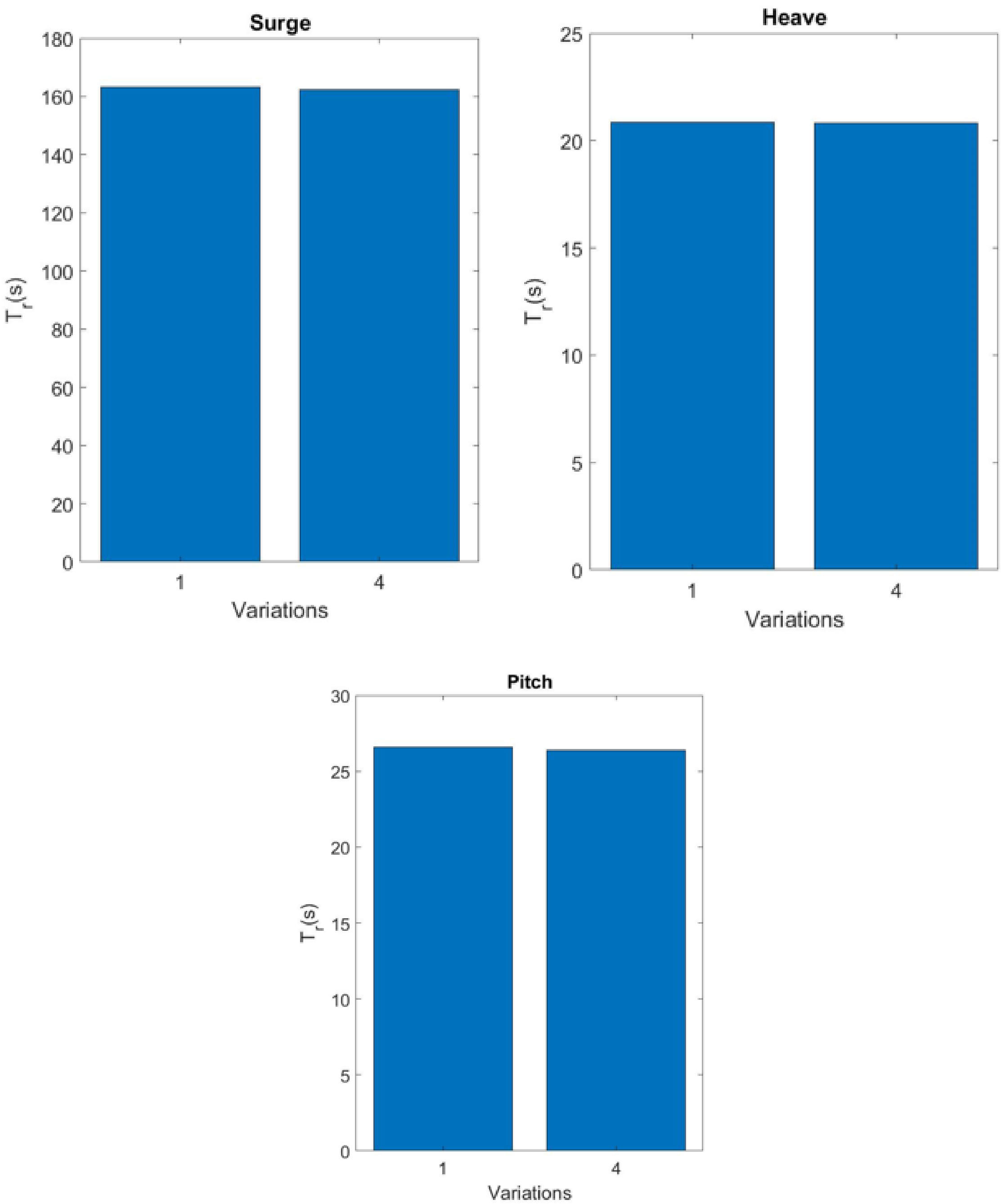

Figure 60 -Thruster system vs Pulley system effect on T_r in surge, heave, and pitch.

The use of the pulley system did significantly affect the magnitude of the surge and pitch responses. However, the magnitude of heave response was not significantly affected. The comparison between the magnitude of resonance response for the three main motions of interest is shown in Figure 61.

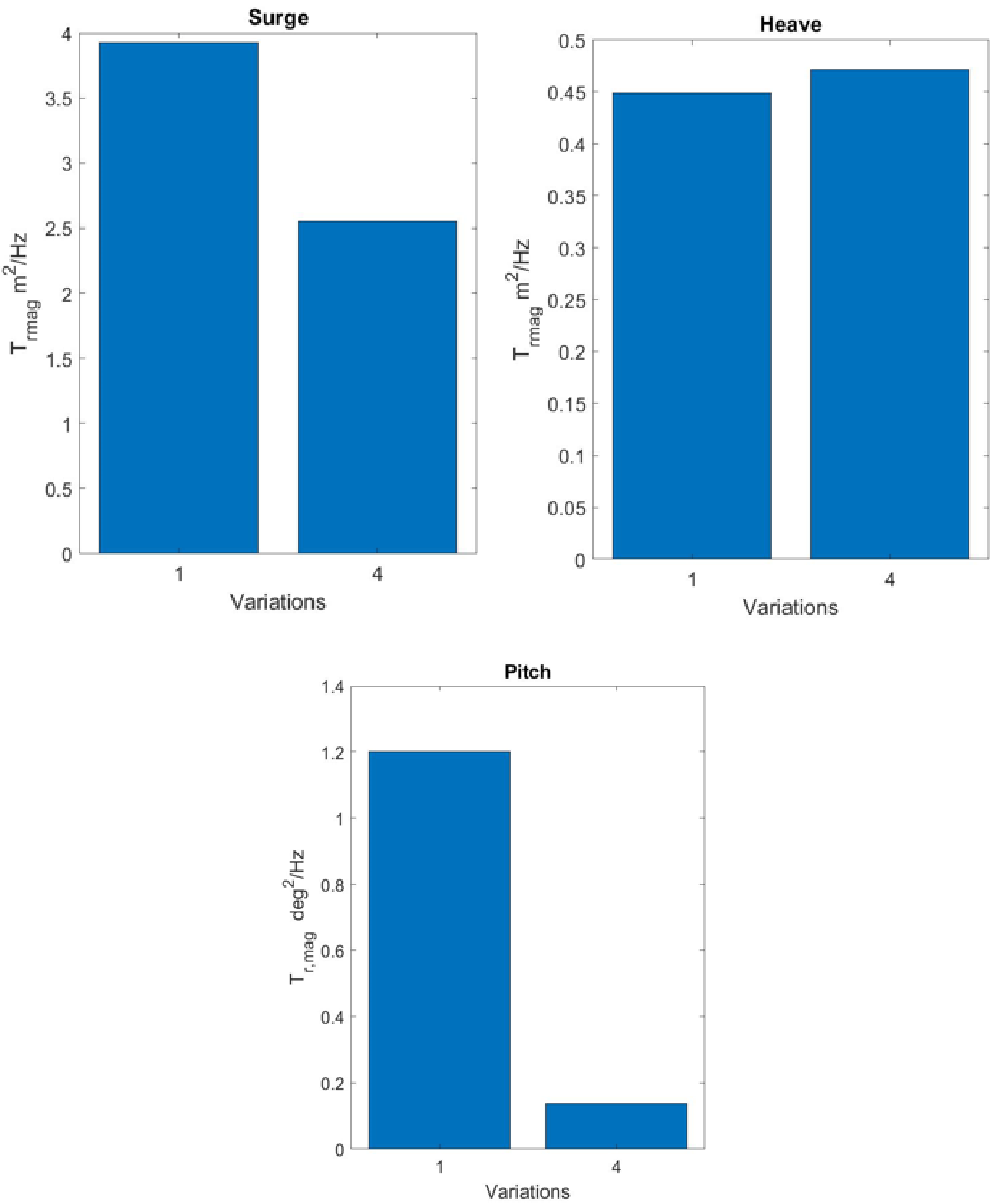

Figure 61 -Thruster system vs Pulley system effect on $T_{r,\,mag}$ in surge, heave, and pitch.

The magnitude of surge and pitch responses with the pulley were far smaller compared to the thruster system. $T_{r,\,mag}$ in surge was reduced by 35%, and there were several reasons for this. One such reason was the friction of the line over the pulley; friction reduced the realised thrust force applied to the top of the tower, thus limiting the surge response. Another reason for the reduced surge response was the motion of the mass attached to the pulley. The mass should move vertically up and down, but in practice, when the mass on the pulley was initially brought through a large motion, like at resonance, it tended not to move up and down. Instead, the mass moved side to side or with a circular movement and this further reduced the force applied at the top of the tower, reducing the surge response.

The pulley system did not correctly estimate the pitch response of the platform. The magnitude of pitch response was 89% smaller with the pulley than with the thruster. With the thruster, the thrust was always applied perpendicularly to the angle of the tower. This meant that the angle of thrust varied depending on platform pitch. With the pulley system, this was not the case. The weighted pulley always applied a horizontal, or very close to horizontal, force to the tower. The tension in the line, the angle at which the force was applied from the line and the irregular motion of the mass attached to the pulley prevented the platform from pitching towards the beach. The friction of the pulley prevented the platform from pitching towards the paddles. The combination of all of these effects resulted in severely reduced pitch motions.

Comparisons between M_{WF} values for each metric clarifies beyond doubt that the pulley system has the effect of damping down the platform motions in the wave frequency range.

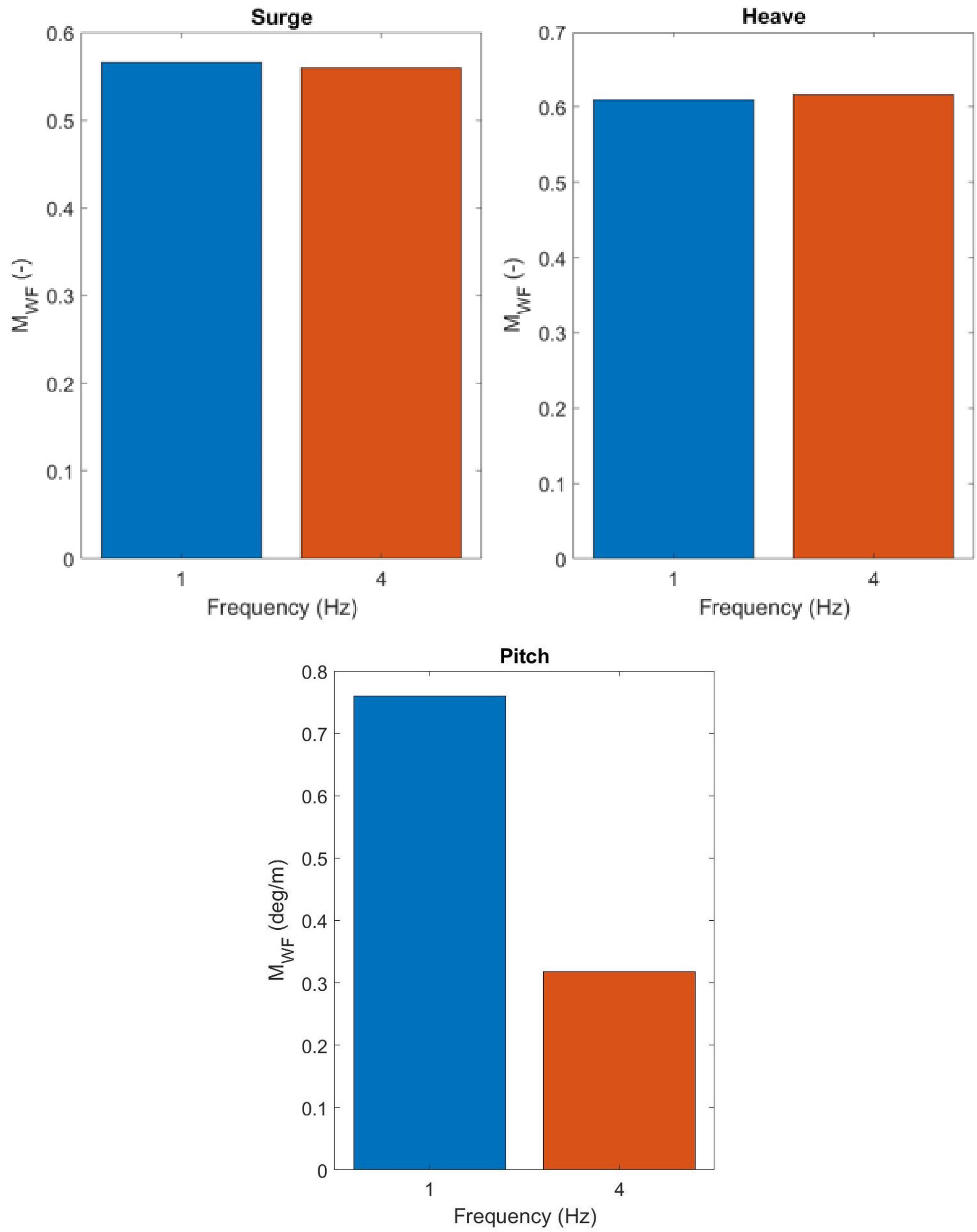

Figure 62 – Thruster system vs Pulley system effect on M_{WF} in surge, heave, and pitch.

The charts shown in Figure 62 indicates that the pulley system affected each platform motion differently. The pulley system has the most significant influence on the pitch motion of the system in the wave frequency range. When comparing *V1* and *V4*, the magnitude of M_{WF} decreases by 58%. The influence on surge and heave is far less, with their M_{WF} values increasing and decreasing by 1%, respectively. The pulley system was not expected to influence the magnitude of heave. The pulley system provided little to no resistance to the platform heave and did not significantly impact surge responses in the wave-frequency range. Factors limiting the surge, like the motion of the mass and the friction of the spring, are likely amplified at resonance. As surge is a low-frequency response, the effect of the pulley on the platform motions at resonance will not influence M_{WF} because M_{WF} indicates what is happening in the wave-frequency range.

The pulley system had a significant influence on the other platform motions and on mooring responses.

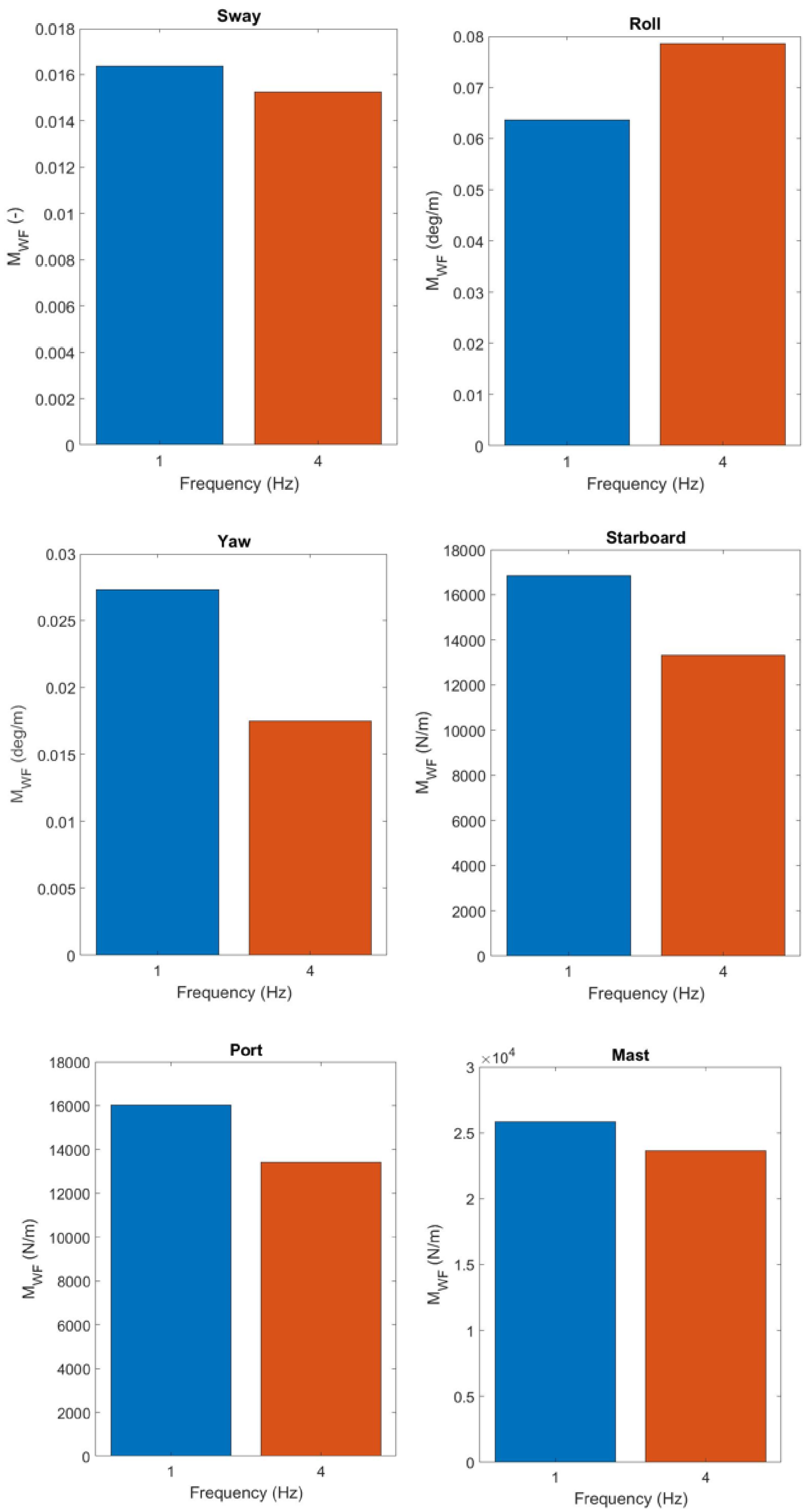

Figure 63 – Thruster vs Pulley system effect on M_{WF} for sway, roll, yaw, and mooring responses.

All motions and mooring responses other than roll had a significant decrease in M_{WF} when comparing *V4* with variation *V1*. The increased roll may be a consequence of the decreased pitch motion. During testing, it was observed that when wave forces caused the platform to pitch, and the pulley limited the pitch, platform roll was induced.

The effect of the pulley system is clear from the comparison shown. It was clear that the pulley system dampened the platform motions during testing. While testing allowed for a detailed comparison between the two wind emulation systems, the effect of the pulley system was apparent prior to running any waves at the platform. When conducting decay tests on the platform with the pulley system in place, the shortcomings of the pulley system became quite clear. When conducting surge and pitch decays tests with the thruster switched on, multiple oscillations could be recorded for each test. However, with the pulley system, there were fewer usable oscillations for analysis, and the oscillations were not as pure as with the thruster. The plots shown in Figure 64 below show the surge decay tests with the pulley and the thruster with an oscillation of a similar magnitude. The first oscillation used for each decay test was not the initial forced oscillation but the subsequent oscillation. The decay test with the pulley attached dampens down far quicker than the decay test with the thruster.

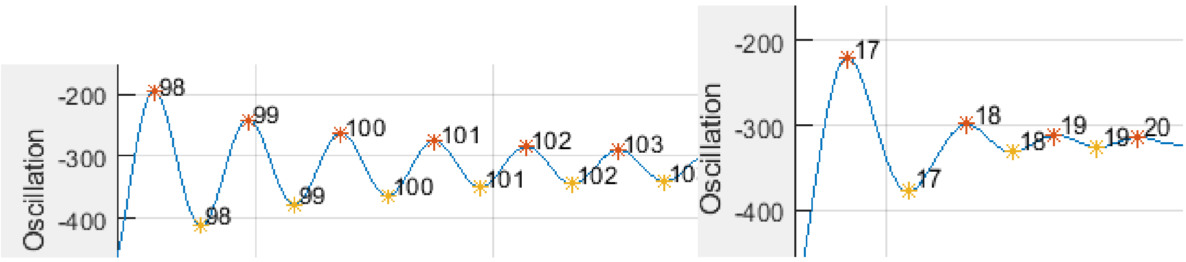

Figure 64 – Surge decay tests for thruster (above) and pulley (below) model A.

During the pitch free decay test, shown in Figure 65, the pitch motion was dampened down even more than the surge free decay tests. With the thruster, up to forty oscillations could have been recorded for each decay test if that was deemed necessary. In the plot shown below, the decay test was stopped after 16 oscillations. With the pulley system, no more than two full oscillations were recorded before the pitch motions were dampened down completely.

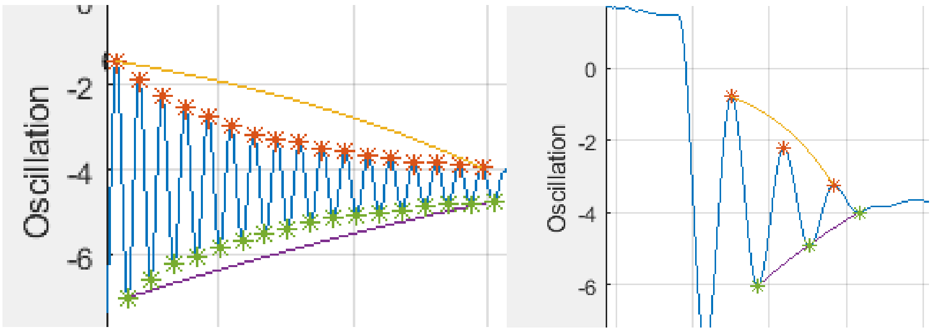

Figure 65 – Pitch decay tests with the thruster (left) and the pulley (right) for model A.

The pulley system did not significantly affect the heave decay tests. The effect that the variation in the wind emulation system had on the metrics for model A are summarised below in Table 30 and Table 31.

Variation	Wind System	T_r Surge (s)	T_r Heave (s)	T_r Pitch (s)	$T_{r,\,mag}$ Surge (m^2/Hz)	$T_{r,\,mag}$ Heave (m^2/Hz)	$T_{r,\,mag}$ Pitch (deg^2/Hz)	M_{WF} Surge (-)	M_{WF} Heave (-)	M_{WF} Pitch (deg/m)
1	Thruster Ifremer	163.29	20.85	26.58	3.93	0.45	1.20	0.57	0.61	0.76
4	Pulley	162.29	20.83	26.41	2.55	0.47	0.14	0.56	0.62	0.32

Table 30 – Summary of values for metrics for V1 and V4

Variation	Wind System	T_r Surge (%)	T_r Heave (%)	T_r Pitch (%)	$T_{r,\,mag}$ Surge (%)	$T_{r,\,mag}$ Heave (%)	$T_{r,\,mag}$ Pitch (%)	M_{WF} Surge (%)	M_{WF} Heave (%)	M_{WF} Pitch (%)
1	Thruster Ifremer	-	-	-	-	-	-	-	-	-
4	Pulley	-0.61	-0.12	-0.65	-35.01	4.89	-88.53	-1.09	1.10	-58.22

Table 31 - % change in metrics for V1 and V4 relative to the base case, V1.

4.3.2 Model B

Model B was used to compare the SiL wind emulation system and a standard thruster. The differences between the SiL system and the thruster have been described above. The most notable differences are that SiL emulates more than just wind thrust, and all of the aerodynamic forces are altered constantly throughout each test, depending on the platform motions. Figure 66 below shows how the thrust delivered by the SiL system varies with time depending on the platform motion, whereas the thrust produced by the thruster is constant throughout testing.

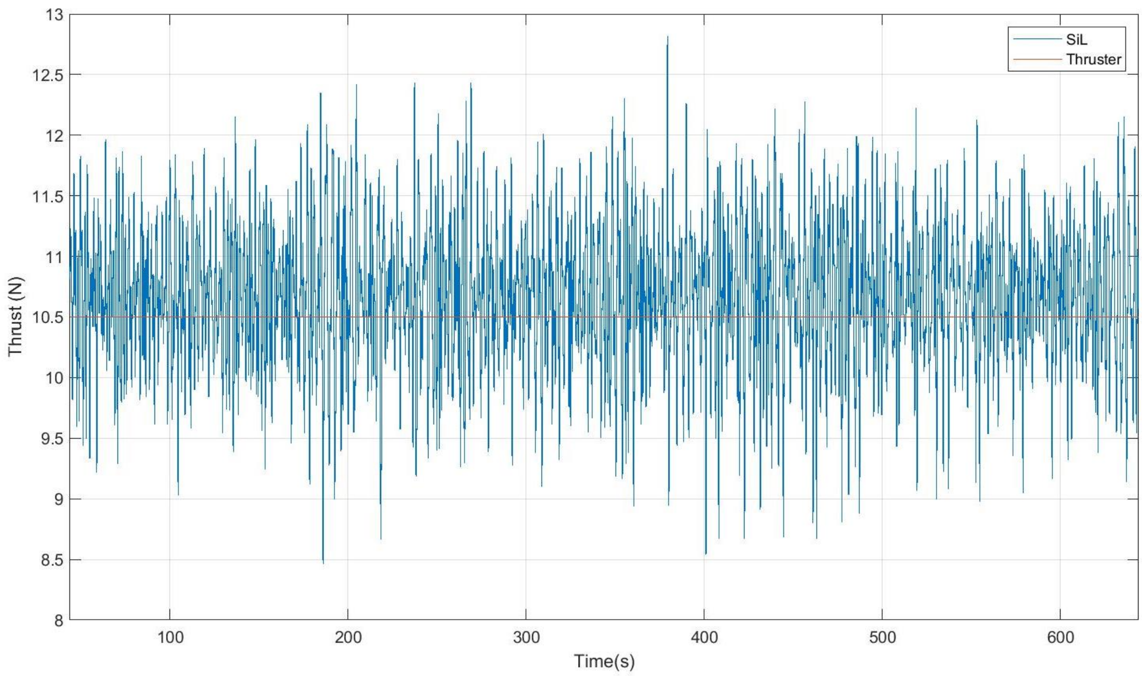

Figure 66 – Variation in thrust for test 001 with SIL vs constant thrust force for all tests in V12.

There were differences between the resonance periods of the platform responses in surge and pitch, while the heave resonance period remained largely unchanged.

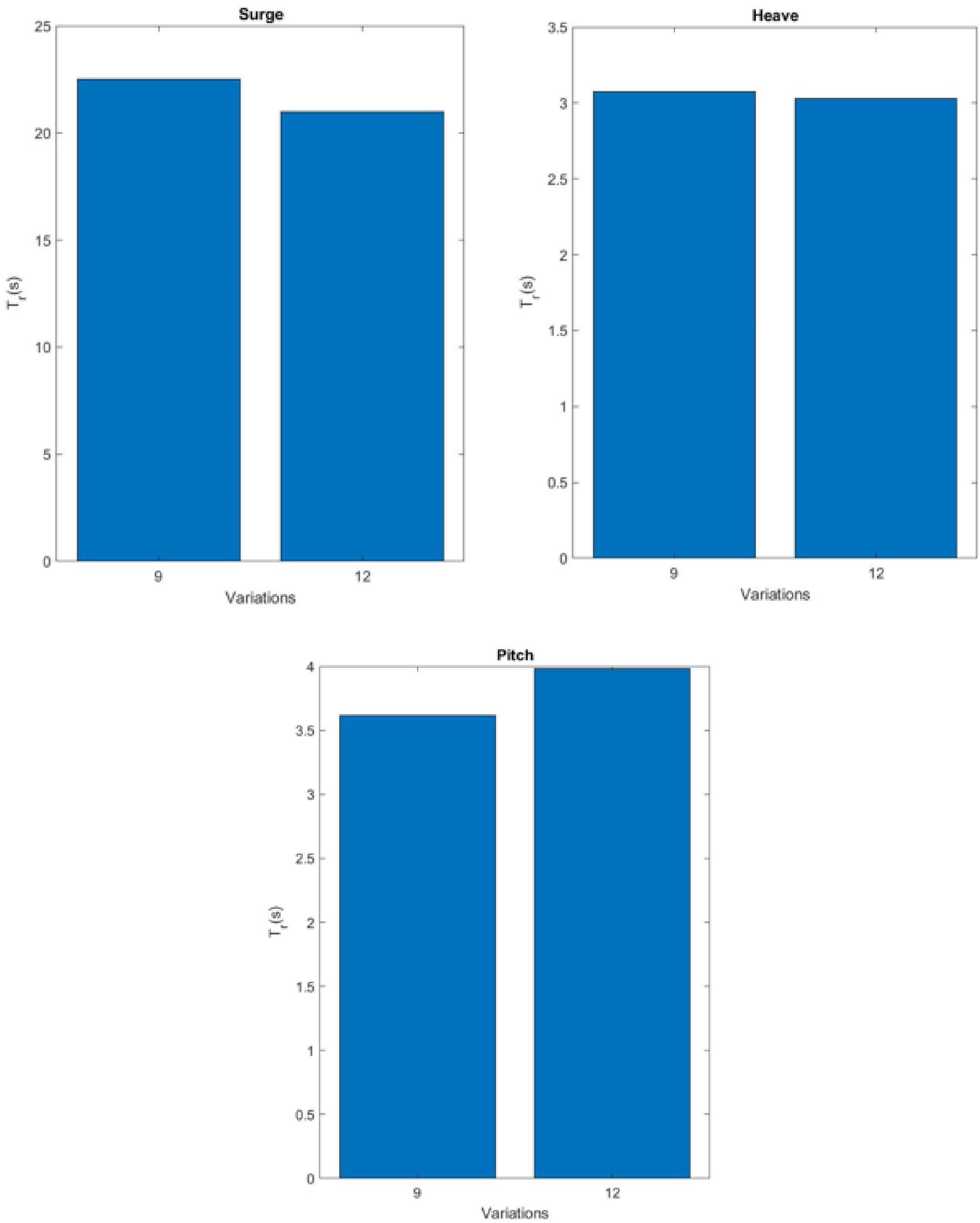

Figure 67 - Effect of change of wind emulation system on T_r, for model B.

The decrease in T_r for surge is most likely a consequence of the same issue established in Section 4.2.2 when comparing the effect of inertia changes on the platform responses of model B. As stated above, the exact cause of this change is unknown, but it is likely to have been due to a change in the mooring configuration between *V9* and *V10*. The value of T_r for surge decreased by 6.7% between *V9* and *V12*. The heave resonance period was largely unaffected by the change in the wind emulation system. However, the value of T_r for pitch increased by 10% when the thruster was attached. The effect of the thruster on the pitch resonance period is better is explained by comparing the PSDs of both systems.

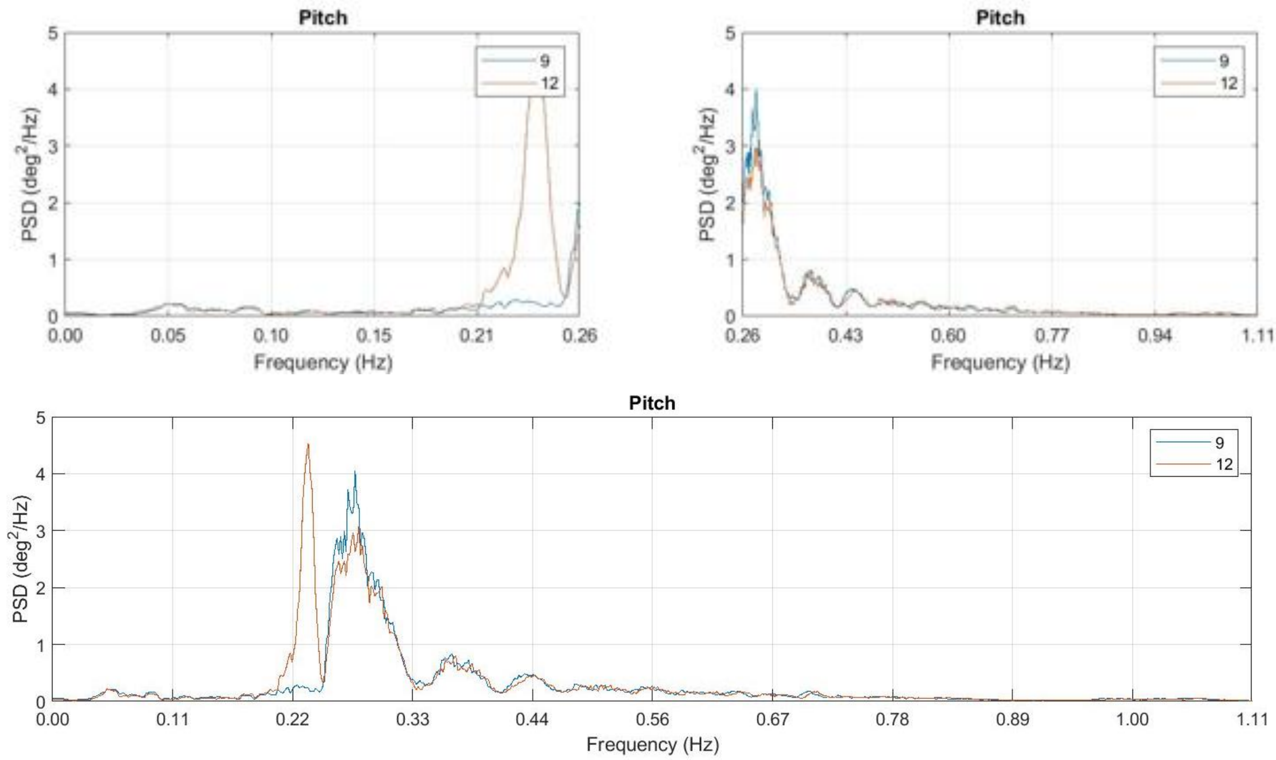

Figure 68 – PSD of model B for V9 and V12.

In *V12*, with the thruster, there is a peak of similar magnitude to *V9* at the same location as T_r for variation 9. However, unlike *V9*, with *V12*, there is a low-frequency resonance peak with a greater magnitude than the other resonance in the wave frequency range and the only resonance peak for *V12*. This low-frequency peak was not a factor in *V10* or *V11* and cannot be attributed unknown factor that caused a decrease in T_r for surge between *V9* and *V10*. This low-frequency peak cannot be accounted for, but it is most likely an architect of model design. The presence of two rigid bodies could have caused this second peak with the thrust only. Given that for model A, with the thruster only, there was no secondary peak, it is likely that this type of peak is unique to the particular design of the model and, in particular, due to the presence of multiple rigid bodies. The exact influence of the SiL versus the thruster cannot be determined exactly without further tests being conducted. A test where the model is under the influence of PN waves only would provide further insight into the exact influence of the SiL on platform responses. Unfortunately, at the time of analysis, this was not possible.

The thrust from the thruster is constant throughout, the SiL does not adjust thrust for low-frequency response, only high-frequency responses. The value of $T_{r,\ mag}$ for pitch was affected by this. The magnitude of pitch response increased by 50%. This increased magnitude is accounted for by both the low-frequency and wave-frequency resonance peaks.

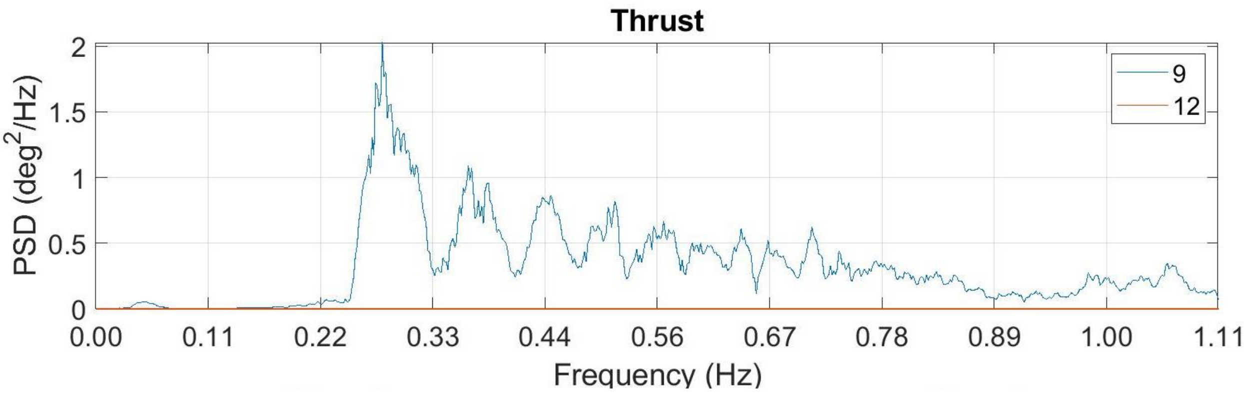

Figure 69 – SiL thrust response to platform motions

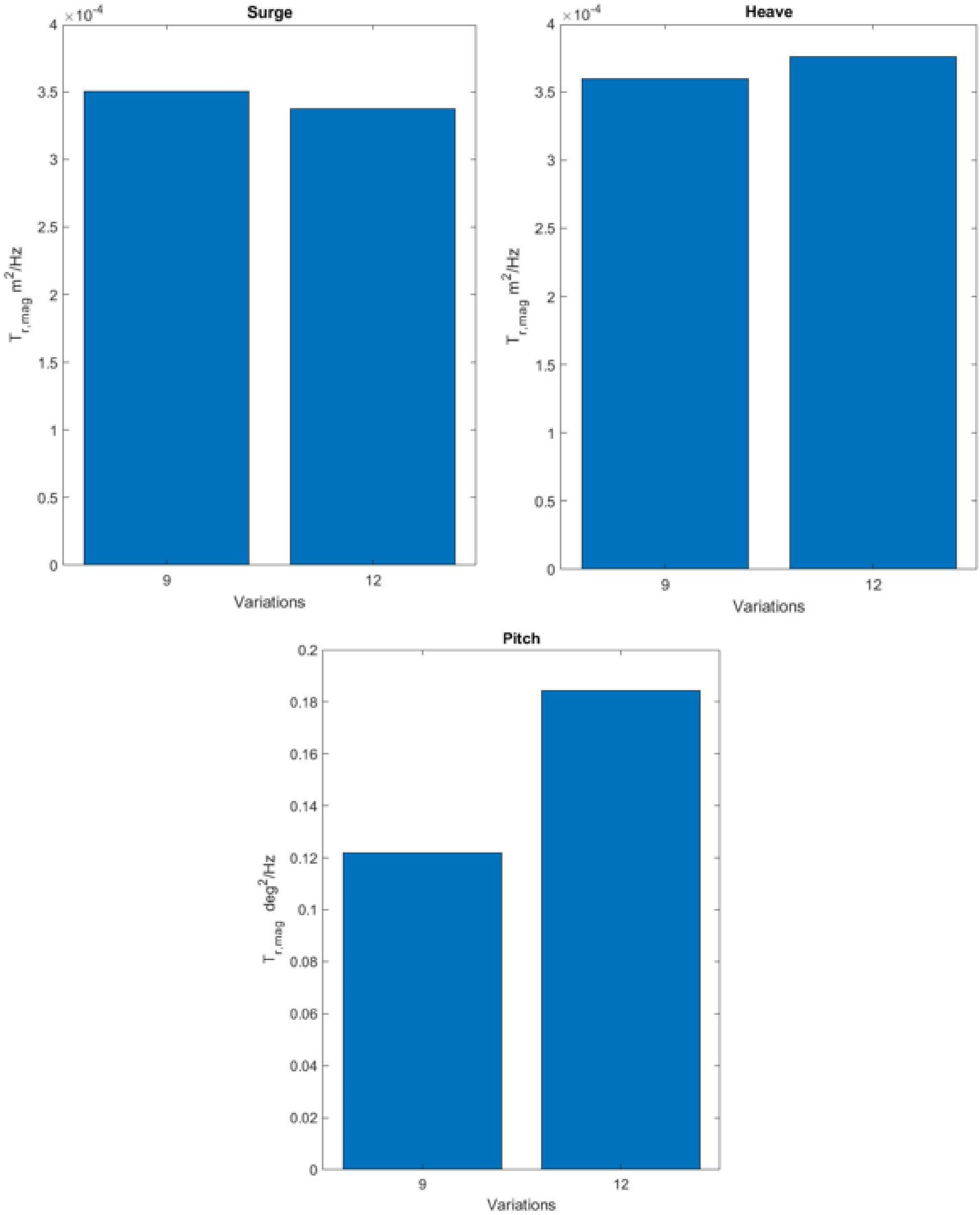

Figure 70 – Effect of change of wind emulation system on $T_{r,\ mag}$ for model B.

The change in the wind emulation system did not significantly affect the values of $T_{r,\ mag}$ for surge and heave. The surge decreased by approximately 3.7%. That would suggest that instantaneous changes in thrust throughout testing provided by SiL had a more significant influence on the pitch of the platform than the surge of the platform. Table 32 and Table 33 below summarise the contrast between the results for each of the metrics using SiL and the MaREI thruster.

Variation	Wind System	T_r Surge (s)	T_r Heave (s)	T_r Pitch (s)	$T_{r,\,mag}$ Surge (m^2/Hz)	$T_{r,\,mag}$ Heave (m^2/Hz)	$T_{r,\,mag}$ Pitch (deg^2/Hz)	M_{WF} Surge (-)	M_{WF} Heave (-)	M_{WF} Pitch (deg/m)
9	SiL	22.51	3.07	3.62	0.0004	0.0004	0.12	0.76	0.88	20.96
12	Thruster MaREI	21.00	3.03	3.98	0.0003	0.0004	0.18	0.76	0.89	20.02

Table 32 - Summary of values for metrics for V9 and V12

Variation	Wind System	T_r Surge (%)	T_r Heave (%)	T_r Pitch (%)	$T_{r,\,mag}$ Surge (%)	$T_{r,\,mag}$ Heave (%)	$T_{r,\,mag}$ Pitch (%)	M_{WF} Surge (%)	M_{WF} Heave (%)	M_{WF} Pitch (%)
9	SiL	-	-	-	-	-	-	-	-	-
12	Thruster MaREI	-6.70	-1.38	10.14	-3.66	4.54	51.22	0.42	1.43	-4.48

Table 33 - % change in metrics for V1 and V4 relative to the base case, V1.

4.4 Influence of mooring system stiffness on platform responses

Uncertainties in mooring line stiffness can arise depending on the method used to hold the model in place. In the case of model A, a linear horizontal mooring system was employed. Linear horizontal mooring systems are not a realistic mooring system. It is rather used to minimise the model's drift while allowing the model to freely move in heave and pitch DoFs. Real mooring systems would take the typical configurations i.e., catenary, taut or vertical (TLP) lines, as discussed in Section 2. Such systems have been adopted for model B. The horizontal mooring system was employed during the MaRINET2 testing campaign and subsequently for this research campaign due to the ease of set-up in the tank. The linear horizontal mooring system allowed mooring properties to be changed easily and quantifiably, and the influence of these changes to be measured. While the mooring system used is not one that will be used in practice, it still allows the influence of mooring line stiffness on model responses to be quantified. The lines themselves were assumed inextensible. As a result, the stiffness of each mooring line was determined by doing load extensions tests on the springs used for testing. The method itself is straightforward. However, the method has an associated level of uncertainty, much like there is with the bifilar and trifilar tests used for inertia calculations and the balance and hang tests used for CoG estimations. The uncertainty associated with the method, along with an explanation that uncertainty was arrived at, is given in Section 3.10.4 and Section 3.10.5. As it transpired, the properties of the springs that arrived in the lab were not as expected. The combination of springs used for *V1*, the initial setup, had a k-value of 45.68kN/m. The springs used in *V7* had an average k-value of 45.38kN/m, just 0.66% less than the original value, not the 3% decrease expected. An increase of 3% was desired for *V8*. The springs used in *V8* had an average k-value of 53.49kN/m, 17.1% greater than the original value. The actual changes in mooring stiffness are summarised below in Table 34.

Variation	Wind System	% change in *k* relative to base case	% change in I_{xx} relative to base case	% change in I_{yy} relative to base case	% change in I_{zz} relative to base case	% Change in KG_Z relative to base case
1	Thruster Ifremer	-	-	-	-	-
7	Thruster Ifremer	-0.7	-	-	-	-
8	Thruster Ifremer	17%	-	-	-	-

Table 34 – Change in mooring stiffness for V1, V7, and V11 relative to the base case, V1.

This allows for an assessment of the effect that errors in spring manufacturing can have on platform motions.

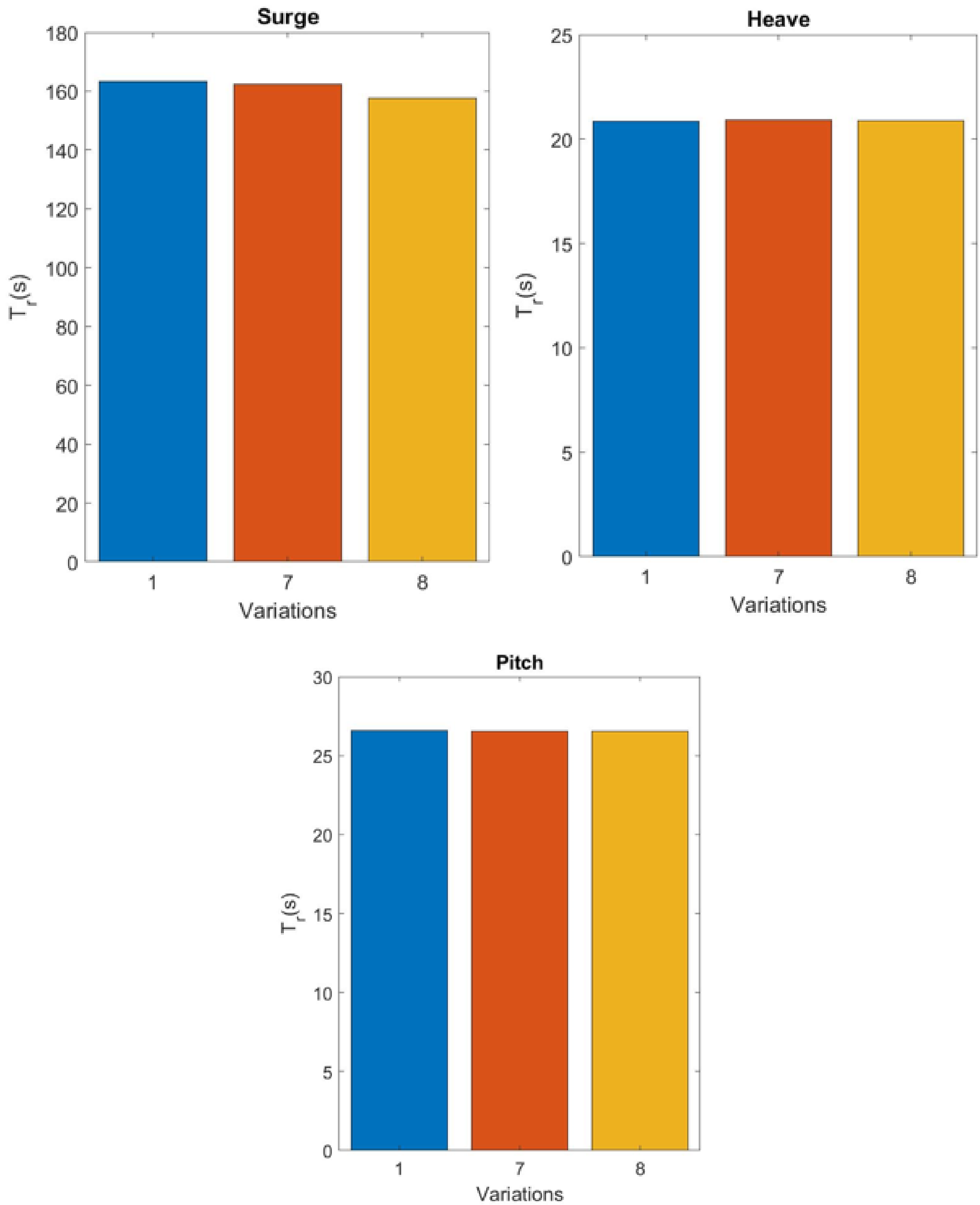

Figure 71 – Variation in T_r with changes in mooring stiffness for surge, heave, and pitch for model A.

The surge resonance period decreased by 0.58% between *V1* and *V7*. It was expected that the resonance period would increase slightly with the decrease in spring stiffness as derived by simple harmonic motion. The main difference between the two springs was that for *V1,* each line had two springs in series, and for *V7,* each line consisted of one solitary spring. The differences between the average value of *k* for *V1* and *V7* was within the uncertainty bounds of the load-displacement test method. For this reason, it is difficult to draw concrete conclusions from this particular comparison. However, it does prove that there is very little difference between the value of T_r for a platform that is moored by two springs in series and a platform that is moored by standalone springs.

The 17% increase in spring stiffness between *V1* and *V8* resulted in a 4% decrease in the period of resonance response for model A. A decrease in T_r was expected, but the extent of the decrease was smaller than anticipated. However, it did not significantly impact the resonance period of the platform. This would suggest that another parameter, such as the hydrostatic stiffness in surge, is the dominant factor for the resonance period for a semi-submersible platform.

The mooring stiffness did not have any significant impact on values of T_r for heave and pitch. T_r decreased by less than 0.14% between *V1* and *V8*. Given the magnitude of the change in mooring stiffness for this variation, the resulting change in T_r is insignificant. The variations in mooring stiffness had a more profound effect on $T_{r,mag}$, in particular for surge.

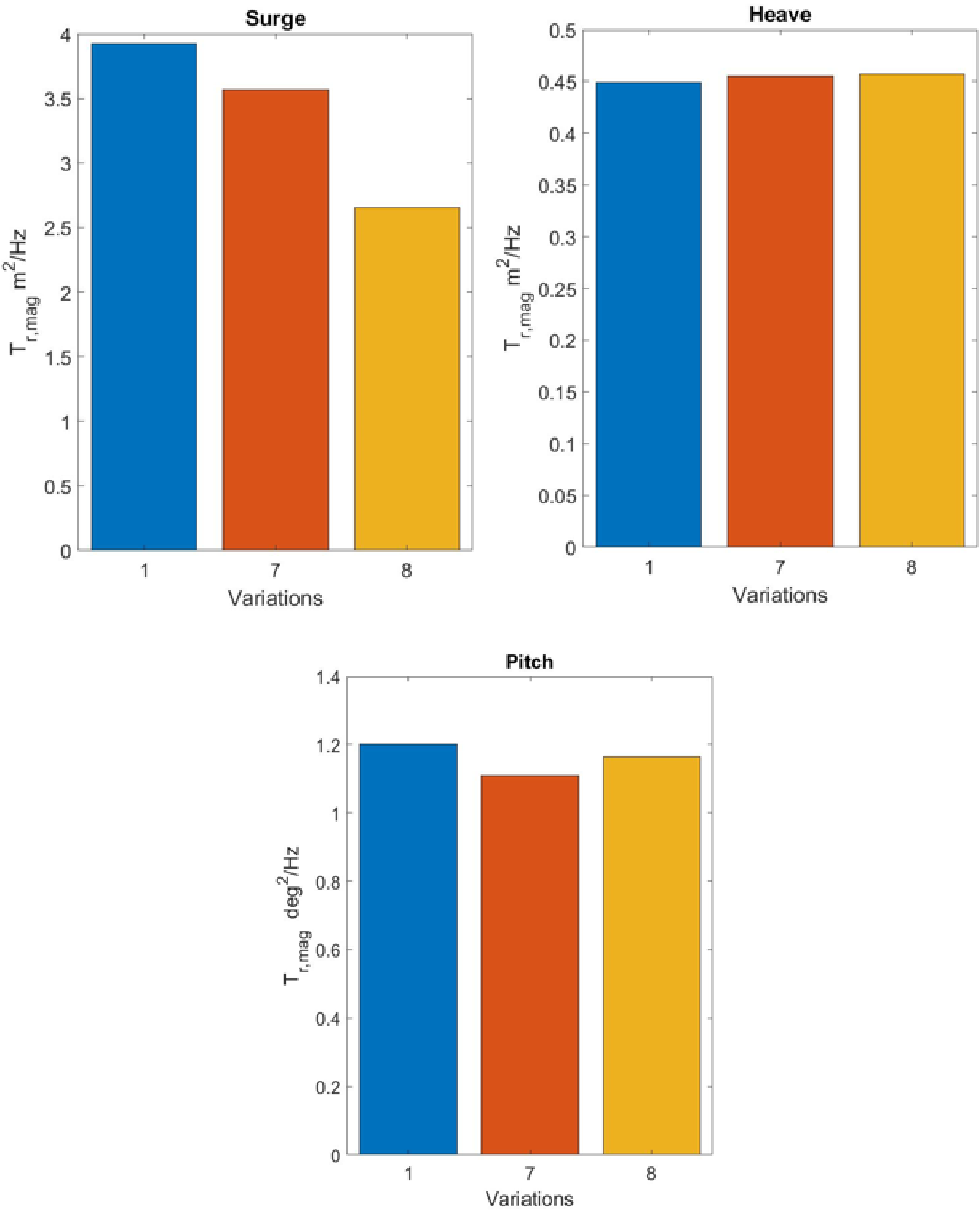

Figure 72 – Variation in $T_{r,\,mag}$ for surge, heave, and pitch with variations in mooring stiffness.

The differences between the values in *V1* and *V7* are interesting. The spring constants for the springs used in the tests were very similar. The only difference between the two mooring systems was that *V1* had two springs in series, whereas *V2* had a standalone spring. Given that the uncertainty in the load-extension method of calibrating the springs is 3%, it cannot be said for definite what the exact difference is between the two springs. The main benefit of the comparison between *V1* and *V7* is that it highlights the effect that a standalone springs vs a spring in series had on the magnitude of platform motions. From the evidence presented in Figure 72, it is clear that the effect of the standalone spring vs the spring in series is greater for $T_{r,\,mag}$ than it is for T_r. $T_{r,\,mag}$ for surge decreased by 9.2% between *V1* and *V7*. For heave, there was an increase of 1.34% and a decrease of 7.6% for pitch. These changes are far larger than the changes in T_r for the same variations.

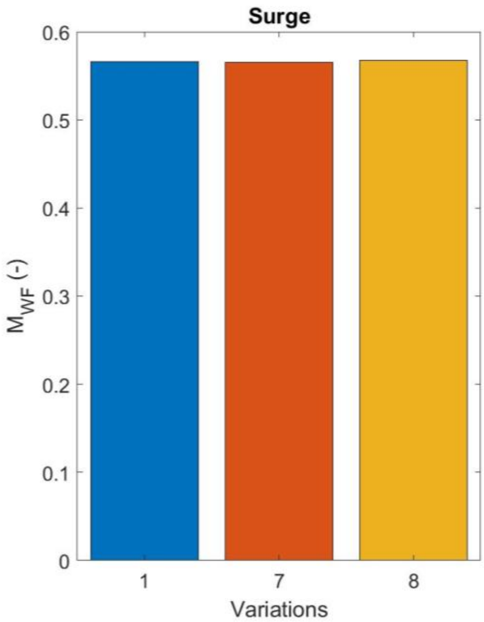

Figure 73 – Effect of variations in mooring stiffness on surge M_{WF} for model A.

Between *V7* and *V8*, the stiffness of each spring was increased by approximately 18%. This change increased $T_{r,\,mag}$ for surge by 25.6%. Given the relationship between stiffness and response shown in Equation 59, a decrease in $T_{r,\,mag}$ was predicted. This comparison highlights the extent of the influence that mooring line stiffness has on the magnitude of resonance response. The effect of the variations in mooring stiffness was amplified at resonance, as was the case with the other variations shown above. The changes in mooring stiffness had no discernible effect on the value of M_{WF} for surge. The magnitude of heave response increased by 0.3% between *V7* and *V8*; this is a minor change. Given that it is a horizontal mooring system, it was not expected that changes in the mooring system would have any effect. If a catenary mooring system were employed, then the outcome of changes in stiffness would perhaps be different. This is because catenary mooring systems have a curved load extension curve, unlike the system investigated during this study, which was linear. Interestingly, $T_{r, mag}$ for pitch increased by 4.9% for the same variation. Much like for heave, it was not expected that a horizontal mooring system would have a significant effect on the magnitude of pitch response. Table 35 and Table 36 below summarise the effect that the variations in mooring stiffness had on each of the metrics. A summary of all of the results from *V1* to *V12* is shown in Appendix 6.3.

Variation	Wind System	T_r Surge (s)	T_r Heave (s)	T_r Pitch (s)	$T_{r, mag}$ Surge (m^2/Hz)	$T_{r, mag}$ Heave (m^2/Hz)	$T_{r, mag}$ Pitch (deg^2/Hz)	M_{WF} Surge (-)	M_{WF} Heave (-)	M_{WF} Pitch (deg/m)
1	Thruster Ifremer	163.29	20.85	26.58	3.93	0.45	1.20	0.57	0.61	0.76
7	Thruster Ifremer	162.35	20.91	26.57	3.57	0.46	1.11	0.57	0.61	0.73
8	Thruster Ifremer	157.59	20.88	26.55	2.65	0.46	1.16	0.57	0.61	0.75

Table 35 – Summary of values for metrics for V1, V7, and V8.

Variation	Wind System	T_r Surge (%)	T_r Heave (%)	T_r Pitch (%)	$T_{r, mag}$ Surge (%)	$T_{r, mag}$ Heave (%)	$T_{r, mag}$ Pitch (%)	M_{WF} Surge (%)	M_{WF} Heave (%)	M_{WF} Pitch (%)
1	Thruster Ifremer	-	-	-	-	-	-	-	-	-
7	Thruster Ifremer	-0.58	0.27	-0.07	-9.21	1.35	-7.60	-0.13	-0.52	-3.80
8	Thruster Ifremer	-3.49	0.13	-0.14	-32.43	1.70	-3.07	0.27	-0.48	-1.58

Table 36 - % change in the metrics for V1, V7, and V8 relative to the base case, V1.

5 Conclusions

5.1 Introduction

Detailed conclusions from each set of variations will first be presented in this section followed by a summary of the overall conclusions from all of the variations conducted.

5.2 Detailed conclusions

5.2.1 Conclusions from variations in model physical properties

- Changes in the physical properties of floating offshore wind platforms influence platform motions. For both model A and model B, changes in the inertia and CoG_z had more influence on the magnitude of resonance response, $T_{r,\ mag}$, than the period of resonance response, T_r.
- Analysing a single rigid body system is far easier than a two rigid body system. It became clear from the analysis that the motions of model B, a two rigid body system, are more complex than a single rigid body system. This is due to the combinations of motions that this model design can cause. The two individual bodies motions are out of phase with one another, and both rigid bodies have their own 6DoF motions; this gives rise to motions not seen in single rigid body platforms. Therefore it was far more challenging to understand the reasons for changes in platform responses for model B than model A. Where double or multiple rigid body systems are used, the motion of each rigid body should be tracked to better understand how the motions of each platform influence the motion of the other.
- The changes in inertia for model A were brought about by moving mass from the top of the tower to the tops of the lower columns of the semi-submersible. While the primary focus of the test was to explore the effect of changes in inertia about the y-axis, I_{yy}, and the distance between the keel of the platform and the CoG, KG_Z, by changing these parameters, the inertia about the x and z axes, I_{xx} and I_{zz}, were affected by default. Theoretical relations derived in Chapter 2 of the report allowed for predictions about the changes these variations would bring about to be made. Despite

large changes in I_{xx} for each variation, there were negligible changes in T_r for surge. This suggested that changes in I_{xx} does not have a signigicant bearing on T_r for surge.

- The variations only caused minor changes in I_{zz}; the changes did not affect the T_r for heave. It was not clear from these tests whether I_{zz} affected T_r significantly. The changes in I_{zz} did appear to affect the magnitude of the resonance response. This could not be stated for definite because the changes in I_{zz} were very small.
- The changes to I_{xx} were of a similar magnitude to the changes to I_{yy} for the variations. The variations in I_{xx} influenced the magnitude of platform response. As I_{xx} decreased, $T_{r,\,mag}$ increased for surge. The variations in I_{yy} and CoG_z had more of an influence on $T_{r,\,mag}$ for pitch than the variations in I_{xx} had for surge.
- Large changes in T_r made it more difficult for $T_{r,\,mag}$ to be predicted as this can change the radiated wave force.
- The effects of the variations in inertia were amplified at resonance. This can be seen by comparing the effect that the changes in inertia had on $T_{r,\,mag}$ vs the effect they had on M_{WF} for surge.
- Given that the designs of most semi-submersible platforms are very similar, the results from the model A variations can be translated to other semi-submersible platforms. It can be concluded that changes in inertia have a more significant effect on the magnitude of platform responses than the period of resonance response, particularly at resonance. Of all the changes in inertia, the changes in I_{yy} had the most significant effect on T_r. This could be because these changes were coupled with changes in CoG_z. That being said, changes in I_{xx} did have a considerable impact on the magnitude of surge response. The fact that changes in I_{xx} did not affect T_r for surge would suggest that other factors such as the hydrostatic stiffness and the mooring stiffness have more of an influence on T_r. The effect of the mooring stiffness will be investigated in Section 4.4 of this report.
- The behaviour of model B was difficult to understand and to analyse. Both rigid bodies had their own 6DoF motions, and the motions of each rigid body influenced the motion of the other. The presence of 2 rigid bodies meant that the overall platform was influenced by motion combinations not present in a single rigid body system. Any changes in inertia affect T_r to a large extent. The only value of T_r that was affected was

the value for surge between *V9* and *V10*. It was suspected that a possible change in the mooring configuration between the setups was the cause for this. Analysis of test results was conducted several weeks after testing was completed. This anomaly points to the fact that the results should be checked throughout the testing campaign. Had the results been checked throughout testing, this discrepancy in the results would have been spotted, the cause for the discrepancy could have been found and fixed, and the tests could have been re-run without a considerable loss of time.

- Model B was the same as model A in the sense that changes in inertia and CoG had more of an effect on $T_{r, mag}$ than they did on T_r.
- The changes were performed to see how potential uncertainties and errors in platform properties affect platform responses. The variations proved that uncertainties in the inertia and CoG of the model can significantly affect the response of the platform. Interestingly, the effect of changes in inertia do not change the platform response metrics linearly. The large initial change in the model properties between *V1* and *V2* brought about a similar magnitude change in the metrics to the much smaller change in model properties conducted between *V2* and *V3*. At times, the changes in the values of the metrics for each variation were not as expected when using theoretical relations to predict the platform responses. This was more of an issue with model B than model A. This unpredictability points to a need to carry out these kinds of variations to truly understand the effect that uncertainties in the inertia could have on model responses. The method acts as a sensitivity analysis for changes in model parameters. It provides further insight into the extent that uncertainties influence the results and could also help improve platform performance.

5.2.2 Conclusions from variations in wind emulation system.

The wind emulation system comparisons conducted for both models were extremely insightful. Between both models, the most basic method, an effective yet not overly complex method and arguably the most advanced method of wind emulation have been compared.

- Model A was used to compare the very basic and straightforward weighted pulley wind system and a thruster system. In theory, both systems were supposed to provide constant thrust. The comparison highlighted how much the choice of wind emulation system influenced the platform motions. In summary, the weighted pulley significantly dampened the platform motions.

- Interestingly, the wind emulation system did not have a significant influence on the period of resonance response, T_r. However, the magnitude of platform responses at resonance, compared using $T_{r,\,mag}$, were significantly affected by the change in the wind emulation system. Heave response was not significantly affected, but surge and pitch response were affected. The pitch response was more sensitive to the change in the wind emulation system. $T_{r,\,mag}$ was reduced nearly 89% with the pulley compared with the thruster.
- Much like the changes in inertia, the effect on surge response was amplified at resonance. The effect on $T_{r,\,mag}$ was much greater than the effect on M_{WF} for surge. All other platform motions other than roll were severely dampened by the pulley system.
- It is noted that the pulley used during testing was not perfect; it was old and most likely would not have performed as well as a newer pulley. The radius of the pulley was also relatively small. Friction could have been reduced by using a pulley with a larger radius. The rationale behind the pulley chosen has been mentioned above in Section 3.10.3. Given the severity of the changes induced by the pulley, it is concluded that the weighted pulley system should be avoided for use in early-stage wave tank testing unless there are no other options. While resonance periods were unaffected by the variation, the magnitude of resonance response was significantly dampened. Friction losses due to the pulley and the unpredictable motion of the mass attached mean that the realised thrust force applied at the top of the tower throughout each test is not the same as the weight attached at the other end of the system.

The wind emulation variations carried out for model B compared a very basic thruster, emulating a constant thrust force, like the thruster used for model A and the very advanced SiL system developed by CENER. The main differences between the two methods have been explained in detail in Sections 2.4.2 and 3.2.2 of this report.

- The differences between *V9* and *V12* were smaller than those between *V1* and *V4*.

- The SiL method did not have a significant effect on the period of resonance response for surge and heave. It did, however, influence the pitch resonance period. The exact reason for this change in the pitch resonance period, more specifically the reason for the low-frequency resonance peak, could not be determined with the available information. It has been hypothesised that the reason for the low-frequency peak was the two rigid body systems. We know from the data presented in model A that with a constant thruster, this peak does not occur for a simple semisubmersible design. The SiL system is highly advanced and reflects the aerodynamic loads experienced when combined wind and wave loading. Therefore, the SiL system is a far more realistic representation of the forces experienced in an ocean environment.
- The evidence from these variations suggests that the thruster, while an appropriate method of approximating platform responses under average load conditions, should not be used for more detailed analysis. In particular, where more complex multiple rigid body systems give rise to less predictable and more complex motions.

5.2.3 Conclusions from variations in mooring stiffness

Overall, the comparisons completed were extremely valuable. It proved beyond doubt that errors in mooring line properties have a considerable effect on platform motions, particularly surge.

- It was chosen that a 3% increase and decrease in the k-value for each spring would be used for comparison. This value was chosen based on the uncertainty in the method used to estimate the k-value of each spring. One interesting lesson from this experiment is how challenging it can be to obtain springs with the desired k-values. Anecdotal evidence within the facility suggested it had been a challenge in the past. This was also the case during this testing campaign. The springs that arrived in the lab were less than a percent less than the initial k-value and 14% larger than the initial spring. Had the errors in the k-value been consistent, it would have been possible to re-order with a corrected value, but this was not the case. This problem has been consistently encountered despite sourcing springs from several locations. Springs should always be calibrated before use, and it is not reliable to go on the specifications of the manufacturer. It seems like a trivial task, but one very simple learning outcome of this testing campaign is the need to order springs well in advance of the starting testing. This allows time to rectify any problems that might arise from the springs that arrive on site. In the case of this testing campaign, a busy wave tank testing schedule at Lir meant that there was no time to reorder springs that would better represent the desired variations.

- The variations in mooring stiffness conducted did present vital learnings. Variations in mooring stiffness for horizontal mooring systems affect the surge natural period mostly, but not significantly. Given that the changes in inertia conducted between *V1*, *V2*, and *V3* did not affect T_r for surge massively either, it would suggest that hydrostatic stiffness has the most significant influence on T_r for surge.
- The influence of changes in mooring stiffness was amplified at resonance. Increases in mooring stiffness did have the effect of damping down the magnitude of platform responses in surge. Errors in mooring line stiffnesses also affected the $T_{r,\,mag}$ for pitch. The increase in mooring stiffness between *V7* and *V8* increased the magnitude of pitch response. Unfortunately, however, there were not enough data points to see the trends for the effects on each response.

5.3 Overall Conclusions

Detailed conclusions for each of the variations conducted have been given in Section 5.2 above. This section presents conclusions on a higher level basis. These higher-level conclusions are presented below.

- Uncertainties and errors due to the model inertia, wind emulation system and mooring stiffness all have a significant effect on platform motions. The influence of all these factors was amplified at resonance. While there may not have been a considerable impact across most frequencies of platform response, within a narrow band to either side of the eigenfrequencies, as represented by $T_{r,\,mag}$, the influence of these uncertainties and errors was far more apparent. This could be seen visually by comparing the PSDs of platform response and by comparing M_{WF} and $T_{r,\,mag}$ for surge response.
- Uncertainties in inertia and CoG had more influence on device motions than uncertainties in mooring stiffness.

- Of the variations completed, the uncertainties in inertia about the y-axis, $I_{yy,}$ had more influence on the platform pitch than the inertia about the x-axis, I_{xx}, had on platform surge.
- Of the uncertainties in physical parameters investigated, the surge was most significantly affected by the uncertainties in mooring stiffness. In particular in the magnitude of surge response. Given that neither changes in inertia nor changes to mooring stiffness in surge had a significant impact on T_r for surge, it has been concluded that hydrostatic stiffness plays the most significant roll in determining the natural period in surge of semi-submersible platforms.
- The effect of the uncertainties and errors in inertia were easier to quantify for model A than model B. This was due to the more complex design of model B and the less conventional motions that arose as a result. Where systems with multiple rigid bodies are used, the motions of each rigid body should be tracked to assess the effect that each body has on the others.
- Conducting a sensitivity analysis across the range of the uncertainty bounds for key parameters like CoG, Inertia and mooring stiffness facilitates assessment of the potential error that these uncertainties could cause and would further enhance developers' understanding of their platform.
- The choice of wind emulation system is a significant source of uncertainty. The variation between the results using the constant thruster and the SiL for model B and the pulley for model A highlighted this. The constant thruster is a tried and tested method for early-stage analysis on simple designs like semi-submersibles and spar-boys. When compared with a more realistic wind emulation method like SiL, it is clear that the thruster is not appropriate for more detailed analysis. There were significant differences between the results obtained with the thruster and SiL, particularly for pitch responses.

Uncertainties during the wave tank testing campaign are highly likely. The uncertainties in Inertia, CoG, and mooring stiffness investigated during these testing campaigns reflect a worst-case scenario. The extent of errors in model properties can be reduced by introducing mitigation measures that could correct these errors into the model design and allowing time before the test campaign implement these mitigation measures. The uncertainties in the methods used to estimate model properties are difficult to ignore and do significantly influence the response of the platform. Uncertainties due to wind emulation system, inertia, CoG and mooring stiffness do have a significant influence on platform motions.

Wave tank testing of FOWTs is a cost-effective and accurate method of assessing model performance in various wind and wave conditions. However, the accuracy of results obtained from testing depends on the uncertainty associated with key physical parameters and the wind emulation system used. From the results obtained during testing, it is estimated that wave tank testing can be conducted with approximately ***5%*** uncertainty assuming that errors in model construction and material properties are limited, and the uncertainties are solely due to the procedures used to measure the model and material properties. This value is approximated based on the errors obtained for model A during this test campaign and assumes that the weighted pulley wind emulation system would not be used.

5.4 Recommendations for further research

The research conducted during this study was highly beneficial. However, given what was learned during the testing campaign and the results were presented in this report, the research could go further than what was done in this study.

- It would be relevant to conduct more variations for both inertia and mooring stiffness. There were only 3 data points for the inertia variations, and they all reflected decreases in I_{yy} and CoG_z. It would be beneficial to collect further data on the influence of decreases in inertia and collect data for different increases in inertia and CoG_Z. As mentioned above, increases in CoG_z were not feasible for these models. A good outcome of further research would be to plot a graph showing the effect that increases and decreases in model inertia would have on the platform motions. (Gueydon et al., 2022) conducted a similar study using numerical data and then applied theoretical relations to the variations to predict the effect that these variations would have. Some of the data from this testing campaign has been used for that study and showed good agreement with the predictions from the theoretical relations. It would improve understanding to compare the testing results with many more data points to the predicted outcomes using theoretical relations.

- These variations focused primarily on changes I_{yy} and CoG_z, which in turn changed the I_{xx} value by a similar amount. Data shown in Figure 53 hinted that even the slight changes in I_{zz} brought about by *V2* and *V3* influenced the heave response of the platform. However, the magnitude of each variation in I_{zz} was so small that it could not be concluded definitively how much of an effect this had. This could be investigated further.
- Much like with the variations in inertia, conducting more variations in mooring stiffness would be a valuable piece of research. This would allow a graph to be created showing the influence of mooring stiffness on each of the key motions. Data shown in Figure 72 showed that the mooring stiffness had a significant impact on the magnitude of pitch response and surge response. However, given a lack of data, the trend for pitch was more challenging to assess.
- While (Judge et al., 2021) investigated the influence of wave repeatability on experimental uncertainties for OWCs, it would be useful to conduct a similar study for FOW platforms. While this study concluded influence of wave repeatability was consistent for each variation, it would be useful to quantify the influence of uncertainties in wave period and wave height, on model responses for FOW platforms.
- A linear mooring system is only one type of mooring system. Many other types are used for different models. Similar to what was done with the wind emulation system, the effect that different methods of mooring truncation for the same full-scale mooring system would be a useful comparison. By comparing industry-standard methods of mooring truncation to more novel ideas and concepts, it would soon become apparent which methods are viable for wide-scale use in the future.
- Within the different truncation methods, another type of sensitivity analysis for the effect that changes of key parameters within each truncation system would have on platform responses could be performed. This would help classify how sensitive the method of mooring truncation is to errors and uncertainties in the setup procedure and mooring configuration.

6 References

Ackermann, T. (2005). Wind Power in Power Systems. In *Wind Power in Power Systems*. https://doi.org/10.1002/0470012684

American Society of Mechanical Engineers. (2006). Test Uncertainty. *Encyclopedia of Database Systems*, *2005*, 1068–1068. https://doi.org/10.1007/978-0-387-39940-9_2597

Azcona, J., Bouchotrouch, F., González, M., Garciandía, J., Munduate, X., Kelberlau, F., & Nygaard, T. A. (2014). Aerodynamic thrust modelling in wave tank tests of offshore floating wind turbines using a ducted fan. *Journal of Physics: Conference Series*, *524*(1). https://doi.org/10.1088/1742-6596/524/1/012089

Azcona, J., Bouchotrouch, F., & Vittori, F. (2019). Low-frequency dynamics of a floating wind turbine in wave tank–scaled experiments with SiL hybrid method. *Wind Energy*, *22*(10), 1402–1413. https://doi.org/10.1002/we.2377

Bahaj, A. S., Myers, L., & James, P. A. B. (2007). Urban energy generation: Influence of micro-wind turbine output on electricity consumption in buildings. *Energy and Buildings*, *39*(2), 154–165. https://doi.org/10.1016/j.enbuild.2006.06.001

Bailey, H., Brookes, K. L., & Thompson, P. M. (2014). Assessing environmental impacts of offshore wind farms: Lessons learned and recommendations for the future. *Aquatic Biosystems*, *10*(1), 1–13. https://doi.org/10.1186/2046-9063-10-8

Bergdahl, L., Palm, J., Eskilsson, C., & Lindahl, J. (2016). Dynamically scaled model experiment of a mooring cable. *Journal of Marine Science and Engineering*, *4*(1). https://doi.org/10.3390/jmse4010005

Blue H Technologies. (2017). *The design engineer, system integrator and technology provider for floating foundation systems and multi-purpose platforms at sea*. www.bluehengineering.com,info@bluehengineering.com,

Boccia, V., Renga, A., Rufino, G., D'Errico, M., Moccia, A., Aragno, C., & Zoffoli, S. (2015). Linear dispersion relation and depth sensitivity to swell parameters: Application to synthetic aperture radar imaging and bathymetry. *Scientific World Journal*, *2015*. https://doi.org/10.1155/2015/374579

Bozonnet, P., Caillé, F., Blondel, F., Melis, C., Poirette, Y., & Pedrizet, T. (2017). A Focus on Fixed Wind Turbine Tests to Improve Coupled Simulations of Floating Wind Turbine Model Tests. *The Proceedings of the 27th(2017) International Ocean and Polar Engineering Conference.*

Brodtkorb, P. A., Johannesson, P., Lindgren, G., Rychlik, I., Rydén, J., & Sjö, E. (2000, May 28). Matlab toolbox for random waves and loads. *In Proceedings of the 10th International Offshore and Polar Engineering Conference*.

Butterfield, S., Musial, W., Jonkman, J., Sclavounos, P., & Wayman, L. (2007). Engineering Challenges for Floating Offshore Wind Turbines. *2005 Copenhagen Offshore Wind Conference Copenhagen, Denmark*, 13. https://doi.org/10.1111/j.1365-313X.2008.03515.x.

BVG. (2019). *Guide to an offshore wind farm*. www.thecrownestate.co.uk

Chakrabarti, S. K. (2005). Handbook of Offshore Engineering. In *Handbook of Offshore Engineering: Vol. II*. http://dx.doi.org/10.1016/B978-0-08-044381-2.50022-9

Chen, X., Yu, H., Wang, W., & Wang, B. (2019). *Analysis of Motion Response of Wind Turbine Platform Considering Different Heading Angles and Water Depths*.

Chester, R., Desmond, C., Murphy, J., & Watson, S. (2018). MOORING LINE DYNAMICS OF A SEMI-SUBMERSIBLE WIND ENERGY PLATFORM: CROSS VALIDATION OF TWO COMMERCIAL NUMERICAL CODES WITH EXPERIMENTAL DATA. *Offshore & Arctic Engineering*, *38*.

Chester, R., Murphy, J., & Dinh, V. N. (2019). *Co-designing opportunities towards the development of Irish offshore wind Work Package 3: Cost Optimisation for Offshore Wind Deliverable D3.1 Initial Issues in the Development of Offshore Wind in Ireland Summary*. www.marei.ie/eirwind

Ching, J. (2011). Practical Monte Carlo Based Reliability Analysis and Design Methods for Geotechnical Problems. *Applications of Monte Carlo Method in Science and Engineering*, *February 2011*. https://doi.org/10.5772/15136

Crosetto, M., Tarantola, S., & Saltelli, A. (2000). Sensitivity and uncertainty analysis in spatial modelling based on GIS. *Agriculture, Ecosystems & Environment*, *81*(1), 71–79. https://doi.org/10.1016/S0167-8809(00)00169-9

Cummins, V., & McKeogh, E. (2020). *Blueprint for offshore wind in Ireland 2020-2050: A Research Synthesis*. https://doi.org/http://doi.org/10.5281/zenodo.3958261

Darrieus, G. J. M. (1931). Turbine Having its Rotating Shaft Transverse to the Flow of the Current. In *US Patent No. 1835081.*

Davey, T., Sarmiento, J., Ohana, J., Thiebaut, F., Haquin, S., Weber, M., Gueydon, S., Judge, F., Lyden, E., O'Shea, M., Gabl, R., Jordan, L.-B., Hann, M., Wang, D., Collins, K., Conley, D., Greaves, D., Ingram, D. M., & Murphy, J. (2021). Round Robin Testing: Exploring Experimental Uncertainties through a Multifacility Comparison of a Hinged Raft Wave Energy Converter. *Journal of Marine Science and Engineering*, *9*(9), 946. https://doi.org/10.3390/jmse9090946

Dean, R. G., & Dalrymple, R. A. (1991). *Water Wave Mechanics for Engineers and Scientists* (Vol. 2). WORLD SCIENTIFIC. https://doi.org/10.1142/1232

Desmond, C. J., Hinrichs, J. C., & Murphy, J. (2019). Uncertainty in the Physical Testing of Floating Wind Energy Platforms' Accuracy versus Precision. *Energies*, *12*(3), 1–14. https://doi.org/10.3390/en12030435

DNV GL. (2018). *Floating wind turbine structures*. http://www.dnvgl.com,

Dvorak, P. (2021). *Factoring in six degrees of freedom for floating offshore wind turbines*.

Edinburgh Designs. (2021, November 19). *Edinburgh Designs Wave Gauges*.

Edvotek. (2021). *Edvotek - THE BIOTECHNOLOGY EDUCATION COMPANY*.

emeraldfloatingwind. (2020). *About Emerald*. Emeraldfloatingwind.Com. https://emeraldfloatingwind.com/about/

Equinor. (2020). *Hywind scotland* (p. 1).

Equinor. (2021a). *Hywind Tampen: the world's first renewable power for offshore oil and gas*. Equinor.Com. https://www.equinor.com/en/what-we-do/hywind-tampen.html

Equinor. (2021b, March 23). *Hywind Scotland remains the UK's best performing offshore wind farm*. Equinor.Com. https://www.equinor.com/en/news/20210323-hywind-scotland-uk-best-performing-offshore-wind-farm.html

Esber, G., Esber, G., Draack, L., & Adam, F. (2019, October 29). *A parameter study of the metacentric height role and limitations in minimizing the trim of the DTU 10-MW wind turbine mounted on moored spar-buoy floater*. https://www.researchgate.net/publication/337000366

Esteban, M. D., Diez, J. J., López, J. S., & Negro, V. (2011). Why offshore wind energy? *Renewable Energy*, *36*(2), 444–450. https://doi.org/10.1016/j.renene.2010.07.009

ETI. (2015). Offshore Wind Floating Wind Technology. *Energy Technologies Institute*, 13.
European Commission. (2013). Green Paper - A 2030 framework for climate and energy policies. In *COM(2013) 169 final*.
EurOtop. (2018). *Manual on wave overtopping of sea defences and related structures. An overtopping manual largely based on European research, but for worldwide application.* 320.
Floating Offshore Wind Centre of Excellence. (2021). *Floating Offshore Wind : Cost Reduction Pathways to subsidy free*.
FloWave. (2022). *FloWave Ocean Energy Research Facility*. https://www.flowavett.co.uk/
Fowler, M. J., Kimball, R. W., Iii, D. A. T., & Goupee, A. J. (2013, June 9). DESIGN AND TESTING OF SCALE MODEL WIND TURBINES FOR USE IN WIND/WAVE BASIN MODEL TESTS OF FLOATING OFFSHORE WIND TURBINES. *Proceedings of the ASME 2013 32nd International Conference on Ocean, Offshore and Arctic Engineering OMAE2013*. http://asme.org/terms
Fowler, M. J., Kimball, R. W., Thomas, D. A., & Goupee, A. J. (2013, June 9). Design and Testing of Scale Model Wind Turbines for Use in Wind/Wave Basin Model Tests of Floating Offshore Wind Turbines. *Volume 8: Ocean Renewable Energy*. https://doi.org/10.1115/OMAE2013-10122
Ghigo, A., Cottura, L., Caradonna, R., Bracco, G., & Mattiazzo, G. (2020). Platform optimization and cost analysis in a floating offshore wind farm. *Journal of Marine Science and Engineering*, *8*(11), 1–26. https://doi.org/10.3390/jmse8110835
Gosch, M., Cronin, M., Rogan, E., Hunt, W., Luck, C., & Jessopp, M. (2019). Spatial variation in a top marine predator’s diet at two regionally distinct sites. *PLOS ONE*, *14*(1), e0209032. https://doi.org/10.1371/journal.pone.0209032
Gueydon, S., Bayati, I., & de Ridder, E. J. (2020). Discussion of solutions for basin model tests of FOWTs in combined waves and wind. *Ocean Engineering*, *209*. https://doi.org/10.1016/j.oceaneng.2020.107288
Gueydon, S., Judge, F., Lyden, E., O’shea, M., Thiebaut, F., Boulluec, M. le, Caverne, J., Ohana, J., Bouscasse, B., Kim, S., Day, S., Dai, S., & Murphy, J. (2021). A heuristic approach for inter-facility comparison of results from round robin testing of a floating wind turbine in irregular waves. *Journal of Marine Science and Engineering*, *9*(9). https://doi.org/10.3390/jmse9091030
Gueydon, S., Judge, F. M., O’shea, M., Lyden, E., le Boulluec, M., Caverne, J., Ohana, J., Kim, S., Bouscasse, B., Thiebaut, F., Day, S., Dai, S., & Murphy, J. (2021). Round robin laboratory testing of a scaled 10 mw floating horizontal axis wind turbine. *Journal of Marine Science and Engineering*, *9*(9). https://doi.org/10.3390/jmse9090988
Gueydon, S., Lyden, E., Judge, F., O’shea, M., Murphy, J., & Desmond, C. (2022). Looking for a simplified approach for the propagation of systematic uncertainty in basin model tests. *TBC*.
Gustavo, M., & Enrique, P. (2011). Modelling and Control Design of Pitch-Controlled Variable Speed Wind Turbines. *Wind Turbines*, *May*. https://doi.org/10.5772/15880
Hannon, M., Topham, E., Dixon, James, Mcmillan, D., & Collu, M. (2019). *Offshore wind, ready to float? Global and UK trends in the floating offshore wind market*. https://doi.org/10.17868/69501
Harnois, V., Weller, S. D., Johanning, L., Thies, P. R., le Boulluec, M., le Roux, D., Soulé, V., & Ohana, J. (2015). Numerical model validation for mooring systems: Method and

application for wave energy converters. *Renewable Energy*, *75*, 869–887. https://doi.org/10.1016/j.renene.2014.10.063
HEDGES, T. S. (1995). REGIONS OF VALIDITY OF ANALYTICAL WAVE THEORIES. *Proceedings of the Institution of Civil Engineers - Water Maritime and Energy*, *112*(2), 111–114. https://doi.org/10.1680/iwtme.1995.27656
Heidari, S. (2017). *Economic modelling of floating offshore wind power: Calculation of Levelized cost of energy*.
Hinrichsen, P. F. (2014). BIFILAR SUSPENSION MEASUREMENT OF BOAT INERTIA PARAMETERS. In *Journal of Sailboat Technology*.
Holmes, B. (2009). *Tank Testing of Wave Energy Conversion Systems*.
Huang, Y., & Wan, D. (2020). Investigation of interference effects between wind turbine and spar-type floating platform under combined wind-wave excitation. *Sustainability (Switzerland)*, *12*(1). https://doi.org/10.3390/SU12010246
Hurley, W. L., & Nordstrom, C. J. (2014). *A cost study of the PelaStar floating foundation system in UK waters* .
IEA. (2019). Offshore Wind Outlook 2019: World Energy Outlook Special Report. *International Energy Association*, 98.
IPCC. (2012). Summary for policymakers. In *Managing the Risks of Extreme Events and Disasters to Advance Climate Change Adaptation: Special Report of the Intergovernmental Panel on Climate Change* (Vol. 9781107025). https://doi.org/10.1017/CBO9781139177245.003
IPCC. (2018). *Framing and Context. In: Global Warming of 1.5°C. An IPCC Special Report on the impacts of global warming of 1.5°C above pre-industrial levels and related global greenhouse gas emission pathways, in the context of strengthening the global response to the threat of climate change, sustainable development, and efforts to eradicate poverty*.
Islam, M., Jahra, F., & Hiscock, S. (2016). Data analysis methodologies for hydrodynamic experiments in waves. *Journal of Naval Architecture and Marine Engineering*, *13*(1), 1–15. https://doi.org/10.3329/jname.v13i1.25347
ISO. (2008a). Joint Committee For Guides In Metrology-Evaluation of measurement data — Guide to the expression of uncertainty in measurement. *International Organization for Standardization Geneva ISBN*, *50*(September), 134.
ISO. (2008b). Joint Committee for Guides in Metrology-Evaluation of measurement data — Supplement 1 to the “Guide to the expression of uncertainty in measurement” — Propagation of distributions using a Monte Carlo method. *International Organization for Standardization Geneva ISBN*, *JCGM 101:2008*.
ITTC. (2008). Guide to the Expression of Uncertainty in Experimental Hydrodynamics - ITTC Recommended Procedures and Guidelines, Procedure 7.5-02-01-01, Revision 01. *Specialist Committee on Uncertainty Analysis of 25th ITTC*.
ITTC. (2017). *ITTC-Uncertainty Analysis for a Wave Energy Converter*.
IWEA. (2018). *70 By 30: A 70% Renewable Electricity Vision for Ireland in 2030* (Issue October).
Jain, A., Bansal, R., Kumar, A., & Singh, K. (2015). A comparative study of visual and auditory reaction times on the basis of gender and physical activity levels of medical first year students. *International Journal of Applied and Basic Medical Research*, *5*(2), 124. https://doi.org/10.4103/2229-516x.157168

James, R., & Marc Costa Ros. (2015). Floating Offshore Wind: Market and Technology Review - Prepared for the Scottish Government. In *Carbon Trust*. https://doi.org/10.1016/j.jcp.2016.01.012

James, R., & Weng, W.-Y. (2018). *Floating Wind Joint Industry Project; Key Findings from Electrical Systems, Mooring Systems, and Infrastructure & Logistics studies*.

Judge, F., Lyden, E., Flannery, B., Murphy, J., & Centre, M. (2021). *Uncertainty in wave basin testing of a fixed oscillating water column wave energy converter*. 1–22.

Kaldellis, J. K., & Zafirakis, D. (2011). The wind energy (r)evolution: A short review of a long history. *Renewable Energy*, *36*(7), 1887–1901. https://doi.org/10.1016/j.renene.2011.01.002

Katsouris, G., & Marina, A. (2016). *Cost Modelling of Floating Wind Farms*.

Koerkamp, B. G., Stijnen, T., Weinstein, M. C., & Hunink, M. G. M. (2011). The combined analysis of uncertainty and patient heterogeneity in medical decision models. *Medical Decision Making : An International Journal of the Society for Medical Decision Making*, *31*(4), 650–661. https://doi.org/https://doi.org/10.1177/0272989X10381282

L. Wang, J. Wei, X. W., & Zhang, X. (2011). The Development of Offshore wind Energy in the World. *2009 World Non-Grid-Connected Wind Power and Energy Conference*. https://doi.org/10.1109/WNWEC.2009.5335761

Lee, H., & Lee, D. J. (2019). Effects of platform motions on aerodynamic performance and unsteady wake evolution of a floating offshore wind turbine. *Renewable Energy*, *143*, 9–23. https://doi.org/10.1016/j.renene.2019.04.134

MaRINET1. (2015). *Report on Physical Modelling Methods for Floating Wind Turbines WP2: Marine Energy System Testing-Standardisation and Best Practice Report on Physical Modelling Methods for Floating Wind Turbines*. www.fp7-marinet.eu

MaRINET2. (2019). *D4.1-3 Common MaRINET 2 standard testing and benchmarking plan_final-Wind*.

MaRINET2. (2021a). *MaRINET2*. http://www.marinet2.eu/

MaRINET2. (2021b). *MaRINET2-Final guidelines for test facilities*.

Martin, D., Zuo, L., Parker, R. G., & Tafti, D. K. (2017). *Hydrodynamic Design Optimization and Wave Tank Testing of a Self-Reacting Two-Body Wave Energy Converter*.

Matha, D., Sandner, F., Molins, C., Campos, A., & Cheng, P. W. (2015). Efficient preliminary floating offshore wind turbine design and testing methodologies and application to a concrete spar design. *Philosophical Transactions of the Royal Society A: Mathematical, Physical and Engineering Sciences*, *373*(2035), 20140350. https://doi.org/10.1098/rsta.2014.0350

McAuliffe, D., Delivand, K., Connell, O., Hagan, O., Hanlon, O., Terra Miranda Machado, J., Sweeney, J., & Towe, R. (2020). *Work Package 6: Synthesis Deliverable 6.2 FINAL SYNTHESIS REPORT*. https://doi.org/10.5281/zenodo.3958261

McCombes, T., Johnstone, C. M., Holmes, B., Myers, L. E., Bahaj, A. S., & Kofoed, J. P. (2010). Deliverable 3.4 - Best practice for tank testing of small marine energy devices. *EquiMar Project*, 1–48.

Menon, V. (2020). *The Startup - Understanding Probability Distribution*. https://medium.com/swlh/understanding-probability-distribution-b5c041f5d564

Mohamed, M. H., Ali, A. M., & Hafiz, A. A. (2015). CFD analysis for H-rotor Darrieus turbine as a low speed wind energy converter. *Engineering Science and Technology, an International Journal*, *18*(1), 1–13. https://doi.org/10.1016/j.jestch.2014.08.002

Molins, C., Trubat, P., Gironella, X., & Campos, A. (2015). Design optimization for a truncated catenary mooring system for scale model test. *Journal of Marine Science and Engineering*, *3*(4), 1362–1381. https://doi.org/10.3390/jmse3041362

Müller, K., Guzmán, R. F., Zhou, S., Lerch, M., Proskovics, R., Pérez, G., Mendikoa, I., Matha, D., Borisade, F., Bhat, J., Scheffler, R., Thys, M., Bredmose, H., Madsen, F., & Jurado, A. M. P. (2019). *LIFES50+ D7.11: design practice for 10MW+ FOWT support structures*.

Müller, K., Sandner, F., Bredmose, H., Azcona, J., Manjock, A., & Pereira, R. (2014). *IMPROVED TANK TEST PROCEDURES FOR SCALED FLOATING OFFSHORE WIND TURBINES*. www.vindenergi.dtu.dk

Murphy, S., Bhinder, M. A., Casaubieilh, P. ;, & Sheng, W. (2015, September). Effects of tidal range on mooring systems of wave energy converters. *11th European Wave and Tidal Energy Conference (EWTEC)*. http://www.ewtec.org/proceedings/

Musial, W., Heimiller, D., Beiter, P., Scott, G., & Draxl, C. (2016). *2016 Offshore Wind Energy Resource Assessment for the United States*. *September*, 88.

Myhr, A., Bjerkseter, C., Ågotnes, A., & Nygaard, T. A. (2014). Levelised cost of energy for offshore floating wind turbines in a lifecycle perspective. *Renewable Energy*, *66*, 714–728. https://doi.org/10.1016/j.renene.2014.01.017

Newman, F. H., & Searle, V. H. L. (1951). *The General Properties of Matter* (Vol. 4). Edward Arnold.

Newman, J. N. (2017). *Marine Hydrodynamics* (40th Anniversary). The MIT Press.

O'Donnell, D., Murphy, J., Desmond, C., Jaksic, V., & Pakrashi, V. (2017). Tuned Liquid Column Damper based Reduction of Dynamic Responses of Scaled Offshore Platforms in Different Ocean Wave Basins. *Journal of Physics: Conference Series*, *842*(1). https://doi.org/10.1088/1742-6596/842/1/012043

O'Donnell, D., Murphy, J., & Pakrashi, V. (2021). Comparison of Response Amplitude Operator Curve Generation Methods for Scaled Floating Renewable Energy Platforms in Ocean Wave Basin. *ASME Letters in Dynamic Systems and Control*, *1*(2). https://doi.org/10.1115/1.4049169

Oguz, E., Clelland, D., Day, A. H., Incecik, A., López, J. A., Sánchez, G., & Almeria, G. G. (2018). Experimental and numerical analysis of a TLP floating offshore wind turbine. *Ocean Engineering*, *147*, 591–605. https://doi.org/10.1016/j.oceaneng.2017.10.052

Ohana, J., Judge, F., O'Shea, M., Lyden, E., & Gueydon, S. (2021). *Round robin tests of a hinged raft wave energy converter*.

Orphin, J. (2020). *Uncertainty in Hydrodynamic Model Test Experiments of Wave Energy Converters* (Issue September). University of Tasmania.

Orphin, J., Howe, D., Nader, J., & Penesis, I. (2017). Experimental Uncertainty Analysis of an OWC Wave Energy Converter. *Proceedings of the Twelfth European Wave and Tidal Energy Conference*, *September*, {1096-1}--{1096-10}.

Orphin, J., Nader, J. R., & Penesis, I. (2021). Uncertainty analysis of a WEC model test experiment. *Renewable Energy*, *168*, 216–233. https://doi.org/10.1016/j.renene.2020.12.037

Orphin, J., Penesis, I., & Nader, J. (2018). Uncertainty Analysis for a Wave Energy Converter : the Monte Carlo Method. *Awtec*, *September*.

Paduano, B., Giorgi, G., Gomes, R. P. F., Pasta, E., Henriques, J. C. C., Gato, L. M. C., & Mattiazzo, G. (2020). Experimental Validation and Comparison of Numerical Models for the Mooring System of a Floating Wave Energy Converter. *Journal of Marine Science and Engineering*, *8*(8), 565. https://doi.org/10.3390/jmse8080565

Papazoglou, V. J., Mavrakos, S. A., & Triantafyllou, M. S. (1990). Non-linear cable response and model testing in water. *Journal of Sound and Vibration*, *140*(1), 103–115. https://doi.org/10.1016/0022-460X(90)90909-J

Parnell, J. (2020). *Siemens Gamesa Launches 14MW Offshore Wind Turbine, World's Largest*. Greentechmedia. https://www.greentechmedia.com/articles/read/siemens-gamesa-takes-worlds-largest-turbine-title

Pasqualetti, M., Righter, R., & Gipe, P. (2004). History of Wind Energy. *Encyclopedia of Energy*, *September 2014*, 419–434.

Payne, G. S. (2008). *Guidance for the experimental tank testing of wave energy converters*. *March*.

Pham, T. D., & Shin, H. (2019). Validation of a 750 kW semi-submersible floating offshore wind turbine numerical model with model test data, part I: Model-I. *International Journal of Naval Architecture and Ocean Engineering*, *11*(2), 980–992. https://doi.org/10.1016/j.ijnaoe.2019.04.005

Pires, O., Azcona, J., Vittori, F., Bayati, I., Gueydon, S., Fontanella, A., Liu, Y., de Ridder, E. J., Belloli, M., & van Wingerden, J. W. (2020). Inclusion of rotor moments in scaled wave tank test of a floating wind turbine using SiL hybrid method. *Journal of Physics: Conference Series*, *1618*(3). https://doi.org/10.1088/1742-6596/1618/3/032048

Pisano, F. (2019). Input of advanced geotechnical modelling to the design of offshore wind turbine foundations. *Conference Paper*, *September*. https://doi.org/10.32075/17ECSMGE-2019-1109

Porter, A., & Phillips, S. (2016). *Determining the Infrastructure Needs to Support Offshore Floating Wind and Marine Hydrokinetic Facilities on the Pacific West Coast and Hawaii*. 238.

PrinciplePower. (2019). *WindFloat Atlantic*. Principlepower,Com. https://www.principlepower.com/projects/windfloat-atlantic

PrinciplePower. (2021). *Kincardine Offshore Wind Farm*. Principlepower.Com. https://www.principlepower.com/projects/kincardine-offshore-wind-farm

Qiu, W., Sales Junior, J., Lee, D., Lie, H., Magarovskii, V., Mikami, T., Rousset, J. M., Sphaier, S., Tao, L., & Wang, X. (2014). Uncertainties related to predictions of loads and responses for ocean and offshore structures. *Ocean Engineering*, *86*, 58–67. https://doi.org/10.1016/j.oceaneng.2014.02.031

Rinaldi, G., Garcia-Teruel, A., Jeffrey, H., Thies, P. R., & Johanning, L. (2021). Incorporating stochastic operation and maintenance models into the techno-economic analysis of floating offshore wind farms. *Applied Energy*, *301*. https://doi.org/10.1016/j.apenergy.2021.117420

Robertson, A., Bachynski, E. E., Gueydon, S., Wendt, F., & Schünemann, P. (2020). Total experimental uncertainty in hydrodynamic testing of a semisubmersible wind turbine, considering numerical propagation of systematic uncertainty. *Ocean Engineering*, *195*(December 2019), 106605. https://doi.org/10.1016/j.oceaneng.2019.106605

Robertson, A. N. (2017). Uncertainty analysis of oc5-deepcwind floating semisubmersible offshore wind test campaign. *Proceedings of the International Offshore and Polar Engineering Conference*, *July*, 482–489.

Robertson, A. N., Bachynski, E. E., Gueydon, S., Wendt, F., Schünemann, P., & Jonkman, J. (2018). Assessment of experimental uncertainty for a floating wind semisubmersible under hydrodynamic loading. *Proceedings of the International Conference on Offshore*

Mechanics and Arctic Engineering - OMAE, *10*(June). https://doi.org/10.1115/OMAE2018-77703

Röckmann, C., Lagerveld, S., & Stavenuiter, J. (2017). Operation and Maintenance Costs of Offshore Wind Farms and Potential Multi-use Platforms in the Dutch North Sea. In *Aquaculture Perspective of Multi-Use Sites in the Open Ocean* (pp. 97–113). Springer International Publishing. https://doi.org/10.1007/978-3-319-51159-7_4

Rogowski, K., Hansen, M. O. L., & Bangga, G. (2020). Performance analysis of a h-darrieuswind turbine for a series of 4-digit NACA airfoils. *Energies*, *13*(12). https://doi.org/10.3390/en13123196

Sahnoun, M., Baudry, D., Mustafee, N., Louis, A., Smart, P. A., Godsiff, P., & Mazari, B. (2015). Modelling and simulation of operation and maintenance strategy for offshore wind farms based on multi-agent system. *Journal of Intelligent Manufacturing Volume*, *30*(2019), 2981–2997. https://doi.org/https://doi.org/10.1007/s10845-015-1171-0

Scheffler, R., Matha, D., Brons-illig, C., Mitzlaff, A., & Scheffler, R. (2017). Fabrication installation constraints for floating wind and implications on current infrastructure and design. *Energy Procedia*, *137*, 299–306.

Schünemann, P., Zwisele, T., Adam, F., & Ritschel, U. (2018, June 17). Development of a Scaled Rotor Blade for Tank Tests of Floating Wind Turbine Systems. *Volume 10: Ocean Renewable Energy*. https://doi.org/10.1115/OMAE2018-77156

Schwartz, A. B., Malick, S., & Friesen, J. R. (1957). Measurement of the Moment of Inertia of Missile-type Bodies. *Aircraft Engineering and Aerospace Technology*, *29*(9), 271–274. https://doi.org/10.1108/eb032869

SEAI. (2017). *Ireland's Energy Projections - Progress to targets, challenges and impacts*.

Seyr, H., & Muskulus, M. (2019). Decision support models for operations and maintenance for offshore wind farms: A review. *Applied Sciences (Switzerland)*, *9*(2). https://doi.org/10.3390/app9020278

Shahrukh Adnan, K., Rajprasad, K. R., Aravind, C. V., Wong, Y. W., Geo, S. S., & See, L. J. (2016). Comprehensive review on the wind energy technology. *International Journal of Control Theory and Applications*, *9*(6).

Shell. (2020). *Perdido - overview*. Shell. https://www.shell.com/about-us/major-projects/perdido/perdido-an-overview.html

Siemens Gamesa. (2020). *The SG 14-222 DD*.

Spfc.ie. (2021). *About Shannon Foynes Port*. https://www.sfpc.ie/about/

Steven Hughes. (1993). *Physical Models and Laboratory Techniques in Coastal Engineering* (Vol. 7). World Scientific. https://doi.org/https://doi.org/10.1142/2154

Student. (1908). The Probable Error of a mean. *Biometrika*, *6*(1), 1–25.

Tambke, J., Lange, M., Focken, U., Wolff, J.-O., & Bye, J. A. T. (2005). Forecasting offshore wind speeds above the North Sea. *Wind Energy*, *8*(1), 3–16. https://doi.org/10.1002/we.140

Taylor, B. N., & Kuyatt, C. E. (1994). Guidelines for Evaluating and Expressing the Uncertainty of NIST Measurement. In *National Institute for Standards and Technology, Gaithersburg, MD* (p. D.1.1.2).

Tdistributiontable. (2020). *Student's T distribution*. https://www.tdistributiontable.com/

The Crown Estate. (2012). *Offshore wind cost reduction-Pathways study*. 88 pp.

Tran, T. T., & Kim, D. H. (2015). The platform pitching motion of floating offshore wind turbine: A preliminary unsteady aerodynamic analysis. *Journal of Wind Engineering and Industrial Aerodynamics*, *142*, 65–81. https://doi.org/10.1016/j.jweia.2015.03.009

Tumewu, Y., Crescenzo, P., & Sivaselvan, M. (2017). Numerical Simulation of the Influence of Platform Pitch Motion on Power Generation Steadiness in Floating Offshore Wind Turbines. *International Journal of Environmental Science & Sustainable Development.*, *2*(1), 92. https://doi.org/10.21625/essd.v1i2.39

Vortexfdc. (2021). *Ireland wind Map*. https://vortexfdc.com/knowledge/ireland-wind-map/

Ward, J. C., Goupee, A. J., Viselli, A. M., & Dagher, H. J. (2020). Influence of the Mass and Line Stiffness on the Dynamic Line Tension of a Floating Offshore Wind Turbine Stabilized by a Suspended Counterweight. *Journal of Physics: Conference Series*, *1452*(1). https://doi.org/10.1088/1742-6596/1452/1/012043

Wind Energy Ireland. (2021, December 13). *Wind Energy Ireland: Facts and Stats*. Wind Energy Ireland .

WindEurope. (2019). *Wind energy in Europe in 2019 - Trends and statistics*. https://windeurope.org/data-and-analysis/product/wind-energy-in-europe-in-2019-trends-and-statistics/

WindEurope. (2021, October 12). *Ireland's offshore ambitions are starting to take off*. Windeurope.Org. https://windeurope.org/newsroom/news/irelands-offshore-ambitions-are-starting-to-take-off/

Yang, W., Tian, W., Hvalbye, O., Peng, Z., Wei, K., & Tian, X. (2019). Experimental research for stabilizing offshore floating wind turbines. *Energies*, *12*(10). https://doi.org/10.3390/en12101947

7 Appendices

7.1 Test List Model A

Test ID	Wave Type	System	Load	Frequency Range	Wave Height(H_s)	Seed	Duration
1	PN	Calib		0.258 - 1.111	0.1	1	660 s
2	PN	Calib		0.258 - 1.111	0.1	1	660 s
3	PN	Calib		0.258 - 1.111	0.1	1	660 s
4	PN	Calib		0.258 - 1.111	0.1	1	660 s
5	PN	Calib		0.258 - 1.111	0.1	1	660 s
6	PN	Calib		0.258 - 1.111	0.1	1	1320 s
7	PN	Calib		0.258 - 1.111	0.1	1	1980 s
8	PN	Calib		0.258 - 1.111	0.05	1	660 s
9	PN	Calib		0.258 - 1.111	0.15	1	660 s
10	PN	Calib		0.258 - 1.111	0.2	1	660 s

1	Static load	1	3N	-	-	-	240 s
2	Static load	1	5N	-	-	-	240 s
3	Static load	1	7N	-	-	-	240 s
4	Static load	1	7N	-	-	-	240 s
5	Static load	1	7N	-	-	-	240 s
6	Static load	1	7N	-	-	-	240 s
7	Static load	1	8N	-	-	-	240 s
8	PN wave only	-	-	0.258 - 1.111	0.1	1	660 s
9	PN wave only	-	-	0.258 - 1.111	0.1	1	1320 s
10	PN wave only	-	-	0.258 - 1.111	0.1	1	1980 s
11	PN wave only	-	-	0.258 - 1.111	0.05	1	660 s
12	PN wave only	-	-	0.258 - 1.111	0.15	1	660 s
13	PN wave only	-	-	0.258 - 1.111	0.2	1	660 s
14	Decay surge x 3						240 s
15	Decay heave x 3						240 s
16	Decay pitch x 3						240 s
17	Decay in wind surge x 3						240 s
18	Decay in wind heave x 3						240 s
19	Decay in wind pitch x 3						240 s
20	PN and wind	1	3N	0.258 - 1.111	0.1	1	660 s
21	PN and wind	1	5N	0.258 - 1.111	0.1	1	660 s
22	PN and wind	1	7N	0.258 - 1.111	0.1	1	660 s
23	PN and wind	1	7N	0.258 - 1.111	0.1	1	660 s
24	PN and wind	1	7N	0.258 - 1.111	0.1	1	660 s
25	PN and wind	1	7N	0.258 - 1.111	0.1	1	660 s
26	PN and wind	1	7N	0.258 - 1.111	0.1	1	660 s
27	PN and wind	1	7N	0.258 - 1.111	0.1	1	1320 s
28	PN and wind	1	7N	0.258 - 1.111	0.1	1	1980 s
29	PN and wind	1	8N	0.258 - 1.111	0.1	1	240 s
30	Decay surge x 3	2	-	-	-	-	240s
31	Decay heave x 3	2	-	-	-	-	240s
32	Decay pitch x 3	2	-	-	-	-	240s
33	Decay in wind surge x 3	2	7N	-	-	-	240s
34	Decay in wind heave x 3	2	7N	-	-	-	240s
35	Decay in wind pitch x 3	2	7N	-	-	-	240s
36	PN	2		0.258 - 1.111	0.1	1	660s
37	PN and wind	2	7N	0.258 - 1.111	0.1	1	660s
38	PN and wind	2	7N	0.258 - 1.112	0.1	1	660s
39	PN and wind	2	7N	0.258 - 1.113	0.1	1	660s
40	PN and wind	2	7N	0.258 - 1.114	0.1	1	660s
41	PN and wind	2	7N	0.258 - 1.111	0.1	1	660s

42	Decay surge x 3	3	-	-	-	-	240 s
43	Decay heave x 3	3	-	-	-	-	240 s
44	Decay pitch x 3	3	-	-	-	-	240 s
45	Decay in wind surge x 3	3	-	-	-	-	240 s
46	Decay in wind heave x 3	3	-	-	-	-	240 s
47	Decay in wind pitch x 3	3	-	-	-	-	240 s
48	PN and wind	3	7N	0.258 - 1.111	0.1	1	660 s
49	PN and wind	3	7N	0.258 - 1.111	0.1	1	660 s
50	PN and wind	3	7N	0.258 - 1.111	0.1	1	660 s
51	PN and wind	3	7N	0.258 - 1.111	0.1	1	660 s
52	PN and wind	3	7N	0.258 - 1.111	0.1	1	660 s
53	Static load	4	3N	-	-	-	240 s
54	Static load	4	5N	-	-	-	240 s
55	Static load	4	7N	-	-	-	240 s
56	Static load	4	8N	-	-	-	240 s
57	Decay in wind surge x 3	4	7N	-	-	-	240 s
58	Decay in wind heave x 3	4	7N	-	-	-	240 s
59	Decay in wind pitch x 3	4	7N	-	-	-	240 s
60	PN and wind	4	7N	0.258 - 1.111	0.1	1	660 s
61	PN and wind	4	7N	0.258 - 1.111	0.1	1	660 s
62	PN and wind	4	7N	0.258 - 1.111	0.1	1	660 s
63	PN and wind	4	7N	0.258 - 1.111	0.1	1	660 s
64	PN and wind	4	7N	0.258 - 1.111	0.1	1	660 s
65	Decay in wind surge x 3	5	7N	-	-	-	240 s
66	Decay in wind heave x 3	5	7N	-	-	-	240 s
67	Decay in wind pitch x 3	5	7N	-	-	-	240 s
68	PN and wind	5	7N	0.258 - 1.111	0.1	1	660 s
69	PN and wind	5	7N	0.258 - 1.111	0.1	1	660 s
70	PN and wind	5	7N	0.258 - 1.111	0.1	1	660 s
71	PN and wind	5	7N	0.258 - 1.111	0.1	1	660 s
72	PN and wind	5	7N	0.258 - 1.111	0.1	1	240 s
73	Decay in wind surge x 3	6	7N	-	-	-	240 s
74	Decay in wind heave x 3	6	7N	-	-	-	240 s
75	Decay in wind pitch x 3	6	7N	-	-	-	240 s
76	PN and wind	6	7N	0.258 - 1.111	0.1	1	660 s
77	PN and wind	6	7N	0.258 - 1.111	0.1	1	660 s
78	PN and wind	6	7N	0.258 - 1.111	0.1	1	660 s
79	PN and wind	6	7N	0.258 - 1.111	0.1	1	660 s
80	PN and wind	6	7N	0.258 - 1.111	0.1	1	660 s
81	Static load	7	3N	-	-	-	240 s
82	Static load	7	5N	-	-	-	240 s
83	Static load	7	7N	-	-	-	240 s
84	Static load	7	8N	-	-	-	240 s
85	Decay surge x 3	7	-	-	-	-	240 s
86	Decay heave x 3	7	-	-	-	-	240 s
87	Decay pitch x 3	7	-	-	-	-	240 s
88	Decay in wind surge x 3	7	-	-	-	-	240 s
89	Decay in wind heave x 3	7	-	-	-	-	240 s
90	Decay in wind pitch x 3	7	-	-	-	-	240 s
91	PN and wind	7	7N	0.258 - 1.111	0.1	1	660 s
92	PN and wind	7	7N	0.258 - 1.111	0.1	1	660 s
93	PN and wind	7	7N	0.258 - 1.111	0.1	1	660 s
94	PN and wind	7	7N	0.258 - 1.111	0.1	1	660 s
95	PN and wind	7	7N	0.258 - 1.111	0.1	1	660 s
96	Static load	8	3N	-	-	-	240 s
97	Static load	8	5N	-	-	-	240 s
98	Static load	8	7N	-	-	-	240 s
99	Static load	8	8N	-	-	-	240 s
100	Decay surge x 3	8	-	-	-	-	240 s
101	Decay heave x 3	8	-	-	-	-	240 s
102	Decay pitch x 3	8	-	-	-	-	240 s
103	Decay in wind surge x 3	8	-	-	-	-	240 s
104	Decay in wind heave x 3	8	-	-	-	-	240 s
105	Decay in wind pitch x 3	8	-	-	-	-	240 s
106	PN and wind	8	7N	0.258 - 1.111	0.1	1	660 s
107	PN and wind	8	7N	0.258 - 1.111	0.1	1	660 s
108	PN and wind	8	7N	0.258 - 1.111	0.1	1	660 s
109	PN and wind	8	7N	0.258 - 1.111	0.1	1	660 s
110	PN and wind	8	7N	0.258 - 1.111	0.1	1	660 s

7.2 Test List Model B

Test ID	Wave Type	Variation	Wind Speed(m/s)	Frequency(Hz)	Wave Height(m)	Seed	Duration
1	Decay Surge	1	0	-	-	-	-
2	Decay Heave	1	0	-	-	-	-
3	Decay Pitch	1	0	-	-	-	-
4	Pink Noise	1	8m/s	0.258-1.111	0.1	1	660s
5	Pink Noise	1	8m/s	0.258-1.111	0.1	1	660s
6	Pink Noise	1	8m/s	0.258-1.111	0.1	1	660s
7	Pink Noise	1	8m/s	0.258-1.111	0.1	1	660s
8	Pink Noise	1	8m/s	0.258-1.111	0.1	1	660s
9	Decay Surge	2	0	-	-	-	-
10	Decay Heave	2	0	-	-	-	-
11	Decay Pitch	2	0	-	-	-	-
12	Pink Noise	2	8m/s	0.258-1.111	0.1	1	660s
13	Pink Noise	2	8m/s	0.258-1.111	0.1	1	660s
14	Pink Noise	2	8m/s	0.258-1.111	0.1	1	660s
15	Pink Noise	2	8m/s	0.258-1.111	0.1	1	660s
16	Pink Noise	2	8m/s	0.258-1.111	0.1	1	660s
17	Decay Surge	3	0	-	-	-	-
18	Decay Heave	3	0	-	-	-	-
19	Decay Pitch	3	0	-	-	-	-
20	Pink Noise	3	8m/s	0.258-1.111	0.1	1	660s
21	Pink Noise	3	8m/s	0.258-1.111	0.1	1	660s
22	Pink Noise	3	8m/s	0.258-1.111	0.1	1	660s
23	Pink Noise	3	8m/s	0.258-1.111	0.1	1	660s
24	Pink Noise	3	8m/s	0.258-1.111	0.1	1	660s
25	Pink Noise	4	10.64N	0.258-1.111	0.1	1	660s
26	Pink Noise	4	10.64N	0.258-1.111	0.1	1	660s
27	Pink Noise	4	10.64N	0.258-1.111	0.1	1	660s
28	Pink Noise	4	10.64N	0.258-1.111	0.1	1	660s
29	Pink Noise	4	10.64N	0.258-1.111	0.1	1	660s
30	Decay surge	4	0	-	-	-	-
31	Decay Heave	4	0	-	-	-	-
32	Decay pitch	4	0	-	-	-	-

7.3 Summary of Results.

Variation	Wind System	T_r Surge (s)	T_r Heave (s)	T_r Pitch (s)	$T_{r,\,mag}$ Surge (m^2/Hz)	$T_{r,\,mag}$ Heave (m^2/Hz)	$T_{r,\,mag}$ Pitch (deg^2/Hz)	M_{WF} Surge (-)	M_{WF} Heave (-)	M_{WF} Pitch (deg/m)
1	Thruster Ifremer	163.29	20.85	26.58	3.93	0.45	1.20	0.57	0.61	0.76
2	Thruster Ifremer	163.08	20.99	23.72	4.02	0.45	0.57	0.57	0.61	0.58
3	Thruster Ifremer	162.43	21.01	22.29	4.12	0.45	0.64	0.57	0.61	0.62
4	Pulley	162.29	20.83	26.41	2.55	0.47	0.14	0.56	0.62	0.32
5	Pulley	163.65	20.91	25.42	2.18	0.49	0.09	0.56	0.63	0.30
6	Pulley	163.38	20.93	23.40	2.38	0.49	0.09	0.56	0.63	0.32
7	Thruster Ifremer	162.35	20.91	26.56	3.57	0.46	1.11	0.57	0.61	0.73
8	Thruster Ifremer	157.59	20.88	26.55	2.65	0.46	1.16	0.57	0.61	0.75
9	SiL	22.51	3.07	3.62	0.0004	0.0004	0.12	0.76	0.88	20.96
10	SiL	20.86	3.07	3.57	0.0003	0.0004	0.32	0.83	0.87	28.01
11	SiL	20.84	3.08	3.62	0.0003	0.0003	0.13	0.76	0.86	20.80
12	Thruster MaREI	21.00	3.03	3.98	0.0003	0.0004	0.18	0.76	0.89	20.02